

REPORT DOCUMENTATION PAGE			Form Approved OMB No. 0704-0188	
Public reporting burden for this collection of information is estimated to average 1 hour per response, including the time for reviewing instructions, searching existing data sources, gathering and maintaining the data needed, and completing and reviewing the collection of information. Send comments regarding this burden estimate or any other aspect of this collection of information, including suggestions for reducing this burden, to Washington Headquarters Services, Directorate for Information Operations and Reports, 1215 Jefferson Davis Highway, Suite 1204, Arlington, VA 22202-4302, and to the Office of Management and Budget, Paperwork Reduction Project (0704-0188), Washington, DC 20503.				
1. AGENCY USE ONLY (Leave blank)	2. REPORT DATE 11.Oct.00	3. REPORT TYPE AND DATES COVERED THESIS		
4. TITLE AND SUBTITLE HYPERSPECTRAL IMAGING FOR BOTTOM TYPE CLASSIFICATION AND WATER DEPTH DETERMINATION			5. FUNDING NUMBERS	
6. AUTHOR(S) 1ST LT WILSON NIKOLE L				
7. PERFORMING ORGANIZATION NAME(S) AND ADDRESS(ES) ROCHESTER INSTITUTE OF TECHNOLOGY			8. PERFORMING ORGANIZATION REPORT NUMBER CY00384	
9. SPONSORING/MONITORING AGENCY NAME(S) AND ADDRESS(ES) THE DEPARTMENT OF THE AIR FORCE AFIT/CIA, BLDG 125 2950 P STREET WPAFB OH 45433			10. SPONSORING/MONITORING AGENCY REPORT NUMBER	
11. SUPPLEMENTARY NOTES				
12a. DISTRIBUTION AVAILABILITY STATEMENT Unlimited distribution In Accordance With AFI 35-205/AFIT Sup 1			12b. DISTRIBUTION CODE	
13. ABSTRACT (Maximum 200 words)				
14. SUBJECT TERMS			15. NUMBER OF PAGES 170	
			16. PRICE CODE	
17. SECURITY CLASSIFICATION OF REPORT	18. SECURITY CLASSIFICATION OF THIS PAGE	19. SECURITY CLASSIFICATION OF ABSTRACT	20. LIMITATION OF ABSTRACT	

Hyperspectral Imaging for Bottom Type Classification and Water Depth Determination

Nikole L. Wilson

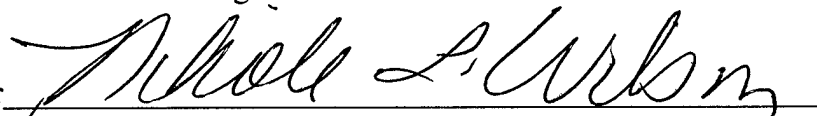
B.S., Engineering Mechanics, U.S. Air Force Academy

(1996)

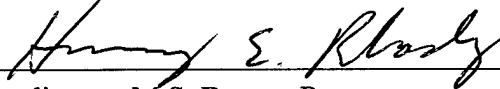
A thesis submitted in partial fulfillment of the
requirements for the degree of Masters of Science
in the Chester F. Carlson Center for Imaging Science
of the College of Science
Rochester Institute of Technology

August 2000

Signature of the Author



Accepted by



Coordinator, M.S. Degree Program

9/12/2000

Date

THESIS RELEASE PERMISSION
ROCHESTER INSTITUTE OF TECHNOLOGY
COLLEGE OF SCIENCE

Hyperspectral Imaging for Bottom Type Classification and
Water Depth Determination

I, Nikole L. Wilson, hereby grant permission to the Wallace Memorial Library of RIT to reproduce my thesis in whole or in part. Any reproduction will not be for commercial use or profit.

Signature of Author



Nikole L. Wilson

Date

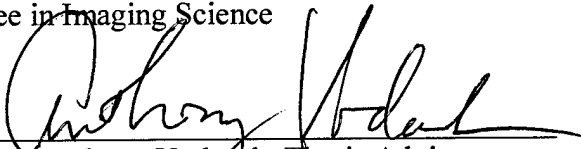
12 SEP 00

CHESTER F. CARLSON
CENTER FOR IMAGING SCIENCE
COLLEGE OF SCIENCE
ROCHESTER INSTITUTE OF TECHNOLOGY
ROCHESTER, NEW YORK

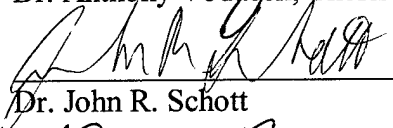
CERTIFICATE OF APPROVAL

M.S. DEGREE THESIS

The M.S. Degree of Nikole L. Wilson
has been examined and approved by the thesis committee
as satisfactory for the thesis requirement for the
Master of Science degree in Imaging Science



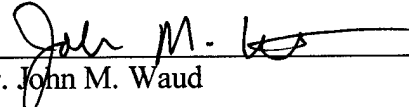
Dr. Anthony Vodacek, Thesis Advisor



Dr. John R. Schott



Mr. Rolando V. Raqueno



Dr. John M. Waud

12 SEP 00

Date

Abstract

Many recreational, military, and commercial activities take place in shallow coastal waters; therefore, interest is high in characterizing these areas. A variety of methods have been employed to determine water depths and classify the bottom using remote sensing. This research proposes to apply Philpot's principal components algorithm for bathymetric mapping to a MISI hyperspectral image, whereas previously this approach has been used on synthetic data. A description of the principal components algorithm is presented along with an outline of how it was applied to airborne hyperspectral images. The algorithm takes advantage of the ability to implement a deep-water correction, and in this linearized space, perform an eigenvector analysis to determine maximum variance in the data, which is related to depth. Unsupervised classification was performed on the first two principal component scores, resulting in a qualitative depth map and bottom type map.

An extensive water measurement campaign was conducted in Lake Ontario in order to characterize the optical properties of the water at the time the MISI images were taken. These properties were used as inputs to the HydroMod radiative transfer model in order to generate sensor-reaching radiance values for various depths and over different bottom types characteristic of a test site on the central New York shore of Lake Ontario. A principal components regression was performed using the algorithm-processed HydroMod model radiances and image data in an effort to determine the inputs to the image, i.e. depth and bottom type, without having a priori information. The limitations of the algorithm as well as the regression approach are discussed.

Acknowledgments

This thesis represents a tremendous accomplishment in my life, one which I could not have completed alone. There are many people that helped me with the research itself, and there are many that saw me through both the ups and downs, and kept me going with their friendship and support. First, I would like to thank the Air Force for putting its faith in me by giving me this rare, extraordinary opportunity. I would like to thank my thesis committee for their time and effort in helping me complete this research. I would like to express my gratitude to Erich Hernandez-Baquero for his endless patience, encouragement, and ideas throughout the past year. Also, I would like to thank Rolando Raqueño for answering countless questions and helping me extensively with HydroMod runs, as well as agreeing to be part of my committee. I would also like to recognize Nina Raqueño, who went out of her way to help me collect ground truth and register images. I really appreciate the advice and ideas that Kirk Knobelspiesse and John Klatt offered in programming and other aspects of this research. To Jonathan Bishop, I owe a debt of gratitude for proofreading this document and providing suggestions. I am very grateful for the adventurous spirit of Stef VanGorden, who was ready at a moment's notice to climb over rocks and wade in muck to obtain much-needed ASD spectra. I would also like to thank Bryce Nordgren for help with MISI, and Ron Fairbanks for getting me started in HydroMod. There are many others I would like to thank who helped out in many ways - gathering ground truth, processing data, providing advice.

Then, there are those people that kept me sane along the way and never once doubted that I would accomplish this goal – God, my family, Beth, old friends, and all of the wonderful new friends I have made in Rochester and nearby. Thank you for believing in me.

Contents

List of Figures	ix
List of Tables	xii
1 Introduction	1
2 Background-Literature Search	4
2.1 Radiance Reaching the Sensor	4
2.1.1 Atmospheric Attenuation	5
2.1.2 The Air-Water Interface	6
2.1.3 In the Water	7
2.1.3.1 Inherent Optical Properties	8
2.1.3.2 Bulk vs Specific Inherent Optical Properties	13
2.1.3.3 Apparent Optical Properties	16
2.2 Composition of Natural Water	19
2.2.1 Pure Water	19
2.2.2 Dissolved Salts and Gases	20
2.2.3 Dissolved Organic Matter	21
2.2.4 Suspended Matter	23
2.2.5 Algal Pigments	25
2.3 Shallow Water Reflectance	27
2.4 Previous Efforts in Bottom Mapping and Bathymetry	31
2.4.1 Single Band Reflectance Model	32
2.4.2 Ratio Method	33
2.4.3 Other Multispectral Methods	37
2.5 Principal Components Method	44
2.6 Choosing the Method	50
3 Methods	52
3.1 Principal Components Analysis	52
3.2 Regression	55
3.3 Principal Components Regression	57
3.4 Water Sampling	59
3.4.1 Filtering	60
3.4.2 Particle Absorption	61

3.4.3 Chlorophyll-a	62
3.4.4 CDOM	62
3.4.5 TSS	63
3.5 Bottom Target Reflectance	63
4 Approach	64
4.1 The Image	64
4.2 Principal Components Algorithm (Philpot 1989)	66
4.2.1 Pre-Processing	67
4.2.2 Deep-Water Correction	68
4.2.3 The Algorithm – Depth	68
4.2.4 The Algorithm – Bottom Type	69
4.3 Inputs to HydroMod	70
4.4 The Forward Model	71
4.5 Applying Principal Components Regression to this Research ...	73
4.5.1 PCR Applied – HydroMod	75
4.5.2 PCR Applied – The Image	76
5 Results	77
5.1 Data Collection	77
5.1.1 Water Sampling	77
5.1.2 Bottom Sampling	79
5.2 MISI Images	84
5.3 Image Selection	91
5.4 Qualitative Results	94
5.4.1 Using the Entire Width for Deep Water	95
5.4.2 Using Darker Deep Water	99
5.4.3 Consistent Deep Water	103
5.4.4 More Results	107
5.4.5 Ontario Beach Results	108
5.5 Building the Forward Model	112
5.6 PCR	116
6 Conclusion	120
Works Cited	131
Appendix A	136
Appendix B	142

Appendix C

154

Appendix D

166

List of Figures

2.1	Components of Sensor-Reaching Radiance	4
2.2	Geometry Used to Define Inherent Optical Properties	9
2.3	Pure Water Absorption Coefficient and Absorption Cross-Section Spectra for chlorophyll, total suspended minerals, and dissolved organic carbon indigenous to Lake Ontario	15
2.4	Pure Water Scattering Coefficient and Scattering Cross-Section Spectra for chlorophyll and total suspended minerals indigenous to Lake Ontario	16
2.5	Optical Properties of Pure Water	20
2.6	CDOM Normalized Spectral Absorption Coefficient used in HydroMod	23
2.7	Suspended Matter Absorption and Scattering Cross-Sections In HydroMod	24
2.8	Chlorophyll a Absorption and Scattering Cross-Sections in HydroMod	26
2.9	Ratio Imagery, Site 5, North Hamlin Beach	36
2.10	Scatter Plot of X-Values for aircraft bands C5 and C7	38
2.11	Linearized Radiance Data for the Two-Band Case	47
2.12	Comparison of Noise in Predicted Depth Using Simple Ratio Vs. Optimal Coefficients	48
2.13	Linearized Radiance Data – Constant Water, But Varying Depth And Bottom Type	49
3.1	PCA	58
4.1	Components of the Forward Model	71
5.1	HydroMod Sand vs. Ontario Sand – Reflectance Spectra	80
5.2	Green Algae Bottom Type in HydroMod	80
5.3	Gray Rock Wet (Groc1_wet)	81
5.4	Groc1_wet input to HydroMod	81
5.5	Gray Rock 2 (Groc2)	82
5.6	Groc2_wet Input to HydroMod	82
5.7	Red Rock (redrock_wet)	82
5.8	Redrock_wet Input to HydroMod	82
5.9	Algae on Red Rock (Rro_alg2)	82
5.10	Rro_alg2 Input to HydroMod	82
5.11	Light Gray Rock Wet (Ltgro1_we)	83
5.12	Ltgro1_wet Input to HydroMod	83
5.13	Yellow Rock Wet (yrocl_we)	83
5.14	Yrocl_wet Input to HydroMod	83
5.15	Bottom Dredger	84

5.16 Band 12 Noise Problems in C9 (Ginna)	85
5.17 Band 20 Noise Problems in C9 (Ginna)	85
5.18 R.G.B.Image near Ginna (Ginna_Four (Bands 24,15,5))	86
5.19 $Y_{ }$ on Ginna_Four	87
5.20 $Y_{ }$ on Ginna_Four Classified	87
5.21 Y_{\perp} on Ginna_Four	87
5.22 Y_{\perp} on Ginna_Four Classified	87
5.23 Image Band 48 from a 400 by 400 Portion of C9	88
5.24 Ginna_Four Image Band 45	88
5.25 $Y_{ }$ Ginna_Seven	89
5.26 $Y_{ }$ Ginna_Seven Classified	89
5.27 Y_{\perp} Ginna_Seven	89
5.28 Y_{\perp} Ginna_Seven Classified	89
5.29 C9 – R,G,B Image of Ginna	91
5.30 Smaller Portion of Image C9 Showing Coastal Bottom Type Variation	92
5.31 C2 – Along Ontario Beach and a Spatially Resized Portion of C2, Ont_One	94
5.32 Image Ginna and the Deepwater Taken Over the Entire Width of the Image	95
5.33 Y for Ginna Image Processed using the Entire Width of C9 for Deep Water	96
5.34 Scatter Plot of X_{640} vs. X_{545} Using the Entire Width of C9	96
5.35 $Y_{ }$ - Deep Water of Entire Image (~Depth)	98
5.36 Y_{\perp} - Deep Water of Entire Image (~Bottom Type)	98
5.37 Ginna Image and Deep Water from the Right Side of C9	99
5.38 $Y_{ }$ for Ginna Processed With Deep Water From Right of C9	100
5.39 Scatter Plot of X_{640} vs. X_{545} Using the Right Side of C9 for Deep Water	100
5.40 Eigenvalues from PCA on Ginna Image Processed Using Deep Water from the Right Side of C9	101
5.41 $Y_{ }$ Using Deep Water from Right (~Depth)	102
5.42 Y_{\perp} Using Deep Water from Right (~Bottom Type)	102
5.43 Y_{\perp} (~Bottom Type) is Picking Up on Variations in Ginna Image	103
5.44 Image and Deep Water from the Right Side of Ginna	104
5.45 Ginna_Right With Colors Corresponding to 5.46	104
5.46 Scatter Plot of X_{640} vs. X_{545} for Ginna_Right	104
5.47 $Y_{ }$ (~depth) – K-means Classification of Ginna_Right Using 3 Classes and 4 Classes, Respectively	105
5.48 Y_{\perp} (~Bottom Type) Using 3 and 4 Classes, Respectively and Comparison to Actual Image	106

5.49	Ginna_Left With its Corresponding Depth and Bottom Type Maps	107
5.50	Ginna_Middle With its Corresponding Depth and Bottom Type Maps	107
5.51	Image Near Ontario Beach, C2, and the Image Area Selected for Processing, Ont_One	109
5.52	$Y_{ }$ for Ont_One	110
5.53	$Y_{ }$ Classified for Ont_One	110
5.54	Y_{\perp} for Ont_One	110
5.55	Y_{\perp} Classified for Ont_One	110
5.56	Ground Truth Results for Ont_One	111
5.57	Transmission and Upwelled Radiance for September 3, 1999	112
5.58	Plot of Sensor-Reaching Radiance for a Zero-Reflectance Bottom	113
5.59	Sensor-Reaching Radiances at Depth of 0.5 m	114
5.60	Sensor-Reaching Radiances at Depth of 1 m	114
5.61	Sensor-Reaching Radiances at Depth of 30 m	115
5.62	Eigenvalues from the PCA on Model Data	116
5.63	Quantitative Depth Results for Ginna_Left	117
5.64	Quantitative Depth Results for Ginna_Right	118
5.65	Quantitative Depth Results for Ginna_Middle	118
6.1	C9 Image Near Ginna Power Plant	122
6.2	$Y_{ }$ - Deep Water of Entire Image (~Depth)	122
6.3	Y_{\perp} - Deep Water of Entire Image (~Bottom Type)	122
6.4	$Y_{ }$ Using Deep Water From Right (~Depth)	123
6.5	Y_{\perp} Using Deep Water From Right (~Bottom Type)	123
6.6	$Y_{ }$ (~Depth) for Ginna_Right	124
6.7	Y_{\perp} (~Bottom Type) for Ginna_Right	124
6.8	Smaller Portion of Image C9 (Ginna)	126
6.9	C2 - Image Near Ontario Beach	129

List of Tables

4.1	MISI Bandcenters for Visible and NIR Bands	65
4.2	Inputs to HydroMod	72
5.1	Water Sampling Dates and Locations – 1999 and 2000	78
5.2	Sampling Results for Ginna, September 3, 1999	78
5.3	Ginna (C9) MISI Bands Retained for Algorithm	90
D.1	September 3, 1999 Chlorophyll-a concentrations – determined Spectrophotometrically	167
D.2	September 3, 1999 Chlorophyll-a values – determined Fluorimetrically	168
D.3	September 3, 1999 TSS Values	168
D.4	September 3, 1999 CDOM Values	169
D.5	Comparison of Chlorophyll-a Processing Results	169

Chapter 1

Introduction

An advantage of remote sensing is that it provides a synoptic view and can help reduce the amount of time and money spent on sampling. A drawback is that the intervening atmosphere presents a challenge to the interpretation of remotely sensed images. Remote sensing over water is a particularly difficult task because the water is an additional attenuation source. Various components in the water act as absorbing and scattering centers for the radiation that penetrates into the water column.

Much of the research that has been conducted on remote sensing over water has been concerned with the oceans. Remote sensing over shallow water adds one more complexity to the problem: reflection from the bottom. The radiance reaching the sensor over optically shallow water includes not only radiation reflected from the atmosphere, but also radiation reflected from the surface of the water, from the water column itself, and from the bottom.

Understanding the properties of shallow water is important because many recreational and economic activities take place near shore. Remote sensing is a tool that can be used to understand these shallow water properties, such as bottom type variation and depth. For example, Monroe County is interested in the location and distribution of green algae on the bottom of Lake Ontario, particularly the Ontario Beach area near

Rochester, NY. The Monroe County Environmental Health Laboratory's "1998 Ontario Beach Monitoring Report" states that decaying algal plant matter, specifically cladophora and spirogyra, was responsible for 13% of the beach closures. These algae wash up on shore where they act as a substrate for bacterial growth and provide to the bacteria a shield from the harmful effects of ultraviolet light. In coastal waters there is a relationship between high levels of bacteria known as indicator bacteria, which are typically found in the presence of harmful bacteria, and the occurrences of swimming-related illnesses. The Health Lab is interested in knowing where the algae are growing in the water as part of their effort to manage the problem. A bottom type map, produced from remotely sensed data, would be useful in addressing such ongoing environmental problems. The algae grow on hard surfaces, such as the rock comprising parts of the lake floor near the Ontario Beach area. The rock and algae reflect light reaching the bottom of the lake differently than the surrounding sand, which is the reason bottom type mapping is capable of distinguishing between a rock bottom and a sand bottom.

In addition to providing bottom type information for applications such as the one discussed above, remote sensing of shallow waters can also provide depth information. Photogrammetric analysis of the bottom of Tampa Bay provided information about circulation patterns in the bay which was extremely beneficial in the evaluation of plans for dredging the bay (Rosenshein et al. 1977). However, interpretation of aerial photographs using photogrammetry is limited because water depth variations are not easily distinguishable from bottom type differences. Remote sensing over shallow waters

calls for a technique which will distinguish the variation in bottom type reflectance from the variation in the reflectance spectra due to absorption and scattering within the water column. This is the problem addressed in the current research.

This research contributes in three ways to the study of using remotely sensed imagery to gain information about depth and bottom type in shallow, coastal water. First, the algorithm used here was implemented on a hyperspectral image taken by the Modular Imaging Spectrometer Instrument (MISI), rather than a synthetic data set. This involved identifying the challenges of using real data, working around them, and analyzing the algorithm's limitations. The algorithm was implemented to determine qualitative depth and bottom type information from images taken at the Ginna power plant and near Ontario Beach. Second, the research shows the usefulness of the bottom classification map to the County Health Lab in their management efforts to prevent beach closures due to algae washing up on the shore. The third contribution is taking Philpot's algorithm in a new direction by using principal components regression (PCR) to quantitatively determine the unknowns (depth, bottom type, water type) that combine to form an image over shallow water. This study illustrates how the radiative transfer model HydroMod can be used as a model to simulate the conditions under which the Lake Ontario MISI images were taken, calculating sensor-reaching radiances, which were then used to calibrate the PCR.

Chapter 2

Background-Literature Review

2.1 Radiance Reaching the Sensor

Remote sensing over shallow water is difficult because of the various components that contribute to the radiance that reaches the sensor. There are essentially two components that make up the sensor reaching radiance. The first is the upwelled radiance scattered from the atmosphere (blue arrow in Fig. 2.1). The second is the radiance reflected from the scene, composed of three different parts: (1) The radiance reflected from the surface of the water (green arrow in Fig 2.1), (2) water column reflected radiance (violet line in Fig 2.1), and (3) bottom-reflected (orange arrow in Fig 2.1).

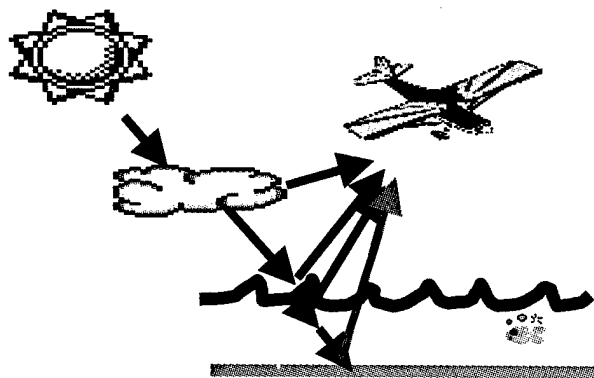


Figure 2.1 Components of Sensor-Reaching Radiance

The radiative transfer model, HydroMod, can be used to understand the components shown in Fig. 2.1. HydroMod is a tool for calculating radiance distributions using realistic environmental conditions. It uses the Air Force Laboratory's MODTRAN (Berk 1989), one of the most accurate radiative transfer computer models available, to calculate the atmospheric conditions through which photons travel on their path toward the water surface and again on their return to the sensor (Fairbanks 1999).

The HydroMod program consists of four modules (Fairbanks 1999). The first module calculates the input radiance distribution using MODTRAN to calculate atmospheric conditions. The second module involves the transition through the water surface both into and out of the water. The third module handles the propagation and reflection underwater. This is accomplished using Dr. Mobley's Hydrolight code (Mobley 1995,1996) to solve the radiative transfer under the water. Finally, the light is propagated back through the atmosphere to the sensor using MODTRAN.

2.1.1 Atmospheric Attenuation

The radiance reaching the sensor over water first passes through the atmosphere where some of it is scattered and some of it is absorbed. Direct solar radiation is scattered and absorbed, but still proceeds from the general direction of the sun, as opposed to diffuse sky radiation, which results from scattering by aerosols and air molecules. Bukata, et al. (1995) define the atmospheric attenuation coefficient, $c_s(\lambda)$, as the fraction of radiant energy removed per unit distance due to absorption and scattering as a beam of solar radiation travels through the atmosphere. $c_s(\lambda)$ is expressed as a

summation of the attenuation coefficients due to the various components that comprise the atmosphere. Attenuation by the atmosphere is a result of molecular (Rayleigh) scattering, aerosol scattering, and absorption by gases.

The atmosphere interferes with the signal from the water, requiring that its effect be removed in order to analyze the scene. The algorithm implemented here on MISI images subtracts off the effect of the atmosphere, based on the assumption that the atmosphere is invariant over the scene, in a procedure termed the “deep-water correction”. The radiative transfer model, HydroMod, was used to model the conditions under which the MISI images were taken, resulting in sensor-reaching radiance values.

2.1.2 The Air-Water Interface

Photons not scattered by the atmosphere interact with the water surface. At the surface, they are either reflected, refracted, or transmitted.

Refraction of the light is governed by Snell’s Law,

$$n_a \sin \theta_a = n_w \sin \theta_w \quad (2.1)$$

in which a and w refer to air and water, respectively, and n is the index of refraction. The angle, θ , is the angle between the direction of the photon flux and the in-water normal.

The reflected photon flux is given by Fresnel’s reflectance formula. For perpendicular polarized light, the reflectance is

$$\rho_{\parallel} = \frac{\tan^2(\theta_i - \theta_r)}{\tan^2(\theta_i + \theta_r)} \quad (2.2)$$

For parallel polarized light, the reflectance is

$$\rho_{\perp} = \frac{\sin^2(\theta_i - \theta_r)}{\sin^2(\theta_i + \theta_r)} \quad (2.3)$$

And for randomly polarized light,

$$\rho = 0.5 \frac{\sin^2(\theta_i - \theta_r)}{\sin^2(\theta_i + \theta_r)} + 0.5 \frac{\tan^2(\theta_i - \theta_r)}{\tan^2(\theta_i + \theta_r)} \quad (2.4)$$

Further information on the air-water interface, including the impact of waves, is given in Bukata (1995) and Mobley (1994).

2.1.3 In The Water

As discussed, the atmospheric and water surface interactions are accounted for in HydroMod (Fairbanks 1999). HydroMod also accounts for the in-water interactions, but the water properties are required. The ground truth gathered for this project allows the optical properties of the water to be determined and used as inputs to HydroMod. The following discussion focuses on the in-water interactions.

Case 1 waters are those waters that have a high concentration of phytoplankton compared to colored dissolved organic matter and nonbiogenic particles or where the phytoplankton covary with the other components. Most coastal water is considered Case 2 water because inorganic or colored dissolved organic matter from land drainage are important and may not covary with absorption by pigments, such as chlorophyll (Mobley 1994). This research is concerned with these coastal waters. The concentrations of these components determine the optical properties of the water.

There are two different categories of optical properties – apparent and inherent. According to Mobley (1994), apparent optical properties are those properties of the water that depend on both the medium and the structure of the light field, and that are regular enough to provide a good description of the water. Inherent optical properties are those properties that depend solely on the medium.

2.1.3.1 Inherent Optical Properties

The inherent optical properties of water include the absorption coefficient $a(\lambda)$, the total attenuation coefficient $c(\lambda)$, the scattering coefficient $b(\lambda)$, the forwardscattering probability $F(\lambda)$, the backscattering probability $B(\lambda)$, the scattering albedo $\omega_o(\lambda)$, and the volume scattering function $\beta(\theta)$ (Bukata 1995). Definitions of these properties are taken from Mobley (1994). Figure 2.2 shows the geometry which will be important in defining optical properties.

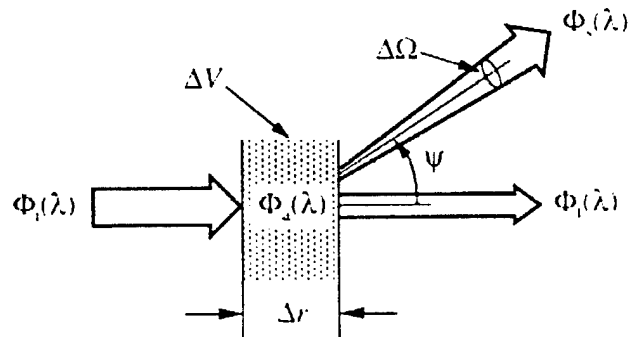


Figure 2.2 Geometry used to define Inherent Optical Properties (Mobley's Fig 3.1)

Mobley defines a small volume ΔV of water, of thickness Δr , which is illuminated by a narrow collimated beam of monochromatic light $\Phi_i(\lambda)$, W nm^{-1} . Part of this incident power is absorbed by the water volume and is designated $\Phi_a(\lambda)$. Also, some part of this power is scattered out of the incident beam at angle ψ , and is termed $\Phi_s(\psi, \lambda)$. The power in the beam that has not been either scattered or absorbed is transmitted $\Phi_t(\lambda)$ through the volume of water. Assuming that no inelastic scattering occurs and the photons retain their original wavelengths, under the conservation of energy,

$$\Phi_i(\lambda) = \Phi_a(\lambda) + \Phi_s(\lambda) + \Phi_t(\lambda) \quad (2.5)$$

The spectral absorbance, $A(\lambda)$, is that fraction of incident power that is absorbed within the volume defined above. Likewise, the spectral scatterance, $B(\lambda)$, is that fraction which is scattered. Finally, the spectral transmittance, $T(\lambda)$, is the remainder of the incident

power, which is transmitted through the volume. These three quantities are mathematically defined below:

$$A(\lambda) \equiv \frac{\Phi_a(\lambda)}{\Phi_i(\lambda)} \quad B(\lambda) \equiv \frac{\Phi_s(\lambda)}{\Phi_i(\lambda)} \quad T(\lambda) \equiv \frac{\Phi_t(\lambda)}{\Phi_i(\lambda)} \quad (2.6) \quad (2.7) \quad (2.8)$$

The inherent optical properties are the spectral absorption coefficient and the spectral scattering coefficient, which are the absorptance and scatterance per unit distance. The spectral absorption coefficient is

$$a(\lambda) \equiv \lim_{\Delta r \rightarrow 0} \frac{A(\lambda)}{\Delta r} \quad (m^{-1}) \quad (2.9)$$

The spectral scattering coefficient is defined as

$$b(\lambda) \equiv \lim_{\Delta r \rightarrow 0} \frac{B(\lambda)}{\Delta r} \quad (m^{-1}) \quad (2.10)$$

The total beam attenuation coefficient is the summation of the absorption and scattering coefficients,

$$c(\lambda) \equiv a(\lambda) + b(\lambda) \quad (m^{-1}) \quad (2.11)$$

The above terms describe the attenuation of light propagating through water. The remaining inherent optical properties describe the directionality of the scattering interactions. Not only does the amount of power scattered need to be considered, but also

the angular distribution of this scatter: the angular scatterance per unit distance and unit solid angle, known as the spectral volume scattering function is given by

$$\beta(\psi; \lambda) \equiv \lim_{\Delta r \rightarrow 0} \lim_{\Delta \Omega \rightarrow 0} \frac{B(\psi; \lambda)}{\Delta r \Delta \Omega} = \lim_{\Delta r \rightarrow 0} \lim_{\Delta \Omega \rightarrow 0} \frac{\Phi_s(\psi; \lambda)}{\Phi_i(\lambda) \Delta r \Delta \Omega} \quad (m^{-1} sr^{-1}) \quad (2.12)$$

where $\Delta \Omega$ is a given solid angle. The spectral power scattered into this given solid angle is equal to the spectral radiant intensity scattered into the direction indicated by ψ times the given solid angle. Therefore,

$$\beta(\psi; \lambda) \equiv \lim_{\Delta V \rightarrow 0} \frac{I_s(\psi; \lambda)}{E_i(\lambda) \Delta V} \quad (2.13)$$

which gives rise to the definition that the spectral volume scattering function is the scattered intensity per unit incident irradiance per unit volume of water. Irradiance (E) is defined as the rate at which the radiant flux, or power, is delivered to a surface. The radiant intensity (I) describes the directional information about the flux (Schott 1997).

The relationship between the spectral volume scattering function and the scattering coefficient is defined in the following formula where Ξ represents the unit sphere.

$$b(\lambda) = \int_{\Xi} \beta(\psi; \lambda) d\Omega = 2\pi \int_0^\pi \beta(\psi; \lambda) \sin \psi d\psi \quad (2.14)$$

The integration defined above is typically divided into forward scattering, over the angles $0 \leq \Psi \leq \pi/2$ and backward scattering over the angles $\pi/2 \leq \psi \leq \pi$. The forward scattering coefficient, b_F , and the backscattering coefficient, b_B , are defined as follows

$$b_F = 2\pi \int_0^{\pi/2} \beta(\psi) \sin \psi d\psi$$

$$b_B = 2\pi \int_{\pi/2}^{\pi} \beta(\psi) \sin \psi d\psi$$

(2.15) (2.16)

Bukata (1995) explains that the photons scattered into either the forward or backward direction are spoken of in terms of probabilities, or the fractions of the total scattered flux directed into each hemisphere. The forward scattering probability, F , is the ratio of flux scattered into the hemisphere ahead of the incident flux to the total scattered flux. Similarly, the backscattering probability, B , is the ratio of the flux scattered into the hemisphere behind the incident flux to the total scattered flux and these probabilities are defined in the following equations.

$$F = \frac{b_F}{b} \quad B = \frac{b_B}{b}$$

(2.17) (2.18)

The last IOP introduced here is the spectral single-scattering albedo, ω_0 , which is the probability that a photon will be scattered rather than absorbed, and is defined as

$$\omega_0(\lambda) \equiv \frac{b(\lambda)}{c(\lambda)} \quad (2.19)$$

2.1.3.2 Bulk vs Specific Inherent Optical Properties

Bulk inherent optical properties (IOPs) are those that are described in the previous section and are based on considering the water column as a whole rather than as various components that absorb and scatter. Specific inherent optical properties are those that are attributed to the individual components in the water that act as absorbing and scattering centers. These specific IOPs are the ones that must be determined when trying to use remote sensing to determine concentrations of the various components in the water. The bulk IOPs, previously defined, are simply summations of the individual specific IOPs. From Bukata et al. (1995),

$$a(\lambda) = \sum_{i=1}^n x_i a_i(\lambda) \quad (2.20)$$

$$b(\lambda) = \sum_{i=1}^n x_i b_i(\lambda) \quad (2.21)$$

$$B(\lambda)b(\lambda) = \sum_{i=1}^n x_i B_i(\lambda) b_i(\lambda) \quad (2.22)$$

(2.20) (2.21) (2.22)

where

$B(\lambda)b(\lambda)$ = backscattering coefficient at wavelength λ (product of backscattering probability and the scattering coefficient)

x_i = concentration of the i th component of the water column

$a_i(\lambda)$ = absorption coefficient at wavelength λ for a unit concentration of aquatic component i

$b_i(\lambda)$ = scattering coefficient at wavelength λ for a unit concentration of aquatic component i

The specific absorption coefficient and the specific scattering coefficient are frequently referred to as the absorption cross-section and scattering cross-section, respectively. Bukata et al. (1995) states that the governing principle behind the remote sensing of the organic and inorganic components of water is that the optical cross sections provide the link between the concentrations of the individual components in the water and the bulk inherent optical properties. If the concentrations of the individual components in the water can be determined, and the optical cross sections of the water are known, the total attenuation of the light due to absorption and scattering in the water column can be determined.

Bukata et al. (1995) limit their optical model to four components, which are followed in this research. A comprehensive model, which considers the optical cross sections of every aquatic component in natural waters, is unattainable. Their rationale is that for the Great Lakes waters, only a small loss in generality occurs due to using this four-component model, as opposed to a model which includes a fifth component, non-living organics, to account for detrital matter. These non-living suspended organics rarely dominate the color of inland and coastal waters. The four-component model includes pure water (W), chlorophyll (Chl), dissolved organic carbon (DOC), and suspended minerals (SM). Therefore, the bulk IOPs may be defined as follows:

$$a(\lambda) = a_w(\lambda) + x_1 a_{Chl}(\lambda) + x_2 a_{SM}(\lambda) + x_3 a_{DOC}(\lambda)$$

$$b(\lambda) = b_w(\lambda) + x_1 b_{Chl}(\lambda) + x_2 b_{SM}(\lambda)$$

$$B(\lambda)b(\lambda) = B_w(\lambda)b_w(\lambda) + x_1 B_{Chl}(\lambda)b_{Chl}(\lambda) + x_2 B_{SM}(\lambda)b_{SM}(\lambda)$$

(2.23) (2.24) (2.25)

The coefficients x_1 , x_2 , and x_3 are the concentrations of chlorophyll, suspended minerals and DOC, respectively. The absorption cross-section and scattering cross section for Lake Ontario (Bukata 1995) are shown in Figures 2.3 and 2.4. Bukata (1995) makes reference to suspended minerals, but this component will be referred to here as suspended matter because this research does not distinguish the mineral from the organic particles.

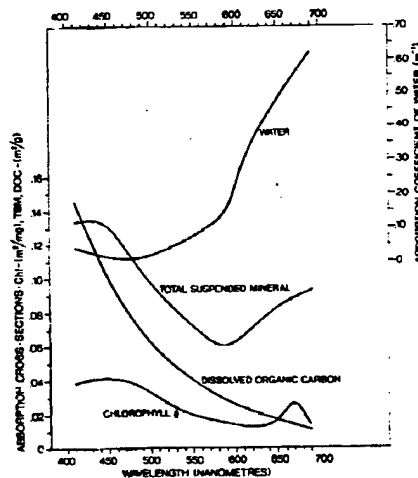


Figure 2.3 Pure water absorption coefficient and absorption cross-section spectra for chlorophyll, total suspended mineral, and dissolved organic carbon indigenous to Lake Ontario (Fig 5.5 of Bukata 1995)

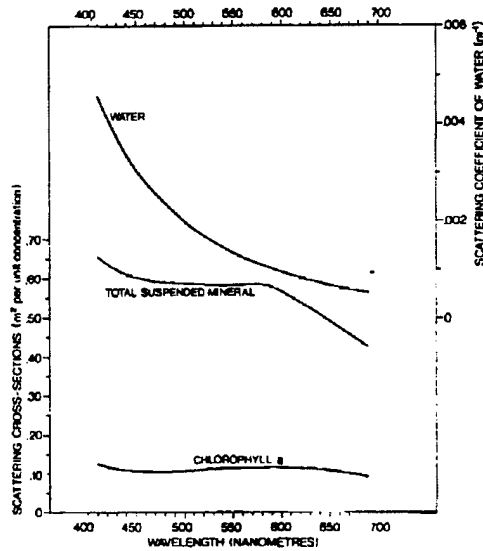


Figure 2.4 Pure water scattering coefficient and scattering cross-section spectra for chlorophyll and total suspended minerals indigenous to Lake Ontario (Fig 5.6 of Bukata 1995)

In order to generate the sensor-reaching radiances, HydroMod requires the component concentrations for chlorophyll, suspended solids, and DOC. These component concentrations are multiplied by the optical cross-sections of the aquatic components included in the model. Updated optical cross-sections for these components in Lake Ontario, determined from processing and analysis of water samples, are included in the HydroMod model to generate radiance data, with the exception of pure water and chlorophyll. These updated cross-sections are presented in Section 2.2.

2.1.3.3 Apparent Optical Properties

As stated earlier, the apparent optical properties (AOP) depend not only on the medium, but also on the structure of the ambient light field, and they are used whenever a

radiometric quantity other than radiance is used. The first AOP that will be discussed here is the irradiance attenuation coefficient, $K(\lambda, z)$. Bukata et al. (1995) define the irradiance attenuation coefficient as the logarithmic depth derivative of the spectral irradiance at a depth of z . The actual definition of $K(\lambda, z)$ results from Beer's Law (Bukata 1995) and is derived below. A beam of light passing through a medium loses some of its initial radiance flux value, Φ_{inc} , due to absorption loss by an attenuating medium of thickness Δr , and only Φ_{trans} remains of the original beam of light, according to the following form of Beer's law.

$$\Phi_{trans} - \Phi_{inc} = -a\Phi_{inc}\Delta r \quad (2.26)$$

or
$$\Delta\Phi = -a\Phi_{inc}\Delta r \quad (2.27)$$

The constant of proportionality, a , is defined as the absorption coefficient. Then, in the limit as both $\Delta\Phi$ and Δr approach zero, the equation becomes

$$\frac{d\Phi}{\Phi} = -adr \quad (2.28)$$

which is Beer's Law. Integrating equation 2.28 from $r = 0$ to a distance r in the absorbing medium, and knowing that the beam coefficient is a function of wavelength yields the following equation:

$$\Phi(r, \lambda) = \Phi(0, \lambda)e^{-a(\lambda)r} \quad (2.29)$$

and consequently for a beam propagating vertically in water,

$$E(\lambda, z) = E(\lambda, 0-) \exp[-K(\lambda, z)z] \quad (2.30)$$

where $E(\lambda, z)$ = the value of irradiance at depth z and $E(\lambda, 0-)$ = the irradiance just below the air-water interface. Finally, Equation 2.31 defines the irradiance attenuation coefficient, resulting from Beer's Law being used to describe the attenuation of spectral irradiance with depth z (Eq. 2.30).

$$K(\lambda, z) = -\frac{1}{E(\lambda, z)} \left[\frac{\partial E(\lambda, z)}{\partial z} \right] (m^{-1}) \quad (2.31)$$

This AOP shows how the irradiance decreases exponentially with depth due to attenuation by the water. The irradiance attenuation coefficient divided into the

downwelling irradiance attenuation coefficient $K_d(\lambda, z)$ and the upwelling irradiance attenuation coefficient $K_u(\lambda, z)$ is

$$K_d(\lambda, z) = -\frac{1}{E_d(\lambda, z)} \left[\frac{\partial E_d(\lambda, z)}{\partial z} \right] m^{-1}$$

$$K_u(\lambda, z) = -\frac{1}{E_u(\lambda, z)} \left[\frac{\partial E_u(\lambda, z)}{\partial z} \right] m^{-1}$$

(2.32) (2.33)

where E_d and E_u refer to the downwelled and upwelled irradiances, respectively. For a review of these radiometric terms, refer to Schott (1997).

2.2 Composition of Natural Water

Natural waters are composed of a myriad of living, non-living, and once-living material. These components determine the optical properties of the water that were discussed in the previous section

2.2.1 Pure Water

Pure water implies that the water is free from the scattering and absorption effects of organic and inorganic matter. The attenuation due to pure water is due only to water molecules. Pure water typically absorbs weakly in the blue and green regions of the electromagnetic spectrum. As Kirk (1983) states, the absorption of pure water increases above 550 nm and is quite significant in the red. Figure 2.5 shows the absorption and scattering spectra of pure water as measured by Smith and Baker (1981), which are the water optical cross-sections used in HydroMod.

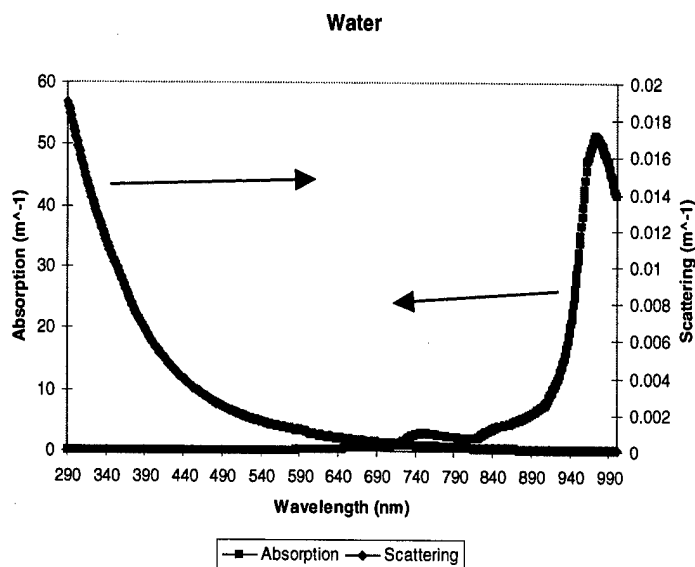


Fig. 2.5 Optical Properties of Pure Water (Smith and Baker 1981)

Above 550 nm, the attenuation of light by pure water is dominated by absorption and the total attenuation coefficient due to pure water can be approximated as the absorption coefficient due to pure water. However, in the blue region, $\lambda = 400\text{-}520$ nm, scattering by pure water plays a greater role in total attenuation (Bukata 1995). The strong absorption in the red and weak absorption, but strong scattering, in the blue-green region of the spectrum causes the blue appearance of water.

2.2.2 Dissolved Salts and Gases

Dissolved salts and gases are not included in the four-component model discussed earlier. Dissolved salts do affect absorption within the water column, with the most significant effect at ultraviolet wavelengths, $\lambda < 300$ nm. Molecular scattering in mid-oceanic waters due to the pure water/dissolved salt combination is relatively insignificant

compared to the total attenuation. The specific directional scattering due to pure water/dissolved salts plays a more significant role in molecular scattering. However, for inland waters, the ability of dissolved salts to create a directional nature to $\beta(\psi)$ is significantly reduced compared to mid-oceanic waters due to their much lower concentrations in fresh water (Bukata 1995). Dissolved gases, of which dissolved oxygen is the most significant, also do not produce significant changes to the bulk optical properties of the water, and therefore, are not included in the model.

2.2.3 Dissolved Organic Matter

Dissolved organic matter (DOM) does not have a significant impact on scattering as evidenced by the fact that it is not included in Eq. 2.24. DOM does, however, impact the absorption in natural waters and is often the dominant component in the optical absorption of coastal water (Vodacek et al. 1997). The optically active component of DOM is referred to as Colored Dissolved Organic Matter (CDOM). DOM is a result of excretion, secretion, or decomposition of plants and animals in the water, or of direct input of terrestrial material. Plant or animal materials are transformed into DOM through hydrolysis, photolysis, and bacterial decomposition of their cellular structure. The decomposition of plants and animals results in water soluble humic substances which are responsible for the yellow color observable in some inland and coastal waters. Although these pigments comprise only about 40% of the DOM, the yellow hue has given rise to the various terms given to DOM, such as colored dissolved organic matter (CDOM), yellow substance, gelbstoff, gilvin, etc. (Bukata 1995).

Lake Ontario displays DOM concentrations on the order of 2 g C/m^3 , which is fairly low compared to average lake water concentrations reported in the literature of 9 or 10 g C/m^3 . (Bukata 1995) An absorption curve can be represented by the following relationship, which is valid over the wavelengths $\lambda = 350\text{-}700 \text{ nm}$,

$$a_g(\lambda) = a_g(\lambda_0) \exp[-S(\lambda-\lambda_0)]$$

(Bricaud, et al 1981) (2.34)

The subscript, *g*, stands for gelbstoff. The variable, *S*, is a slope parameter assumed to be independent of wavelength. The values for the parameter, *S* (nm^{-1}), typically range between 0.010 to 0.020, with a mean value of 0.014. The reference wavelength, λ_0 , is typically arbitrary, but usually in the UV or blue. Spectrophotometric analysis of a water sample, filtered to remove scattering particles, with the absorption of pure water, subtracted, becomes an estimate of $a_g(\lambda)$. The study examined the wavelengths between $\lambda = 350\text{-}700 \text{ nm}$ because that was the range of the spectrophotometer used. Below $\lambda = 350\text{-}700 \text{ nm}$, there were a few discontinuities in some of the samples measured, but the absorption between $\lambda = 350 \text{ nm}$ and $\lambda = 700 \text{ nm}$ reasonably followed the law shown in Eq.2.34. The normalized CDOM spectral absorption coefficient of Lake Ontario water (Fig. 2.6) used for this study in the HydroMod model was determined from samples collected on May 20, 1999. A spectral absorption coefficient normalized to one at 350 nm is used in the work instead of a cross-section, because DOC measurements were not available. Instead, the normalized

coefficient is multiplied by a scalar to arrive at an appropriate spectral absorption coefficient. The scalar used for Lake Ontario waters was 0.2.

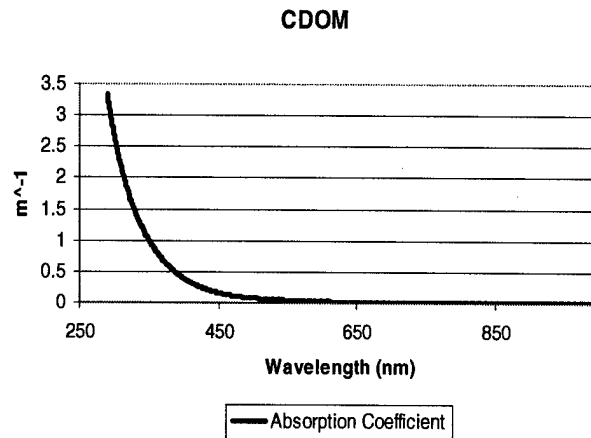


Figure 2.6 CDOM normalized spectral absorption coefficient used in HydroMod

2.2.4 Suspended Matter

The term “suspended matter” includes both organic and inorganic matter. Suspended matter is derived from plankton, detritus from the decomposition of phytoplankton, zooplankton, and macrophytic plants, as well as terrigenous suspended particles formed by erosion and discharge. A large portion of this suspended matter is suspended minerals, which according to Bukata (1981) have concentrations in Lake Ontario of 0.2-8.9 g/m³. The HydroMod absorption and scattering cross-sections for suspended matter are shown in Fig. 2.7. The absorption cross-section was generated from a curve that represents the average of a set of curves measured from water samples collected on May 20, 1999. The scattering cross-section was taken from a backscattering

cross-section curve measured and modified by Dr. Vodacek to match Bukata's (1995) curve.

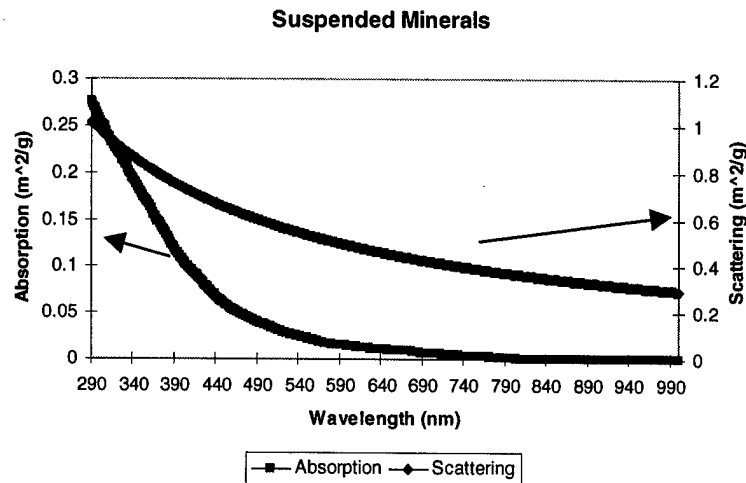


Figure 2.7 Suspended Matter Absorption and Scattering Cross-Sections in HydroMod

In addition, there are various precipitates, a result of chemical activity, that can affect the absorption and scattering within a water body. For example, Landsat first viewed chemical precipitations of calcium carbonate, known as whittings, in the Great Lakes in 1973 (Strong, 1978). As surface waters become saturated with Ca^{++} ions in the summer time, a biological or physical mechanism initiates the whiting.

Zooplankton feed on the algae, detritus, and bacteria, and therefore help to determine the status of the water. For example, a highly productive water body will have a higher concentration of zooplankton, while the populations of zooplankton in natural waters may be patchy because they are moved around by currents, reproductive cycles,

the availability of food, and other factors. The effect of zooplankton on color is largely unknown, but assumed to be minor due to their small concentrations in comparison to phytoplankton and bacterioplankton.

There are also bacterioplankton in the water, which do not contribute to the overall water color, although they probably have some effect on scattering. Planktonic fungi are colorless, chlorophyll-free lower plant forms consisting of cellular filaments containing spores. These planktonic fungi present in the water column are assumed to have negligible optical impact on the optical properties of the water due to their lack of color in addition to their low concentrations (Bukata 1995).

2.2.5 Algal Pigments

Phytoplankton cells contribute to water color, depending on their pigments. All phytoplankton contain chlorophyll and carotenoids, which are responsible for photosynthesis. All green algae contain chlorophyll a, and possibly b and/or c. As Bukata states (1995), the ratio of chl a to chl b is approximately 3:1, and therefore, as Bukata does in his model, the research here focuses on the presence of chl a. Chlorophyll absorption occurs in the blue and red regions of the spectrum (Fig. 2.8), and is more intense in the blue region for chl a.

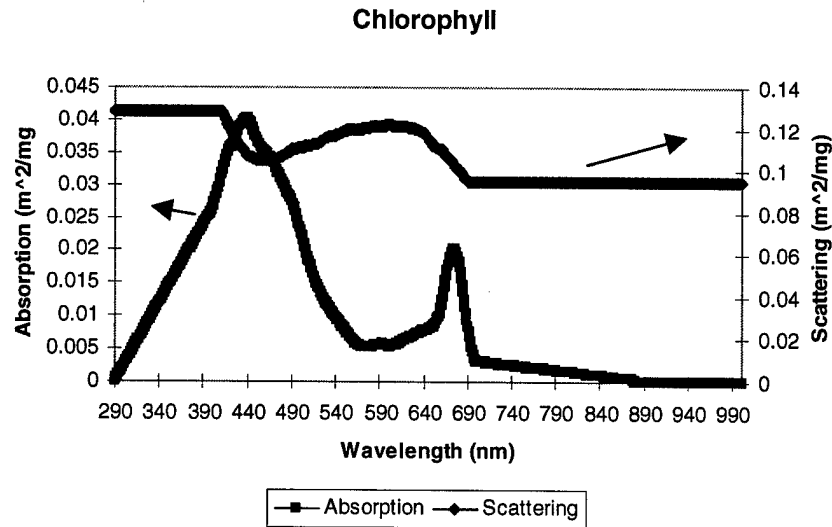


Figure 2.8 Chlorophyll a Absorption and Scattering Cross-Sections in HydroMod (Bukata 1995)

Decomposed chlorophyll, in the form of phaeophytin, must be accounted for because it causes a peak shift toward shorter wavelengths in the blue region and a peak shift toward longer wavelengths in the red region. The intensity of the absorption for this chlorophyll derivative is weak compared to the intensities of the absorption bands of chlorophyll, but an estimate of phaeophytin is essential to determining the portion of non-living phytoplankton in the water.

Understanding these properties helps in derivation of algorithms for determining water depth and bottom type information.

2.3 Shallow Water Reflectance

The irradiance just below the surface includes the flux scattered back by the water column itself (i.e., the photons that never reach the bottom) and the flux scattered back from the bottom:

$$E_u(0) = [E_u(0)]_C + [E_u(0)]_B \quad (2.35)$$

where

$E_u(0)$ = the upwelling irradiance just below the surface

$[E_u(0)]_C$ = upwelling irradiance just below the surface due to the water column

$[E_u(0)]_B$ = upwelling irradiance just below the surface due to the bottom

The derivation of the following expression for shallow water reflectance is included in Maritorena et al. (1994), who use some simplifying assumptions in order to derive analytical formulas for shallow water reflectance. In order to estimate the irradiance due to the water column, they model an infinitely thin layer of thickness dz at depth z , where the downwelling irradiance at this point is $E_d(z)$. The backscattering coefficient for this downwelling light is b_{bd} . Then, the upwelling irradiance created by this infinitely thin layer of water is

$$dE_u(z) = b_{bd}E_d(z)dz \quad (2.36)$$

The irradiance at depth z can then be expressed as

$$E_d(z) = E_d(0) \exp(-K_d z) \quad (2.37)$$

where $E_d(0)$ is the downwelling irradiance at zero depth and K_d is the downwelling irradiance attenuation coefficient. The upwelling irradiance is also attenuated; this attenuation is expressed by $(-\kappa z)$, where κ is the vertical attenuation coefficient of the flux scattered upward from the thin layer of water. According to Kirk (1989), this vertical diffuse attenuation coefficient is different from K_d because the angular distribution of upward-scattering photons biased toward small angles to the horizontal, where the photons get extinguished more quickly. This bias toward small angles is due to the shape of the volume scattering function. Many measurements of K_d exist, but κ is not directly measurable. In the middle of the euphotic zone, defined as the depth at which the downward irradiance is 10% of that penetrating the water surface, it is assumed $\kappa \sim 2.5K_d$. The contribution, then, of the infinitely thin layer to the upwelling irradiance just below the surface, $dE_u(z \rightarrow 0)$, is

$$dE_u(z \rightarrow 0) = b_{bd} E_d(0) \exp[-(K_d + \kappa)z] dz \quad (2.38)$$

One of the assumptions made in this model is that b_{bd} , K_d , and κ do not depend on depth. Maritorena et al. (1984) derive the reflectance, $R(0,H)$ below the surface of a homogeneous ocean with a reflecting bottom located at a depth of H , as

$$R(0, H) = R_\infty + (A - R_\infty) \exp[(-K_d + \kappa)H] \quad (2.39)$$

In Eq. 2.39, A = bottom albedo, R_∞ = reflectance of the infinitely deep ocean, K_d = vertical attenuation for downwelling irradiance, and κ = vertical attenuation coefficient of the flux scattered upward from a thin layer of water. This equation (2.39) is the same as Philpot's (1989) equation 4 in the paper in which he describes his principal components algorithm, implemented in this research. The above equation is simplified because as mentioned earlier, κ is not directly measurable, and is specific for each situation. The following equation is considered by O'Neill and Miller (1989) as the most familiar form for shallow water reflectance.

$$R(0, H) = R_\infty + (A - R_\infty) \exp(-2KH)$$

(2.40)

However, as Maritorena et al. (1994) suggest, the use of $2K_d$ results in an underestimate of the actual attenuation experienced by the albedo difference, $(A - R_\infty)$.

Gordon and Brown (1974) discuss five factors that affect the diffuse reflectance, R_d , of a flat homogeneous ocean with a Lambertian bottom: scattering albedo (ω_0), bottom albedo (A), total attenuation coefficient (c), a parameter that relates to the scattering phase function, and the bottom depth z_B , in addition to the incident irradiance distribution. It is possible to determine water depths even out to depths of 20-30 m in good conditions (i.e. clear water) from R_d if the optical properties and the characteristics

of the bottom are known. They found that the bottom can have a large impact on the diffuse reflectance, especially at small optical depths, ζ , defined here as

$$\zeta(\lambda, z) = \int_0^z K_d(\lambda, z) dz \quad (2.41)$$

where K_d = downwelling irradiance attenuation coefficient over the subsurface depth z . The symbol, ζ , refers to optical depth in this section, as in Bukata's definition, whereas ζ will be used as a constant in the derivation of the linear multi-band algorithm in Section 2.4.3. According to Bukata (1995), if K_d is the average value of the irradiance attenuation coefficient over the depth interval, the following holds true:

$$\zeta(\lambda, z) = K_d z \quad (2.42)$$

In very clear waters, which have a low value of K_d (i.e., low concentrations of both organic and inorganic materials, and the scattering and absorption is determined primarily by the water molecules themselves), optical depth can at times equal the actual physical aquatic depth. More turbid waters have a higher value for K_d and therefore, the optical depth will be different than the actual physical depth. In highly absorbing waters with a highly reflective bottom, the scattering due to the bottom will play a large role at small ζ , and a negligible role at large ζ . In highly scattering waters, the bottom scattering contributes greatly to the reflectance, even at larger optical depths. Therefore, not only

does the diffuse reflectance depend on the depth of the water and the turbidity, it depends on whether the turbidity is due to scattering or absorption. It is necessary to determine the optical properties of the water when quantitatively studying bathymetry using remotely sensed data.

These models for shallow water reflectance will aid in developing methods for mapping bottom types and water depth using remotely sensed data. Some of these methods are discussed in the next section.

2.4 Previous Efforts In Bottom Mapping and Bathymetry

Previous efforts have been made to map the bottom of coastal areas and determine water depths using remotely sensed data. Some of the earliest techniques used photointerpretation and photogrammetry of black and white photos. A study of the bottom configuration in Tampa Bay was conducted in 1971 using photogrammetry (Rosenshein et al. 1977). Photogrammetry is a part of the quantitative analysis of remotely sensed data, and uses photographic images to measure height, size, and location of objects (Schott 1997). Photogrammetric analysis of water depths is difficult for a number of reasons. The apparent water depth must be multiplied by a factor that accounts for the refractive index at the air-water interface. Waves at the surface compound the refractive index problem. Also, the location of the cameras can have an impact on the accuracy of depth estimates (Tewinkel 1963). Some early work with pulsed laser technology from an airborne platform yielded accurate depths but was

limited by data recording rates and rate of coverage (Hickman and Hogg 1969). Recent efforts involve techniques which take advantage of multispectral images. Methods dating from the 1960s depended on the ability to find a relationship between water depth and reflected radiance, but these methods require that the properties of the water and the bottom reflectance be uniform (Lyzenga 1985). More often than not, the properties were not uniform and therefore, other techniques were developed.

2.4.1 Single Band Reflectance Model

A simple reflectance model (Jerlov 1976) for remotely sensed bathymetry from multispectral images is given by the following equation

$$L_i = L_{i\infty} + c_i \cdot R_{ai} \cdot \exp(-2k_i \cdot z) \quad (2.43)$$

where L_i is the radiance value in band i , $L_{i\infty}$ is the average signal over deep water, c_i is a constant that is a function of several optical parameters, R_{ai} is the bottom reflectance in band i over bottom type a , and k_i is the diffuse attenuation coefficient. In order to solve for water depth, this equation can be inverted to solve for z . The disadvantage of this method is that it assumes that the bottom reflectance is constant over the bottom type, the atmosphere and water surface conditions are invariant, and also that other background optical effects are either uniform or constant over the scene (Clark et al. 1987).

2.4.2 Ratio Method

Using more than one spectral band is more accurate than using a single band in determining water depth, since the single band method does not account for variation in bottom type (Paredes and Spero 1983). The governing equation for determining water depth based on a reflectance model is similar to that of equation (2.43) above, with different notation,

$$L_i = L_{si} + k_i r_{Bi} \exp(-\kappa_i f z) \quad (2.44)$$

where

L_i = Radiance in band i at depth z

L_{si} = radiance over deep water

k_i = a function of the solar irradiance, the transmittance of the air and water surface, and the refraction at the water surface

r_{Bi} = bottom reflectance at the location where the depth is z

κ_i = effective attenuation coefficient of the water

f = accounts for the path length through the water

If spectral bands exist such that the ratio of the bottom reflectance in the bands is constant throughout the scene, an equation independent of depth can be found

$$(r_{A1})^{C1} (r_{A2})^{C2} = (r_{B1})^{C1} (r_{B2})^{C2} = \dots = \alpha \quad (2.45)$$

where $C1$, $C2$, and α are chosen to make the equality of the bottom reflectance ratios true. A , B ... in the above equation represent different bottom types. Assuming that a pair of bands exists such that the ratio of the bottom reflectances in the two bands is the same

for all of the bottom types in the scene, z is solved for as a function of light intensity, valid for all bottom types. Another way to write the assumption is

$$\frac{r_{A1}}{r_{A2}} = \frac{r_{B1}}{r_{B2}} = \dots = R_b \quad (2.46)$$

Then, Eq 2.45 can be inverted and solved for depth, according to the following equation

$$z = \frac{1}{(x_1 - x_2)f} \left[\ln\left(\frac{k_1}{k_2}\right) - \ln\left(\frac{R}{R_b}\right) \right],$$

where $R = \frac{(L_1 - L_{s1})}{(L_2 - L_{s2})}$ (2.47)

The advantage of this technique is that the depth is not affected by a change in bottom type nor a change in water quality if $(\kappa_1 - \kappa_2)$ stays constant. The limitations of this technique are that one must find the wavelengths that satisfy the criterion that the ratio of the bottom reflectances in the two bands is the same, and the criterion that the attenuation coefficient remains constant, which indicates that the depth is insensitive to changes in water quality. A pair of wavelengths may not exist which satisfy these assumptions; therefore, it may not be possible to determine the water depth using this technique (Lyzena 1978).

A similar ratio method can also be used to classify the bottom composition. This algorithm makes use of the existence of two bands for which the attenuation coefficients

(absorption coefficient plus scattering coefficient), α , are the same, which removes the depth dependence from the model in Eq. 2.44, reducing the ratio to

$$R = \frac{(k_1 r_{B1})}{(k_2 r_{B2})} \quad (2.48)$$

Lyzenga (1985) cites higher spatial resolution as an advantage of this technique. The disadvantage of the technique is that it requires water depth calibration and is more sensitive to environmental parameters. Using this technique, Wezernak and Lyzenga (1975) mapped the distribution of algae (cladophora) in Lake Ontario in 1972. Equation 2.49 describes the bottom-reflected signal received at the sensor, not including atmospheric effects.

$$V = V_s + K \rho e^{-(\sec\theta + \sec\phi)\alpha z} \quad (2.49)$$

where

V = voltage received

V_s = surface reflectance

K = constant which incorporates solar irradiance and scanner characteristics

ρ = bottom reflectance

θ = viewing angle (from vertical)

ϕ = solar illumination angle (from vertical)

α = volume attenuation coefficient (absorption coefficient plus scattering coefficient)

z = water depth

Lyzenga's approach involves using a ratio of two spectral bands that have similar attenuation coefficients (α). In order to do this, the following conditions must be met:

1) the attenuation coefficients in the two spectral bands must be equal or assumed so, and
2) there must be significant contrast between the bottom reflectances of the cladophora and other bottom features in the spectral bands chosen. Therefore, $\alpha_1 = \alpha_2$, and the signals received in the two different channels are then proportional to the bottom reflectance, but independent of depth. Figure 2.9 shows an example of the ratio imagery produced by this method. The dark areas are those occupied by cladophora, as verified by ground truth collected in the nearshore region from 5 transects extending into the lake.



Fig. 2.9 Ratio Imagery, Site 5, North Hamlin Beach (Lyzenga and Wezernak 1975 Figure 4)

This technique is limited to bands for which the attenuation coefficients are equal, which is not true in every situation. There is also a limitation to the materials one can distinguish because the bottom reflectance ratios for the different materials must be different. For example, the method is unable to distinguish between sand and mud bottoms because they have similarly shaped reflectance spectra. Lyzenga (1978) makes a very important point when he indicates that the ratio method worked for the cladophora case because “the vegetation reflectance has distinctive features (due to chlorophyll

absorption) in the blue-green region of the spectrum where the water attenuation is at a minimum.”

Although more flexible than the single-band method, these band ratio methods are limited because they only take advantage of two bands.

2.4.3 Other Multispectral Methods

From multispectral data, Lyzenga (1981) derives bottom depth information, which depends on the relationship that the bottom-reflected radiance varies linearly with bottom reflectance and exponentially with depth, according to Equation 2.50 (Lyzenga 1978),

$$L_i = L_{si} + k_i r_{Bi} \exp(-\kappa_i f z) \quad (2.50)$$

where

L_i = measured radiance in band i

L_{si} = deep water radiance

k_i = a constant which includes the solar irradiance, transmittance of the atmosphere and the water surface, and the reduction of the radiance due to refraction at the water surface

r_{Bi} = bottom reflectance

κ_i = effective attenuation coefficient of the water

f = a geometrical factor to account for the pathlength through the water

z = water depth

Lyzenga (1978) modifies Eq. 2.50 to include the effects of scattering in the water and internal reflection at the water surface; examination of the model indicates that the scattering term has the same depth dependence as the bottom-reflected radiance.

His algorithm defines a new variable, X_i , that varies linearly with depth,

$$X_i = \ln(L_i - L_{si}) \quad (2.51)$$

The variables, X_i s, that result from the above equation are approximately linear functions of depth and are related to each other linearly for the same bottom type. Therefore, if the X variables from two different bands, X_i and X_j , are plotted against one another, the points will fall along a straight line, with a slope of K_i/K_j where K is the irradiance attenuation coefficient, which was defined in Section 2.1.3.3. Analysis of the correlation between the variables yields the ratio of the attenuation coefficients in the two wavelength bands used. Figure 2.10 (Lyzenga's Figure 1b) is an example of the linearized space where bands 5 and 7 are plotted against one another (Lyzenga 1981).

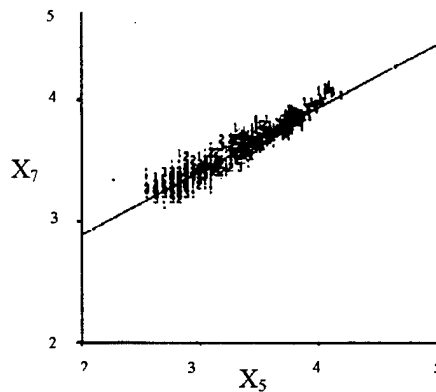


Figure 2.10 Scatter plot of X-values for aircraft bands C5 and C7

When the bottom reflectance changes, the data will fall along a parallel line which is displaced from the first line. Another variable, Y , can be defined which measures the amount of this displacement between the lines, given by

$$Y_i = \frac{K_j \ln(L_i - L_{si}) - K_i \ln(L_j - L_{sj})}{\sqrt{(K_i^2 - K_j^2)}} \quad (2.52)$$

by geometric reasoning, where K_i is the irradiance attenuation coefficient of the water in band i . Y_i is independent of water depth and is related to the bottom reflectance as in Eq. 2.53, assuming that the bottom-reflected radiance ($L_i - L_{si}$) is proportional to the bottom reflectance and varies exponentially with water depth according to

$$Y_i = Y_{i0} - \frac{K_j \ln r_i - K_i \ln r_j}{\sqrt{(K_i^2 - K_j^2)}} \quad (2.53)$$

where r_i is the bottom reflectance in band i and Y_{i0} is a constant for fixed illumination and atmospheric conditions.

The variable Y then acts as a depth-invariant index for the bottom type. This algorithm depends on having a priori knowledge of the attenuation coefficients. To use this technique, an area of uniform bottom type must be selected, which requires knowledge about the scene. One method for determining areas of uniform bottom type is

a clustering routine on scatter plots of the data; the higher the uniformity of the bottom, the higher the correlation is between the spectral bands in linearized space, as can be determined by an inspection of the scatter plots. Figure 2.7 is a scatter plot of data over a sand bottom, and shows high correlation between X_5 and X_7 , indicating high uniformity of the bottom type. The ratio of water attenuation coefficients can then be determined by regression.

Lyzenga (1981) applied this algorithm to aircraft and Landsat data of North Cat Cay, Bahamas. His results for the aircraft data were reasonably accurate in mapping bottom reflectance variations without knowledge of the water depth. The Landsat results were not nearly as accurate because only one of the spectral bands could penetrate deep enough into the water, and Landsat has poorer spatial resolution, which makes it more difficult to select an area in which the bottom is uniform.

Another technique for reducing depth dependence defines a variable Y ,

$$Y_i = \sum_{j=1}^N A_{ij} X_j \quad (2.54)$$

which is obtained by rotating the coordinate system so the Y_N axis is parallel to the direction of changing depth (Lyzenga 1978). If the linear transformation is a pure rotation, Y_N will only be dependent on the water depth assuming this is the primary parameter affecting the brightness, while the remaining variables are functions of the bottom reflectance. Lyzenga states that this is similar to principal component analysis

only in that it involves a rotation transformation. The transformation removes the depth dependence from all but one variable, and does not necessarily reduce the number of variables. This method is better than the ratio method because it does not require that the wavelength bands have equal water attenuation coefficients or that there are equal bottom reflectance ratios for all bottom types. However, the method is more complex.

Lyzenga (1985) also presents another technique for mapping bathymetry, which is a hybrid of both an active and a passive technique. He makes use of pulsed laser technology by using it to calibrate the passive multispectral data for depth. The advantage of this technique is that it does not rely on sea-truth data for depth calibration. This technique incorporates the laser's accuracy in determining depth with the higher spatial resolution of the multispectral scanner (MSS).

Clark et al. (1987) describe another technique for determining depth, the linear multiband algorithm. This method gives the depth by

$$z = \sum \omega_i (1/2k_i) [\ln(c_i \cdot R_{ai}) - X_i] \quad (2.55)$$

where the symbols are defined above in equation 2.50, $X_i = \ln(L_i - L_{i\infty})$ where $L_{i\infty}$ is the average signal over deep water, and the sum is taken over several bands with the constraint that the weights, ω_i , sum to one ($\sum \omega_i = 1$). The testing of this algorithm involved the use of 600 points of known depth for georeferencing. Three hundred of these points were used in a regression fit of the model equation, while the remaining 300

were used to test the calculated depth against the actual depth. The deep-water signals ($L_{i\infty}$) were subtracted from the corresponding L_i values in order to correct for atmospheric scattering, etc. This linear multiband method builds on the two-band ratio assumption that two bands can be found for which the ratio $c_1 R_{a1}/c_2 R_{a2}$ remains constant over different bottom types. The assumption that the ratio $c_1 R_{a1}/c_2 R_{a2}$ remains constant is generalized by assuming that there are constants ζ_i and α independent of bottom type a , so

$$(c \cdot R_{a1})^{\zeta_1} \cdot (c_2 \cdot R_{a2})^{\zeta_2} \cdot (c_3 \cdot R_{a3})^{\zeta_3} K = \alpha \quad (2.56)$$

Certain weights can be found so that when used in Eq 2.55, an equation for z is produced where z is independent of bottom reflectance, R_{ai} , and depends only on the values ζ_i :

$$z = \left(\frac{1}{2} \sum \zeta_i k_i \right) (1 - \zeta_1 X_1 - \zeta_2 X_2 - K) \quad (2.57)$$

This equation may be written in a more generalized form. The following equation is for a two-channel model

$$z = A_0 + A_1 X_1 + A_2 X_2 \quad (2.58)$$

The coefficients A_0, A_1, \dots, A_n are constants that are independent of the bottom type at which the depth is being calculated. A linear regression is performed on the model equation against the calibration points from which the outputs are the coefficients A_0, A_1, \dots which can then be used in equation 2.58 to determine depth. The linear multi-band algorithm (Clark et al. 1987) performed better than the band ratio method (Lyzena 1978) applied to the same data. However, both models underestimated the depth in shallow areas and overestimated the depth in deeper areas. In addition to performing better than the ratio method, the linear multi-band method did not depend on clustering and classification routines to find areas of similar bottom reflectance.

Another method for mapping bottom reflectance and determining depth is found in Bierwirth et al. (1993). The method involves separating the effect of water depth variation from the spectral nature of the substrate. The algorithm derives both substrate reflectance and depth. The algorithm assumes that the water is relatively clear and there are only small variations in the concentrations of water column components. They tested their approach using data from Hamelin Pool, Shark Bay, Western Australia, and therefore, met this assumption because that area is characterized by shallow, clear water. The algorithm applies a constraint, which standardizes the sum of the logarithms of band substrate reflectances. One of the problems with this algorithm is that it derives a value for the attenuation coefficient specifically for Hamelin Pool, Shark Bay, Western Australia. Unless the waters one is working with are similar to these Australian waters, attenuation coefficients would have to be derived from known bathymetric data. The

advantage of this algorithm is that it removes the effect of water depth variation and retains the spectral nature of the substrate.

2.5 Principal Components Method

The principal components algorithm was developed by Dr. William Philpot (1989) and is a generalization of Lyzenga's approach (1978). The benefit of this algorithm is that it extracts depth information and bottom type information even when the conditions are not ideal. Philpot begins with a very simple radiative transfer equation,

$$L_d = L_b \exp(-gz) + L_w \quad (2.59)$$

L_d = radiance observed at the remote detector
 g = an effective attenuation coefficient of the water
 z = depth of water column
 L_b = radiance term which is sensitive to bottom reflectance
 L_w = remotely observed radiance over optically deep water

The model assumes that the optical properties of the water are vertically homogeneous. For the shallow waters that are being considered here, this seems to be a reasonable assumption, although the results will show the limitations of the assumption. The coefficient g is a two way attenuation coefficient and is defined according to

$$g \approx k_d + aD_u \quad (2.60)$$

where k_d is the diffuse attenuation coefficient for downwelling light that was defined above, a is the beam attenuation coefficient, and D_u is the distribution factor for upwelling irradiance. As discussed in Kirk (1989), the distribution factor for upwelling

irradiance is different from that of the downwelling irradiance since the angular distribution of the photons scattered upward is biased toward the horizontal. The term g is approximately equal to the attenuation for downwelling light plus the attenuation for the upwelling irradiance.

In order to quantitatively solve for depth, L_d , L_b , g and L_w must be known. Past methods (Lyzenga 1978) (Paredes and Spero 1983) (Spitzer and Dirks 1987) have assumed that some of these terms are constant over the scene. They also assume that the radiance observed over deep water is constant. Next, they obtain L_d for two or more known depths. With a system of two equations and two unknowns, they solve for L_b and g . Philpot (1989) describes a more complete radiative transfer equation, which includes atmospheric effects, sea state, water reflectance, and other terms in order to generate a synthetic data set upon which to implement his algorithm. He demonstrates that his principal components algorithm works on his synthetic data. The present research implements the algorithm on an actual scene in order to derive qualitative bottom type and depth maps.

Philpot describes three cases in his paper. For the purposes of this research, the case 2 assumptions of variable depth and variable bottom type will be made. Under case 2, L_w and g are still assumed to be constant over the scene and the water is assumed to be vertically homogeneous. A deep-water correction, defined in Eq. 2.61, can be performed because L_w is assumed constant. This procedure defines a new variable, X ,

$$\begin{aligned}
X &= \ln(L_d - L_w) = \ln(L_b) - gz \quad \text{when } L_d - L_w > 0 \\
&\text{and} \\
X &= \ln(L_w - L_d) = \ln(-L_b) + gz \quad \text{when } L_d - L_w < 0
\end{aligned}
\tag{2.61}$$

Usually, it is assumed that $L_d - L_w > 0$ because the bottom reflectance is typically greater than the water reflectance. The ratio methods discussed earlier used a ratio of measurements taken in different spectral bands, which resulted in an improvement in the depth estimate over a single spectral band. It follows that using even more spectral bands will improve the results.

A new variable is defined, Y , according to

$$Y = a \bullet X = a \bullet \ln(L_b) - (a \bullet g)z
\tag{2.62}$$

- Y = a scalar variable
- $X = \ln(L_d - L_w)$, a linearized measurement vector
- g = an effective spectral attenuation coefficient vector
- a = unit vector of arbitrary coefficients

The components of the vectors represent different spectral bands. When using two bands, Eq. 2.62 is reduced to the band-ratio model when $a = r = (1, -1)$. Using this method (Eq. 2.62) with the two-band approach discussed above shows that the two band coefficients are not optimal. However, optimal coefficients can be determined using eigenvector analysis, from which the first eigenvector consists of the optimal coefficients for determining depth. This optimal unit vector is referred to as $a_{||}$, highlighting its parallel relationship to the direction of changing depth in linearized measurement space. Fig. 2.8 is a scatter plot from Philpot's article (1989) of X at 550 nm vs X at 650 nm

which demonstrates how depth varies linearly and how the optimum coefficient vector, \underline{a} , points in the direction of maximum variance.

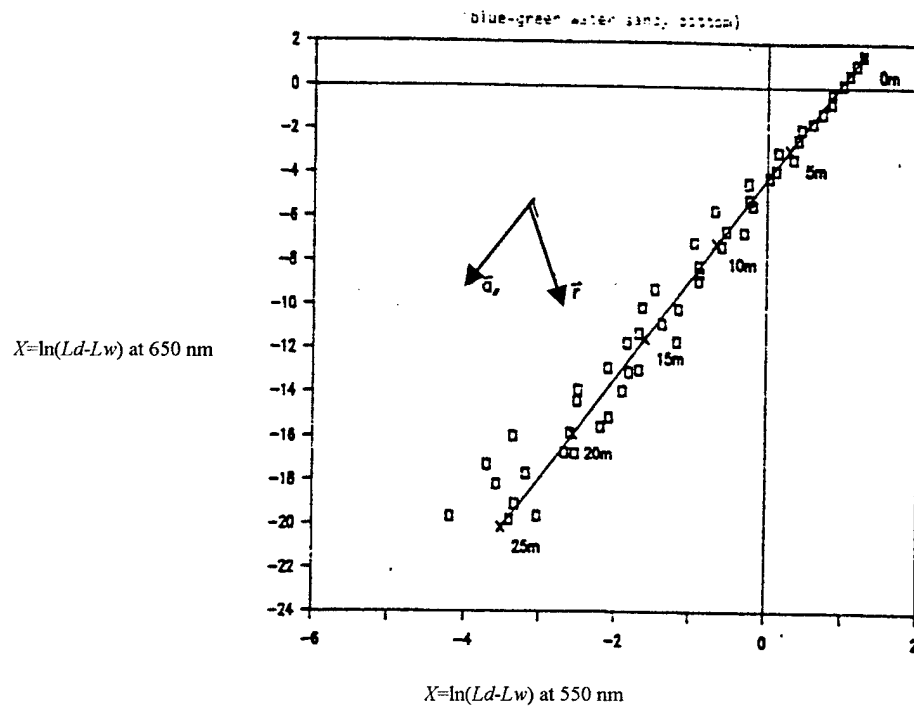


Figure 2.11 Linearized radiance data for the two-band case. (Philpot 1989 Fig. 1)

Fig. 2.12 shows how much of an improvement the optimal coefficients are over the ratio coefficients ($a = (1, -1)$) when applied to Philpot's (1989) synthetic data.

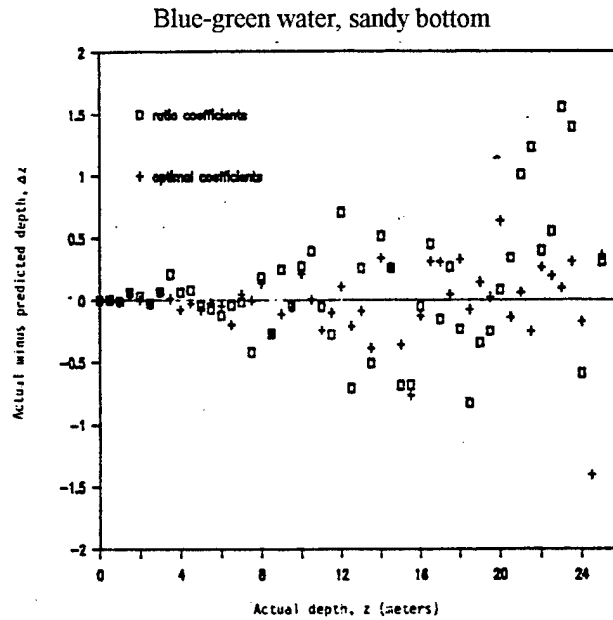


Figure 2.12 Comparison of noise in predicted depth using simple ratio vs optimal coefficients (Philpot 1989 Fig. 2)

For case 2 situations, the data form separate but parallel clusters in the linearized measurement space (X_1, X_2) in Fig. 2.13. For this reason, adequate difference is required in bottom reflectance between the various bottom types in order to distinguish between clusters. Each of these clusters will be aligned with the optimal coefficient vector, \underline{a}_j . The scalar variable, $Y_{||}$, defined in Eq. 2.62 will be sensitive to depth for each bottom type if an eigenvector analysis of each bottom type is performed. In order to obtain the absolute depth information, L_b must be known for each bottom. This can be found using the system of two equations in two unknowns, which requires L_d for two known depths over each bottom type.

The clusters in linearized space are separated by a certain distance, which is related to the difference between the bottom reflectances. This separation can be seen in Figure 2.13, a scatter plot (Philpot 1989), in which shows synthetic data for three different bottom types (sand, silt, and vegetated).

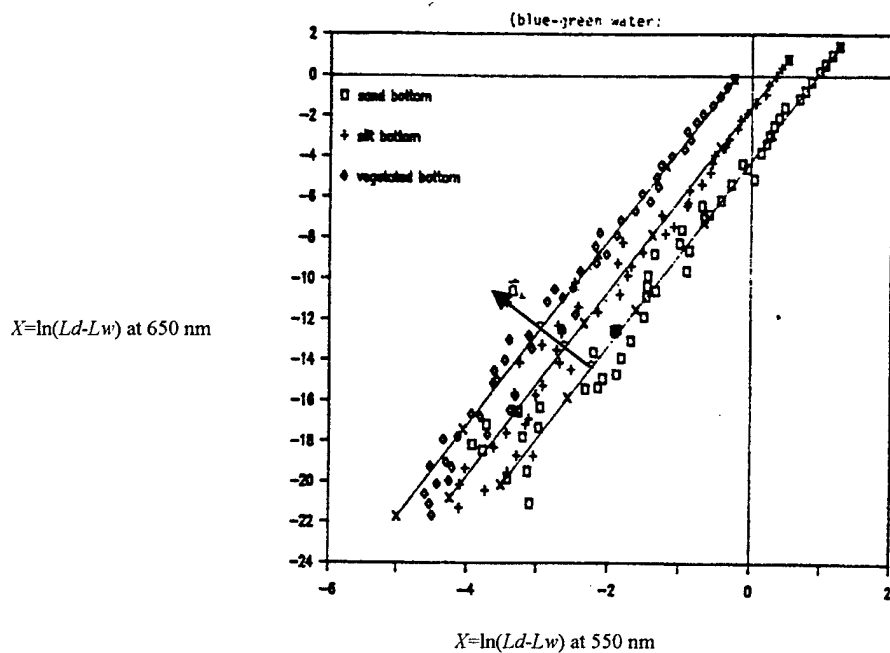


Figure 2.13 Linearized radiance data - constant water, but varying depth and bottom type (Philpot 1989 Fig. 3)

A second vector, \underline{a}_\perp , is perpendicular to the optimal coefficients vector (\underline{a}_\parallel) and characterizes Y_\perp , which is independent of depth but sensitive to the bottom type. The vector \underline{a}_\perp is perpendicular to \underline{a}_\parallel , which is parallel to \underline{g} , so that $\underline{a}_\perp \bullet \underline{g} = 0$. Y_\perp is a scalar variable independent of depth according to:

$$Y_{\perp} = a_{\perp} \bullet X = a_{\perp} \bullet \ln(L_b) \quad (2.63)$$

showing that the bottom type may be characterized by the scalar variable Y_{\perp} .

Philpot's (1989) Case 3 includes varying water type in addition to varying depth and bottom type. He indicates that using a single deep-water observation to linearize the entire data set when different water types exist can result in nonlinearities and errors unless the effective attenuation coefficients of the different water types are spectrally proportional. The absolute depth prediction equation determined for one water type may yield incorrect results when applied to another water type. Therefore, L_b , L_w , and g and the optimal coefficient vector, \mathbf{a} , would need to be determined for each water type.

Theoretically, these parameters can be estimated if at least three depths are known for each water type, which requires that the depths must be assigned to their respective water types prior to analysis. Another difficulty exists if two pixels representing two different depths and different bottom types are spectrally identical. A preferable method for working with an image containing different bottom types is to partition the image into areas based on water type. Then, the appropriate deep-water pixels can be selected to perform the linearization of the data.

2.6 Choosing the Method

The principal components algorithm (Philpot 1989) described in Section 2.5 was chosen because it seemed the most straightforward to implement. The single band reflectance model (Jerlov 1976) assumes that too many factors are constant – bottom

type, atmosphere, and water surface conditions. The two-band ratio methods yield more accurate results than the single band model. However, the two-band method have other limitations. The ratio methods require that the attenuation coefficients remain constant or that the ratio of the bottom reflectances in the two bands is the same (Paredes and Spero 1983). A pair of wavelengths that satisfy either of these criteria may not exist (Lyzenga 1978). Also, when using a similar ratio method to distinguish between different bottom types, there must be sufficient difference in their reflectances (Lyzenga and Wezernak 1978) in addition to meeting the condition that the attenuation in the two spectral bands must be equal. Additionally, this technique requires water depth calibration and is more sensitive to environmental parameters. Some of the other methods require a priori knowledge or the ability to derive attenuation coefficients that are specific for a particular area (Bierwith et al. 1993). These methods only take advantage of two bands. The attractive feature of the principal components algorithm is that it takes advantage of the numerous bands in a hyperspectral image. The algorithm extracts both depth and bottom type information even when the conditions are not ideal. The other algorithms reviewed looked at either determining water depth or determining bottom type, but not both in the same algorithm. The assumption at the start of the research using Philpot's (1989) algorithm is that the water type is constant. The results will show that this assumption, while not valid over the entire image processed, was more valid over smaller portions of the image, carefully selected to approach the assumption of constant water type.

Chapter 3

Methods

The approach taken in this research involves the use of various methods and tools. An understanding of these methods, to include their strengths and weaknesses, must be understood prior to a discussion of the approach taken.

3.1 Principal Components Analysis

The final method for bottom type classification and water depth determination discussed in Chapter 2 was Philpot's (1989) principal components algorithm, selected for implementation in this research. Some of the benefits of this algorithm include ease of implementation and capability to take advantage of hyperspectral information in addition to providing both depth and bottom type information. These advantages result from the use of principal components analysis to transform the linearized data (X s) into eigenvectors by finding the variability in the data.

Each pixel of the MISI images, to which the algorithm was applied, contains a spectrum of calibrated radiance values in 63 bands. The variations in the spectra are related to depth, bottom type, water type, and other changing conditions which contribute to the signal in addition to the instrument variations such as detector noise, etc. Yet, there exists some amount of independent variation in the spectral data. The PC method finds the variability in the data. It is the assumption of this research that the largest

variations in the radiance spectra are due to the different input factors, such as depth, bottom type, and water type, especially after linearizing the data (Sec. 2.5). PCA breaks down spectra into their most significant variations, where the variation spectra are known as eigenvectors, or principal components. Eigenvectors are useful in many areas of math and science. The basic eigenvalue equation,

$$Av = \lambda v \quad (3.1)$$

is satisfied for certain λ and v , the eigenvalues and eigenvectors. A is a square (usually symmetric) matrix, and λ is an eigenvalue of A , found by solving the following equation,

$$\det(A - \lambda I) = 0 \quad (3.2)$$

where I is the identity matrix. Once the eigenvalues are found, the eigenvectors can be found.

In order to implement this Principal Components Algorithm, the principal components must be obtained through eigenvector analysis. The eigenvector corresponding to the largest eigenvalue of the covariance matrix indicates the direction of greatest variance. The covariance matrix is defined as

$$\Sigma = \begin{bmatrix} \sigma_{11} & \sigma_{12} & \dots & \sigma_{1d} \\ \sigma_{21} & \sigma_{22} & \dots & \sigma_{2d} \\ \dots & \dots & \dots & \vdots \\ \sigma_{d1} & \sigma_{d2} & \dots & \sigma_{dd} \end{bmatrix}$$

where

$$\sigma_{xy} = \frac{1}{n} \sum_{i=1}^n (x_i - \bar{x})(y_i - \bar{y}) \quad (3.3) \quad (3.4)$$

The second-largest eigenvector indicates the direction of greatest variation perpendicular to the first eigenvector. These are the two eigenvectors that are required to implement the principal components algorithm (Philpot 1989). Eigenvectors can be used to predict what the unknown inputs were and are often used in place of the original spectra when doing inverse least squares regression. This procedure of using the principal components in place of the original spectra in regression is called Principal Components Regression (PCR) and is defined in Sec. 3.3.

An advantage of using principal components analysis is that it separates out the factors that are independent of each other, although there is no guarantee that these factors have physical meaning. One limitation of PCA is that there can be problems with collinearity, if the spectra share the same variations, although different in magnitude.

The PC analysis was performed in IDL using a publicly available program called PCA.PRO which is located on the internet at the following website, <http://idlastro.gsfc.nasa.gov/contents.html>. A copy is located in Appendix B along with the IDL program used to implement Philpot's principal components algorithm on an

image. This program is based on the PCA method in Murtaugh and Heck (1987). The PCA.PRO program standardizes the variables, i.e. it corrects each observation for its mean and standard deviation. Mean centering is important because it enhances the subtle differences between spectra, essentially removing the first most common variation before the data is processed by the PCA algorithm. PCA.PRO also normalizes the eigenvectors by the square root of the eigenvalues.

PCA is used in the algorithm implemented in this research to determine qualitative bottom type and water depth maps. One of the goals of this research was also to determine quantitative depth information without extensive ground truth, using a procedure, principal components regression. PCR combines the benefits of principal components analysis with regression.

3.2 Regression

Regression analysis is a statistical method for predicting values of dependent variables (Y) from a collection of independent variables (X). Regression is used to find the relationship between the Y s and the X s by estimating the regression coefficients from the regression equation, $Y=Xb$. For multiple variables, a linear relationship can be assumed in order to form a linear regression, as in the following equation,

$$Y = b_0 + b_1X_1 + b_2X_2 + K + b_pX_p$$

(3.5)

where p = number of observations, \underline{Y} = independent variables, \underline{X} = dependent variables, and b = a vector of regression coefficients. The regression coefficients are solved for according to the following equation,

$$\underline{b} = \underline{X}^{-1}\underline{Y} \quad (3.6)$$

An estimate of the inputs (\hat{Y}) is obtained by plugging \underline{X} into the equation, $\hat{Y} = \underline{X} \underline{b}$ using the regression coefficients, b , found in Eq. 3.6. The regression coefficients are determined such that the sum of squares of error is minimized,

$$\min \sum_i (y_i - \hat{y}_i)^2 \quad (3.7)$$

The problem with inverse least squares regression is that the number of variables cannot exceed the number of observations due to the dimensions of the matrices. Theoretically, adding additional observations should allow for additional variables; however, the observations tend to decrease and increase together as the constituents of the observation spectra change, known as collinearity. An additional concern while using regression is overfitting, which occurs at the point when adding additional variables no longer increases accuracy, but instead the prediction accuracy gets worse. Combining

regression with the principal components analysis discussed in the previous section yields a procedure called principal components regression.

3.3 Principal Components Regression

One of the concerns in implementing Philpot's (1989) principal components algorithm on the MISI images was that the pc algorithm assumes constant water type. An early thought in this research was that quantitative depth and bottom type information could be obtained through PCR because the regression coefficients would be determined from HydroMod model data where water type was varied in known amounts along with depth and water type. Then, depth and bottom type could be determined regardless of varying water type, and the need for extensive ground truth would be eliminated because the regression coefficients are determined from model data.

PCR combines PCA spectral decomposition with the inverse least squares regression method. A spectrum, such as the radiance spectra, which are the expected output of HydroMod, may be represented through PCA by a collection of a series of scores and factors, as in the following figure.

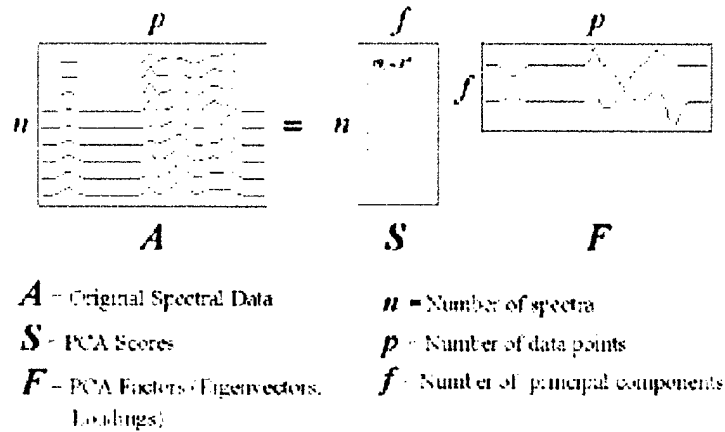


Figure 3.1 PCA (Galactic 2000)

PCA breaks apart the spectral data into the most common spectral variations (eigenvectors) and the corresponding scaling coefficients (scores). For PCR, the regression described in the preceding section was performed not on the \underline{X} matrix itself, but on the scores matrix, which is determined by multiplying the \underline{X} matrix times its principal components.

One of the advantages of PCR is that it reduces collinearity in the observed spectral radiances, which is important in this situation because hyperspectral data are almost always highly correlated. When the predictor variables are highly correlated, it is difficult to obtain a good inverse of $X^T X$; as the predictor variables become more correlated, the same thing occurs to the regression coefficients themselves (Jackson 1991). PCR relates the principal component scores to the variables of interest, and hopefully separates the effects of the variables of interest on the spectra. There is no guarantee that the pca vectors directly correspond to the constituents of interest, although

in this research, the assumption is that the first principal components carries depth information and the second carries bottom type information. Another disadvantage of PCR is that generally, a large number of observations are required for accurate calibration, while still being careful to avoid collinearity. The greatest limitation, with regards to this research, is that PCR does not work on categorical data. The implications of this limitation are discussed in Chapter 5.

The regression coefficients were calculated from the scores, a result of eigenvector analysis of the HydroMod radiance outputs. These radiance spectra were generated by the radiative transfer model, HydroMod, for different bottom types, depths, and water types. The water types that served as inputs to HydroMod were determined from processing of water samples collected at the area of study, the Ginna power plant.

3.4 Water Sampling

Extensive water sampling was undertaken at the Ginna power plant and the Ontario Beach area of Lake Ontario, where the Genesee river empties into the lake. The latter field sampling included stations in Braddocks Bay, Irondequoit Bay, and at the Russell power plant. These field sampling efforts were made throughout the summers of 1999 and 2000. The field sampling used as inputs to HydroMod was made at Ginna on September 3, 1999 and Ontario Beach on July 5, 2000. These samplings were made during an overflight of the MISI aircraft and an overpass by one of the following sensors: AVIRIS, Landsat 5, or Landsat 7. At each water sampling location, various measurements were made and water samples were collected. The GPS coordinates were

recorded at each location in addition to collecting a sample of the water near the surface. Also, secchi depths were determined at various locations and where the water was shallow enough, the secchi disk was lowered to the bottom to determine depth.

3.4.1 Filtering

The water samples were filtered on the same day they were collected. They were filtered onto Whatman GF/F 25 mm filters, which is common practice (Mitchell 1990), (Bricaud and Stramski 1990). A pump was used to create a vacuum which forces the water through three different filters: one used for Total Suspended Solids (TSS), one for Chlorophyll a, and one for particle absorption. The volume of water filtered through each filter was recorded in order to calculate component concentrations. The weight of the TSS filters were recorded prior to filtering in order to calculate the difference between the post-filtered weight and the pre-filtered weight. Each of the filters was placed in a plastic capsules which was labeled according to the water sample number and the component concentration being measured. The plastic capsules with the filters intended for chlorophyll extraction were placed in a bag in the freezer to await analysis. The September 3, 1999 filters were stored for 12 days prior to processing for chlorophyll concentration. The tissue prep capsules help protect the filters from light and ice. The Monroe County Environmental Health Laboratory Standard Operating Procedures located in Appendix C states that if the sample is frozen and kept in the dark, it can be held up to 3 weeks (1996). The particle absorption filters were analyzed immediately.

3.4.2 Particle Absorption

The particle absorption was analyzed using a Shimadzu spectrophotometer. A reference filter was prepared by filtering distilled water through the filter. The spectrum of the reference filter was subtracted from the absorption spectrum measured for each of the sample filters, and the resultant spectra were recorded. The particle absorption spectra were corrected for the multiple scattering effects due to the filter using a quadratic fit:

$$OD_s(\lambda) = aOD_f(\lambda) + b[OD_f(\lambda)]^2$$

(Mitchell 1990) (3.8)

where $OD_s(\lambda)$ is the optical density of phytoplankton in suspension, and $OD_f(\lambda)$ is the optical density of the suspension on a filter. Published coefficients, a and b, given by Cleveland and Weidemann (1993) are currently used in the particle absorption process utilized by the Digital Imaging and Remote Sensing (DIRS) group. The absorption due to particulates was then calculated using the following equation (Mitchell 1990),

$$\alpha_p(\lambda) = 2.3OD_s(\lambda)/l_g \quad (3.9)$$

$l_g = V_f/A_c$, where V_f is the volume filtered, and $A_c = \pi r^2$, with r being the radius of the portion of the filter which contains the particles removed from the suspension. Also, a methanol extraction was done on the filter in order to remove the absorption due to chlorophyll pigment, leaving only the absorption due to TSS.

3.4.3 Chlorophyll a

The chlorophyll filter was removed from the freezer and the concentration of chlorophyll extracted from the filter using the procedure outlined in Standard Methods (Appendix C). The concentrations were derived both spectrophotometrically and fluorimetrically. A comparison was conducted on a few of the samples to determine if the results seemed reasonable. These results are reported along with the results of the water sample processing in Appendix D.

The uncorrected chlorophyll values are used as inputs to HydroMod, which uses the four-component model discussed in 2.1.3.2. Bukata et al. (1981) analyzed the water quality parameters of Lake Ontario using a five component model, the fifth component being nonliving organic component (NLO). They state that it is possible to use a four component model provided that the values of chlorophyll uncorrected for phaeophytin contamination, which thereby includes some detrital component.

3.4.4 CDOM

The absorption spectra of colored dissolved organic matter (CDOM) is also determined using a spectrophotometer. First, the spectrophotometer is zeroed by placing distilled water in both the reference cell and the sample cell (10 cm pathlength). Next, the water sample is filtered using a syringe filter into the sample cell. Then, the absorption spectra is recorded. The concentration of the yellow substance can be expressed as the absorption coefficient at 380 nm, $Y=a_y(380) \text{ (m}^{-1}\text{)}$ (Spitzer and Dirks 1987). The CDOM processing results from the DIRS sampling campaign are recorded as

scalar values as seen in the Results chapter. A mean absorption spectrum was calculated from a wide range of Lake Ontario water and then ratioed against each of the water sample absorption spectra to obtain a scalar value for each sample.

3.4.5 TSS

TSS filters are placed in a heater/dryer that is located in the basement of the CIS building. The heater is set at ~150 °C and the filters are left to dry there for about 24 hours. The post-drying weight of the filters is recorded, the pre-filtered weight is subtracted, and the concentration is determined based on the amount of water that was filtered.

3.5 Bottom Target Reflectance

In addition to varying the water type, bottom type was also varied in the HydroMod runs to produce radiance values in each of the MISI bands. In order to obtain the spectra for each of the bottom types, an ASD spectrometer was used to record reflectances (ASD is the name given to the FieldSpec made by Analytical Spectral Devices, Inc.) The ASD is a portable spectroradiometer that records the reflectance spectra of the object that the “gun” is aimed at and compares it to a reference material with known reflectance properties.

The methods presented here were used as tools in the development of the approach discussed in the next chapter.

Chapter 4

Approach

In this chapter, the background information and methods presented in the previous two chapters is used in the development of an approach to gain knowledge about shallow water from a remotely-sensed image. Just as the band ratio methods improve the accuracy of depth determination over single-band methods, it often follows that using even more bands, such as in hyperspectral imagery, will further improve the results. This work consists of four major parts. First, ground truth was collected including water depths, bottom samples, and water samples. Second, the principal components analysis method was used to perform bottom type classification and water depth determination on a hyperspectral image. The third part of the research involved work with HydroMod to generate sensor-reaching radiances for different depths, bottom types, and water types that were collected in part 1. The fourth part built on parts 2 and 3; a regression was performed on the scores obtained from principal components algorithm analysis of both the image data and the model data and the errors were determined using ground truth.

4.1 The Image

The images used for this particular application were taken by the Modular Imaging Spectrometer Instrument (MISI) constructed by the Digital Imaging and Remote Sensing Group (DIRS) at RIT. MISI is a line scanning hyperspectral sensor with

63 spectral channels from 0.4 μm to 1.018 μm at approximately 0.010 μm intervals.

Table 4.1 shows the Band Centers for MISI.

MISI Band Centers			
	VIS (FWHM=10 nm)		NIR (FWHM=8 nm)
1	418.2962	33	754.044748
2	429.009263	34	762.967334
3	438.465412	35	771.871315
4	448.409214	36	780.87618
5	458.344586	37	789.844196
6	467.972961	38	798.515896
7	477.574686	39	807.440903
8	487.774504	40	825.065944
9	497.398	41	834.01772
10	506.996088	42	842.876596
11	516.928457	43	851.474834
12	526.484894	44	860.375241
13	536.063395	45	868.633836
14	546.026128	46	877.17614
15	555.924146	47	885.87757
16	565.443029	48	893.950338
17	574.95592	49	903.311413
18	584.476584	50	911.152567
19	594.052835	51	919.083669
20	603.982259	52	926.97443
21	613.047188	53	934.554513
22	622.507265	54	942.574798
23	631.955658	55	950.564254
24	641.055941	56	958.448494
25	650.501156	57	965.709716
26	659.530681	58	973.463033
27	668.874578	59	981.01458
28	677.892293	60	988.147481
29	686.558489	61	995.21763
30	695.512074	62	1002.620013
31	704.448606	63	1009.525889
32	713.066255		

Table 4.1 MISI Band Centers for Visible and NIR Bands

An advantage of MISI's hyperspectral nature is that it records a fine spectral resolution electromagnetic profile for each pixel. The wavelength-dependent characteristics in the reflectance spectra reveal important information about the optical properties of water, which can be important in water quality studies. More information about MISI and its calibration can be found in Appendix A.

The MISI images of Lake Ontario were fairly noisy. Steps were taken in order to minimize the effects of the noise. A discussion of the problems with image noise and the steps taken to correct their effects is included in Chapter 5.

4.2 Principal Components Algorithm

Philpot's principal components analysis has been performed on a synthetic data set (Philpot 1989), but there are no published examples of his approach using real data. The website, <http://www.geog.ubc.ca/courses/klink/g472/class98/hamren-larsson/> (Hamren-Larsson 1998) provides information on how a principal components analysis was applied to a Landsat scene. The principal components algorithm was more accurate in predicting depths than the single band algorithm it was compared to. The PCs were linearly regressed against known depth values. However, no bottom type information was determined in this paper although bottom type variation was included as one of the factors that decreased the accuracy of the algorithm. The MISI images contain more spectral bands; and therefore, this research will test to see if more bands increase the accuracy. The algorithm was coded in the software language, Interactive Data Language (IDL) and used on images taken of the Lake Ontario shoreline by MISI in order to map

various bottom types, which were verified using ground truth collected at various points in the image. This information was useful in two ways. First, bottom type mapping near the Ontario Beach area has value to the County Health Lab, which is interested in knowing where the green algae is located. This information will help them address the issue of beach closures, which occurred 13% of the time in 1998 because of cladophora and spirogyra washing up on the beach and decaying. A second possible use of this bottom type map be as a scene in future work with DIRSIG (DIRSIG is a first principles based synthetic image generation model developed by the DIRS program at the Center for Imaging Science (CIS).).

MISI images of the Lake Ontario shore line for summer 1999 and 2000 were available. IDL was used to code the algorithm; the software package, ENvironment for Visualizing Images, ENVI, was used to read in a variety of image formats, filter, classify, and resize images. Following is a list of steps that were taken in applying the principal components algorithm.

4.2.1 Pre-Processing

1. Mask out the land. This was accomplished in ENVI and the land was masked to a value of -1 . The mask value of -1 was chosen over the typical value of 0 to account for any of the water pixels which might have a radiance value equal to 0 . Masking the land increases the accuracy of the principal components analysis on the water areas in the image, because it eliminates the variability of radiance in the land portions of the image.

2. Geo-register the image. The images were manually geo-registered in Arc/Info or ENVI. This was done by matching up a Landsat image of the area containing GPS coordinates to water sampling location GPS coordinates.
3. Select deep-water areas in the image which are considered deep water. Bathymetry data were used to select areas deep enough that the bottom could not be seen. Lyzenga & Schuchman (1979) did so by averaging a set of scan lines in the along track direction in order to obtain the deep-water signal as a function of the pixel number or scan angles. The pixels selected as deep water were averaged to form a single deep-water observation.
4. Address the noise problems, as discussed in Chapter 4.

4.2.2 Deep Water Correction

1. Linearization of data. The simple radiative transfer equation for optically shallow waters is linearized. The parameter X is found, such that

$$X = \ln(L_d - L_\infty) = \ln(L_b) - gz \quad (4.1)$$

2. Plot the data in linearized feature space to visually determine if there are nonlinearities and if there are clusters which indicate different bottom types.

4.2.3 The Algorithm - Depth

1. Form a matrix of all X calculations and perform an eigenvector analysis on the \underline{X} matrix. Use a plot of the eigenvalues in order to determine how many principal components to retain. The SCREE plot method, a graphical technique that retains the

eigenvalues that are to the left of the break in the plot, is used. The last eigenvalues tend to be small and in a straight line; the eigenvalues retained are before the plot levels out. (Jackson 1991) The first principal component is assumed to be the optimal coefficient vector, \mathbf{a}_{\parallel} . Knowing \mathbf{a}_{\parallel} will allow for determination of Y_{\parallel} :

$$Y_{\parallel} = \mathbf{a}_{\parallel} \mathbf{X} = \mathbf{a}_{\parallel} \ln(L_b) - (\mathbf{a}_{\parallel} \mathbf{g}) z \quad (4.2)$$

For the remainder of the discussion, this depth dependent variable will be referred to as \underline{Y} .

4.2.4 The Algorithm - Bottom Type

In addition to depth information, the variation in bottom types will be mapped.

1. For each bottom type, determine \mathbf{a}_{\perp} , which is the eigenvector perpendicular to \mathbf{a}_{\parallel} , and can be used to characterize the depth independent variable \underline{Y}_{\perp} :

$$Y_{\perp} = \mathbf{a}_{\perp} \mathbf{X} = \mathbf{a}_{\perp} \ln(L_b) \quad (4.3)$$

Notice this variable is entirely independent of depth, since \mathbf{a}_{\perp} is perpendicular to \mathbf{a}_{\parallel} , $\mathbf{a}_{\perp} \mathbf{g} = 0$, and the depth-related term drops out of the equation.

2. Use the depth-independent variable for the bottom type, Y_{\perp} , to perform a classification on the image. For this task, the k-means unsupervised classification capability of ENVI will be used. The bottom type map is actually a one band image and

therefore the unsupervised classification is really a gray-level slice which classifies the data in the Y_{\perp} image based on brightness.

The next step is to determine how well the algorithm performed and determine some quantitative information about depth and bottom type. It is preferable to do this without performing an extensive ground truthing effort of diving and sampling the bottom of the lake, so a principal components regression is performed first on the HydroMod radiance values in order to determine regression coefficients which are then applied to the principal component algorithm-processed images (Philpot 1989). This assessment takes advantage of the flexibility of the model, HydroMod. The concentrations of TSS, Chlorophyll a, and CDOM gathered from DIRS data collections were used as inputs to HydroMod. Then, both bottom type and depth were varied in order to generate sensor-reaching radiance values for use in the PCR.

4.3 Inputs to HydroMod

In order to use PCR, the conditions under which the images were taken need to be modeled as closely as possible; therefore, the characteristics of the intervening water column must be known. This requires an extensive water sampling campaign and water processing to determine various concentrations that will serve as inputs to HydroMod. This research takes full advantage of the features of HydroMod which takes into account the atmosphere, water reflectance, water quality, and bottom reflectance in order to provide the sensor reaching radiance. The details of the program HydroMod can be found in Fairbanks (1999). The water sampling and filtering processes were presented in

Chapter 3. The results of this processing and bottom reflectance measurements were used to build the forward model.

4.4 The Forward Model

The inputs to HydroMod will simulate as closely as possible the conditions under which the images were recorded. The components of this forward model built to calibrate the principal components regression (Section 3.3) are shown in Figure 4.1.

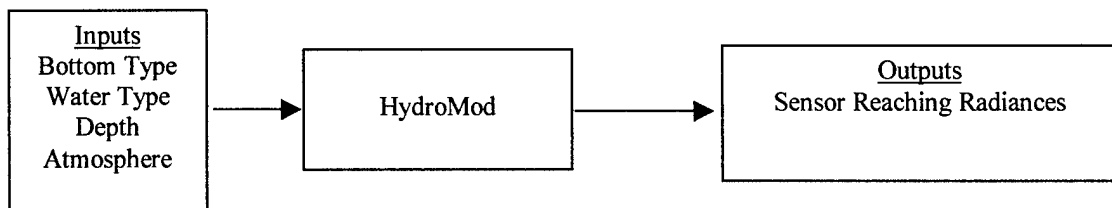


Figure 4.1 Components of the Forward Model

The radiosonde data from the image collection day will be used to calculate the effects of the atmosphere. Radiosonde is a term that refers to the instrument package that collects and transmits meteorological data, and is carried into the atmosphere by a weather balloon. Although HydroMod includes the capability to add clouds to the scene, this option will not be used; because the images were taken on clear days. The water quality parameters are derived from the filtering and subsequent processing of the water samples. The default absorption cross-sections and scattering cross sections (Figs. 2.5-2.8, respectively) are based on Lake Ontario (Bukata 1995) and updated cross-sections determined from water samples collected on May 20, 1999.

A different bottom boundary will be created using the bottom type reflectances discussed in Section 3.5. From the HydroMod User’s Manual, it seems that only a wavelength independent reflectance is allowed if the “User Supplied Constant Reflectance” option is selected. This is not an acceptable option because bottom reflectances vary with wavelength; therefore, HydroMod will need to be modified in order to add the bottom types characteristic of the area captured in the image. The reflectance spectra needed – Lake Ontario sand, cladophora and/or spirogyra, and additional spectra– will have to be collected.

HydroMod runs at various depths with various bottom and water types were made. The resulting sensor-reaching radiance values will be put into a matrix for use in the PCR discussed in the next section. Table 3.3 shows the various depths, bottom types, and water types that will be used in a factorial method.

Bottom Types		Depth (m)	Water Type			
#	Name		Sample	Chl (mg/m ³)	TSS (mg/L)	CDOM (scalar)
1	Ontario sand	0.5	I1	0.934	1.000	0.451
2	Hydromod Green Algae	1.0	A5	1.145	1.000	0.485
3	Gray Rock1_wet	3.0	A3	1.671	1.333	0.481
4	Gray Rock2_wet	5.0	A6	1.698	0.750	0.454
5	Red Rock with algae2	7.0	A2	1.868	1.000	0.467
6	RedRock1_wet	10.0	I4	3.463	2.400	0.438
7	Light gray rock1_wet	30.0				
8	Yellow rock1_wet					

Table 4.2 Inputs to HydroMod

The inputs from Table 4.2 are used to build the forward model, which is then used to calibrate the principal components regression.

4.5 Applying Principal Components Regression to this Research

Principal components regression is a statistical tool that combines principal components analysis with regression. For multiple observations, the independent variable of the regression, \underline{X} forms the matrix defined below for L_{obs} = the dependent variable:

$$\underline{X} = \begin{bmatrix} 1 & Lobs_1(\lambda_1) & \dots & Lobs_1(\lambda_p) \\ 1 & Lobs_2(\lambda_1) & \dots & Lobs_2(\lambda_p) \\ \vdots & \vdots & \ddots & \vdots \\ 1 & Lobs_n(\lambda_1) & \dots & Lobs_n(\lambda_p) \end{bmatrix} \quad (4.4)$$

where p = number of bands and n = number of observations.

Then, the linear regression equation to determine the matrix of regression coefficients, \underline{b} , is

$$\underline{b} = \underline{X}^{-1} \underline{Y} \quad (4.5)$$

which is actually calculated as

$$\underline{b} = (\underline{X}^T \underline{X})^{-1} \underline{X}^T \underline{Y} \quad (4.6)$$

For the PCR, the regression described in the preceding section will be performed not on the \underline{X} matrix itself, but on the scores matrix, which is determined by multiplying the \underline{X} matrix times its principal components. The following equation shows in matrix

form how one principal component score (PC) is obtained by multiplying an eigenvector, \underline{a} , by the data, $\underline{L}(\lambda)$.

$$\begin{bmatrix} PC_1 \\ \vdots \\ PC_n \end{bmatrix} = \begin{bmatrix} a_0 & a_1 L_1(\lambda_1) L & a_p L_1(\lambda_p) \\ \vdots & \ddots & \vdots \\ a_0 & \dots & a_p L_n(\lambda_p) \end{bmatrix}$$

(4.7)

Again, p = number of bands and n = number of observations.

Instead of performing a regression directly on the spectral responses, this method regresses the concentrations on the PCA scores. The PCA scores are the result of transforming the data using the principal components, so in other words, an observation is transformed using the first principal component (eigenvector), resulting in the score. According to Galactic Industries Corp. (2000), using the eigenvectors to calculate the regression instead of the spectral responses themselves “produces a robust model for predicting concentrations of the desired constituents in very complex samples”. This is because the eigenvectors of the principal components analysis represent the spectral variations common to all of the calibration data.

Eq. 4.8 is the principal component regression equation that will be used in this research. The assumption is made that varying depth, bottom type, and water type account for the greatest variation in the data. Therefore, only the first three principal components (PCs) will be retained for the PCR against the dependent variables, depth

(*d*), bottom type (*bt*), and water type (*wt*) from which the regression coefficients, \underline{b} , will be calculated.

$$\begin{bmatrix} d_1 & bt_1 & wt_1 \\ \vdots & \vdots & \vdots \\ d_n & bt_n & wt_n \end{bmatrix} = \begin{bmatrix} 1 & PC1_1 & \dots & PC3_1 \\ \vdots & \vdots & \ddots & \vdots \\ 1 & PC1_p & \dots & PC3(\lambda_p) \end{bmatrix} \begin{bmatrix} b_0 \\ \vdots \\ b_2 \end{bmatrix}$$

$$\underline{Y} = \underline{X} \underline{b}$$

(4.8)

4.5.1 PCR Applied -- HydroMod

The HydroMod runs will be used to calibrate the PCR because both the inputs (depths, water components, bottom types) and the outputs (radiance) are known. In an effort to model the image as closely as possible, the radiosonde file for the day (September 3, 1999) was used to build the sky files in MODTRAN as part of HydroMod. Also, the water components used will be the constituents actually found in the water samples collected in the Ginna area.

The steps for implementing PCR on this data are as follows:

1. Perform deep water subtraction on the \underline{X} matrix by subtracting the radiance values calculated for a depth of 30m, and take the natural log of the data (Philpot's 1989 algorithm).
2. Calculate the covariance of the \underline{X} matrix from Step 1.
3. Determine the eigenvectors. These are the coefficients for the linear combination that maximize the variance in the data. Only the depth, bottom type, and water

type were varied in the HydroMod runs. Therefore, only the first three eigenvectors will be retained (\underline{A}).

4. Determine scores for the retained eigenvectors. $\underline{PC} = \underline{XA}$
5. Perform the regression. Use the pseudoinverse to calculate the regression coefficients, \underline{b} .

$$\underline{b}_{\text{Hydro}} = (\underline{PC}^T \underline{PC})^{-1} \underline{PC}^T \underline{Y} \quad (4.9)$$

The \underline{Y} matrix here represents the inputs to HydroMod

6. Calculate $\underline{Y}_{\text{est}}$. $\underline{Y}_{\text{est}} = \underline{PCb}_{\text{Hydro}}$
7. Compare the results. The depth estimate, for example, is the first column of the $\underline{Y}_{\text{est}}$ matrix. Compare this value to the actual depth input into HydroMod using root mean squared (RMS) error,

$$\frac{1}{N} \sum_{i=1}^n \left(d_i - \hat{d}_i \right)^2 = MSE \quad RMS = \sqrt{MSE} \quad (4.10)$$

4.5.2 PCR Applied - The Image

The next steps involve implementing Philpot's algorithm and PCR on the image.

1. Select an area of the image which can be assumed to be deep water. Average some of these deepwater pixels.
2. Subtract the deepwater pixel from the rest of the image.
3. Take the natural log of this deepwater subtracted image (Philpot's \underline{X} matrix).
4. Calculate the covariance of the data. (\underline{X})
5. Determine the eigenvectors (\underline{A}). These are the coefficients, or weights. Most likely only the first three eigenvectors will be retained based on looking at a plot of the eigenvalues.
6. Calculate scores. $\underline{PC}_{\text{image}} = \underline{XA}$
7. Using the b s calculated from the above HydroMod Step 5, estimates for the dependent variables, depth, bottom type, and water type are found.
 $\underline{Y}_{\text{est}} = \underline{PC}_{\text{image}} \underline{b}_{\text{Hydro}}$
8. Compare the results with ground truth. For example, for depth, compare depth estimates with actual bathymetry.

Chapter 5

Results

5.1 Data Collection

Often, data collection for this research was at the mercy of the weather, functioning instruments, and boat availability. Although sometimes data collection was frustrating, it was also very rewarding because the location for data collection was Lake Ontario, usually on a boat on a beautiful, sunny day. The data needed for this research consisted of water samples, bottom type samples, and the images themselves.

5.1.1 Water Sampling

Water was collected under Landsat and MISI overpasses in order to characterize the water at the time the images were taken. The sample bottles were rinsed out twice with lake water prior to filling them up with water at each sampling location. The water sampling days and locations for 1999 and 2000 are shown in Table 5.1.

11 May 1999	Near Charlotte Pier, in Irondequoit Bay
20 May 1999	Near Charlotte Pier
07 Jun 1999	Ginna Power Plant
26 Jul 1999	Near Charlotte Pier
03 Sep 1999	Ginna Power Plant
05 Jul 2000	Near Charlotte Pier

Table 5.1 Water Sampling Dates and Locations – 1999 and 2000.

The water samples were filtered and processed as explained in section 3.4. The results of the processing of the 1999 samples will be located on the following website, <http://www.cis.rit.edu/research/dir.shtml>. Information on the September 3 1999 processing is located in Appendix D. The water parameters used for the HydroMod portion of this research are from the samples taken at Ginna on 3 September. Table 5.2 shows the sample number and the results of processing.

Sample	CHL-a (mg/m ³)	TSS (mg/L)	CDOM (scalar)
A2	1.868	1.000	0.467
A3	1.671	1.333	0.481
A5	1.145	1.333	0.485
A6	1.698	0.750	0.454
I1	0.934	1.000	0.451
I4	3.463	2.400	0.438

Table 5.2 Sampling Results for Ginna, September 3, 1999

Of note are the high chlorophyll and TSS values for the last sample, I4. These relatively high concentrations from sample I4 will manifest themselves in both the qualitative results from the algorithm processing and the radiance outputs from HydroMod.

These data were input into HydroMod in order to simulate as closely as possible the conditions under which the MISI images were taken. In order to be more accurate in simulating these conditions, bottom reflectances were also needed.

5.1.2 Bottom Sampling

The ASD was used to take reflectance spectra of various materials assumed to form the bottom boundary at the Ginna site near the power plant, based on visits to the area. This data collection requires a clear day in order to have consistent lighting conditions. To calculate the reflectance spectra, a Spectralon white reference is used to account for the lighting conditions.

The bottom at Ginna consists predominantly of rock and algae-covered rock. Therefore, a variety of rock spectra, and even spectra of algae-covered rock were collected. There is also some sand in the area, and so, this spectrum was included in the model. The following figures include images and spectra of the bottom types that were input into HydroMod to build the forward model.

Figure 5.1 is a graph of sand spectra: one is built into HydroMod, and the other was the spectrum of Ontario sand measured by the ASD. The bottom reflectance spectrum that is used for sand in these HydroMod runs is Ontario sand. The other sand

reflectance spectrum is inherent in the HydroMod program; however, it is for bright coral sand, and is not indicative of the sand found on the bottom of Lake Ontario.

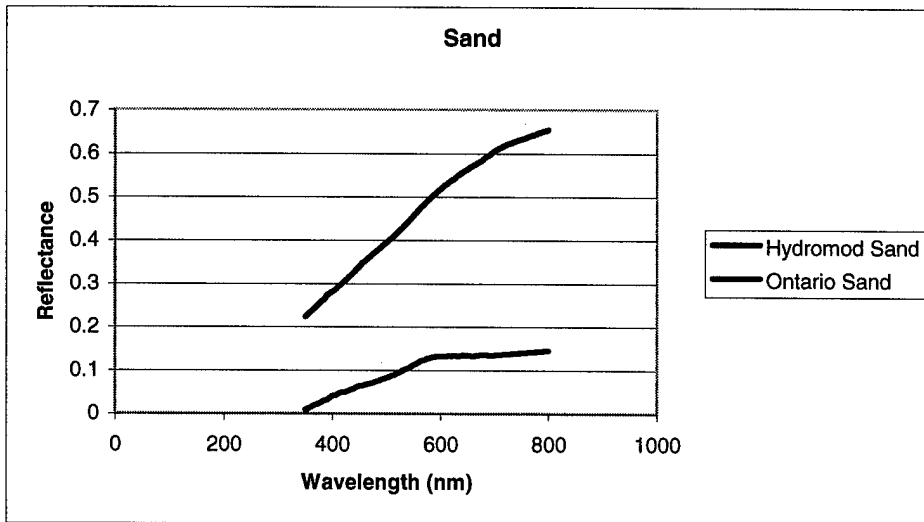


Figure 5.1 Hydromod Sand vs Ontario Sand – Reflectance Spectra

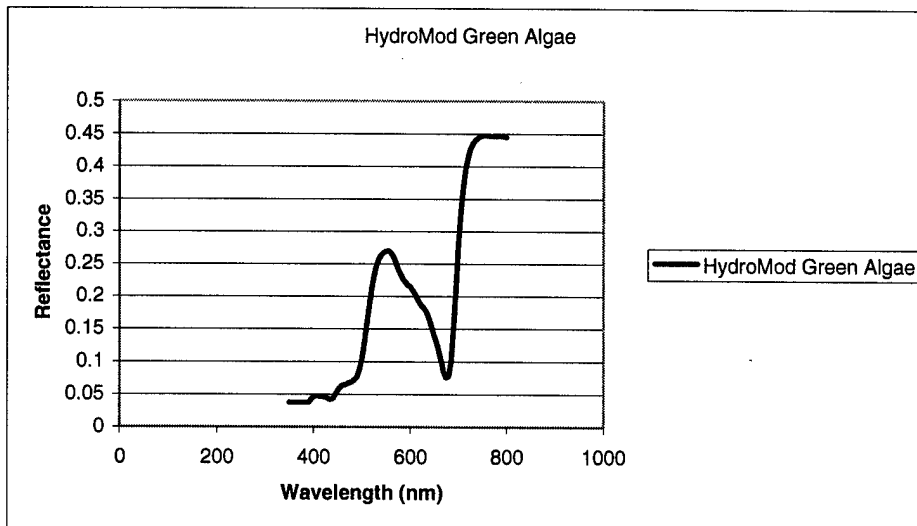


Figure 5.2 Green Algae Bottom Type in HydroMod

Figure 5.2 shows the green algae bottom that will form another bottom type used in the HydroMod runs. Actual reflectance spectra were collected of algae dredged from the bottom of the Lake near Charlotte Pier. The spectra had a similar shape as that of Figure 5.2; however, the magnitude was lower, due to the fact that the algae was dying. It was dark green and had a decaying odor. Therefore, the decision was made to use the HydroMod green algae spectrum because the bottom type that needs to be modeled is of live, benthic algae.

The following figures are images and spectra of various rocks and algae-covered rocks measured at Ginna on July 20, 2000. The various spectra will be inputs to HydroMod, representing different bottom types.

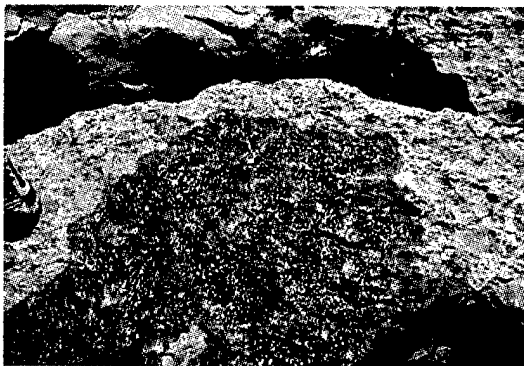


Figure 5.3 Gray rock wet (Groc1_wet)

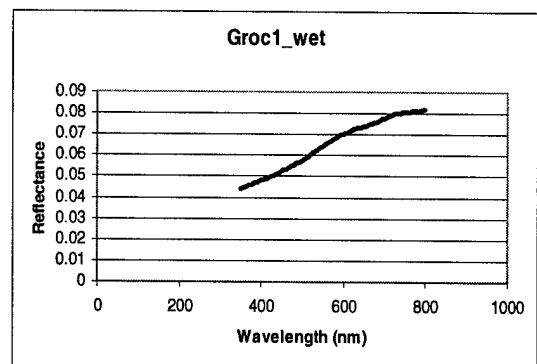


Figure 5.4 Groc1_wet input to HydroMod



Figure 5.5 Gray Rock 2 (Groc2)

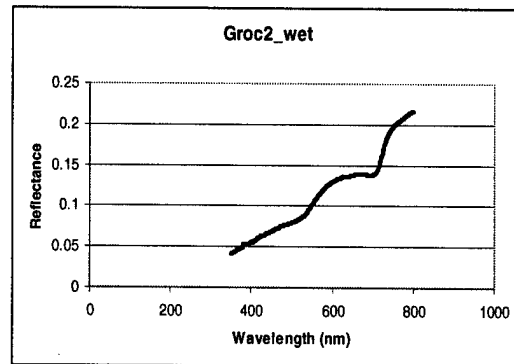


Figure 5.6 Groc2_wet input to Hydromod



Figure 5.7 Red rock (redrock_wet)

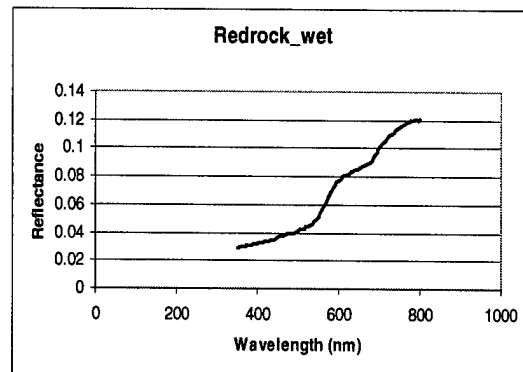


Figure 5.8 Redrock_wet input to HydroMod

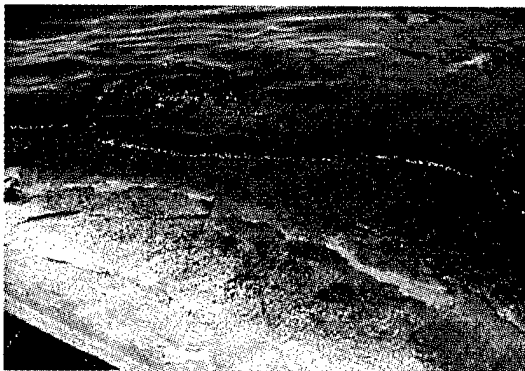


Figure 5.9 Algae on Red Rock (Rro_alg2)

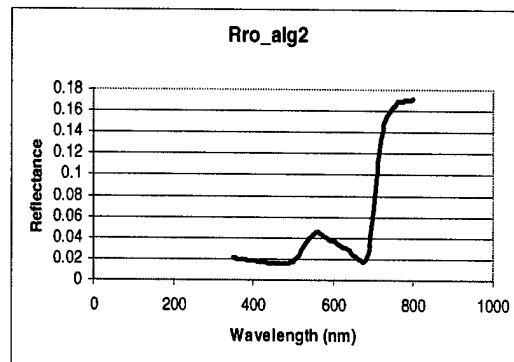
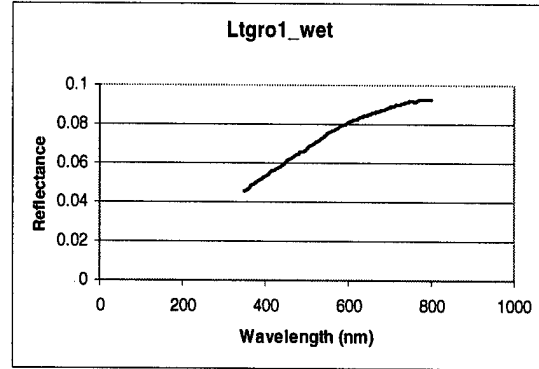


Figure 5.10 Rro_alg2 input to HydroMod



Figure 5.11 Light gray rock wet Figure (Ltgro1_wet)



5.12 Ltgro1_wet input to HydroMod



Figure 5.13 Yellow Rock wet (yroc1_we)

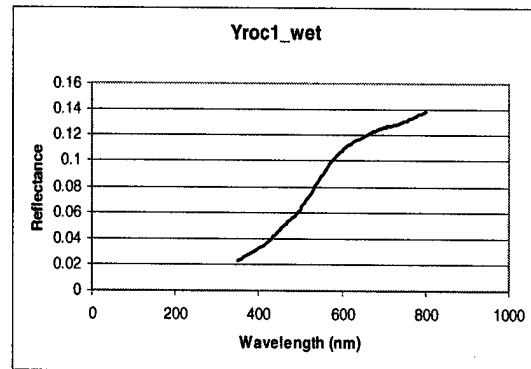


Figure 5.14 Yroc1_wet input for HydroMod

These bottom types are all characteristic of the Ginna area. The Ontario Beach area is characterized by the green algae spectrum and the Ontario sand spectrum. However, a visit to the coastal waters near Ontario Beach revealed that the algae is found growing on rock that is dark in color. The reflectance spectrum needs to be collected for the rock

found out near Ontario Beach in order to model accurately the parameters that form the MISI images of this area.

Bottom sampling was also conducted as part of ground truth collection. In order to sample the bottom, a Fieldmaster bottom dredger (Fig 5.15) was used. It is set open and dropped to the bottom. When it hits the bottom, it closes, scooping up whatever is there. At Ginna, it frequently hit rock, and therefore, nothing was pulled up.

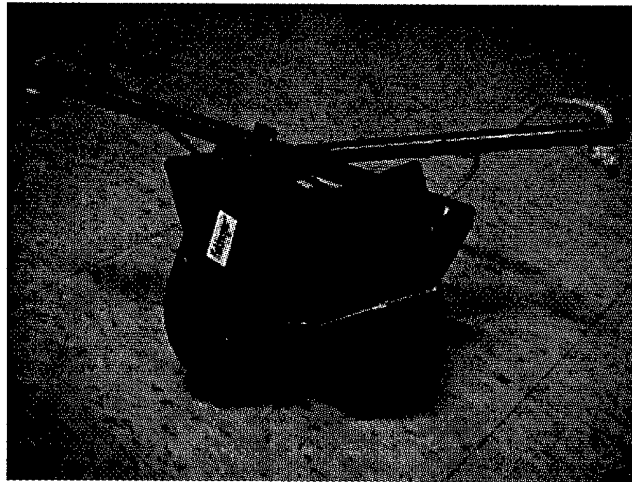


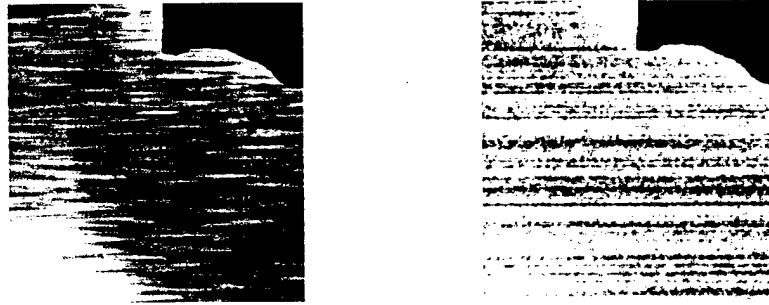
Figure 5.15 Bottom Dredger

This verifies, though, that the bottom consists of rock. The results of the ground truth are discussed in Section 5.5.5 for Ontario Beach.

5.2 MISI Images

The MISI images of the Charlotte Pier (Ontario Beach) and the Ginna Power plant were challenging to work with. Steps were taken to correct the significant noise problems observed in the MISI data. First, a low pass filter was convolved with the image, but upon analysis of each of the 63 bands, a significant amount of vertical banding and

horizontal streaking remained. Also, there were some bands that were unintelligible even after they were convolved with a low-pass filter (Fig. 4.16 and 4.17)



Figures 5.16 and 5.17 Band 12 and Band 20 Noise Problems in C9 (Ginna)

In addition to convolving the image with a low-pass filter, some of the worst bands were discarded prior to implementation of Philpot's algorithm. On the September 3, 1999 Ginna image (C9, Flight Line GFL2) that was taken perpendicular to shore, an area of the image was selected that began near the shore and went out perpendicular from shore. After some of the worst bands were discarded, 51 remained. The image used here to discuss the noise problems was 116 by 258 by 51 (Ginna_four) and is shown in Figure 4.18.

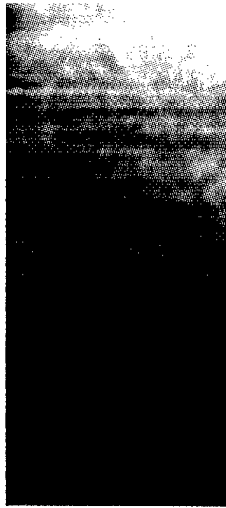


Figure 5.18 R,G,B Image near Ginna (Ginna_Four (Bands 24,14,5))

After initial noise processing, the principal components algorithm (Philpot 1989) was implemented on the image in an effort to determine water depth and bottom type information. $Y_{||}$ refers to the image obtained by multiplying the first eigenvector times the X matrix (linearized variable), and is assumed to provide information about depth; Y_{\perp} refers to that image obtained by multiplying the second eigenvector times the X matrix, and is assumed to provide information about bottom type. The principal components algorithm (Philpot 1989) was run on this image (Fig. 5.18) and then both the $Y_{||}$ image and the Y_{\perp} image were read into ENVI. A simple unsupervised k -means classification was performed to determine which image areas are similar. The k -means classification is performed on a single-band image, $Y_{||}$ or Y_{\perp} , and therefore is simply a gray-level map showing areas of similar brightness rather than a classification, which is typically done on

multi- or hyperspectral images. Figures 5.19-22 show the \underline{Y}_{II} images and their respective gray-level maps.



Figure 5.19 \underline{Y}_{II} on Ginna_four(Fig. 5.18)



Figure 5.20 \underline{Y}_{II} on Ginna_four classified



Figure 5.21 \underline{Y}_I on Ginna_four



Figure 5.22 \underline{Y}_I on Ginna_four classified

The greatest variation in the original image, highlighted by the algorithm and displayed in these images, appears fairly structured. It looked very much like the vertical banding seen in the NIR bands, two of which are shown in Figures 5.23 and 5.24.

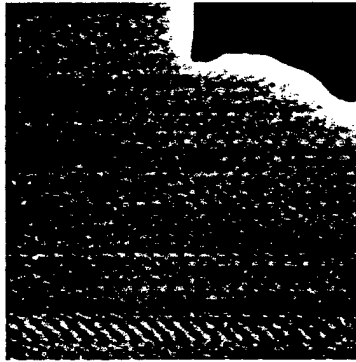


Figure 5.23 Image Band 48 from a 400 by 400 portion of C9

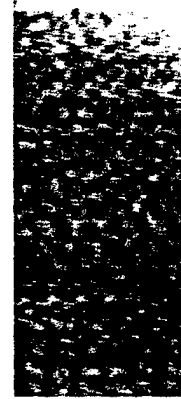


Figure 5.24 Ginna_Four Image Band 45

From these images, one can see that the vertical, wavy banding and the pattern that shows up in the algorithm-processed images are similar. The NIR bands don't penetrate very deep into the water, and therefore carry little information, with most of the signal due to noise.

Using ENVI, the image was spectrally resized again, deleting the NIR bands from the new image, 'Ginna_seven'(Fig. 5.25). The figures below show these results and from them one can see that the banding structure no longer is a significant part of the transformed images.



Figure 5.25 Y_{11} Ginna_seven



Figure 5.26 Y_{11} Ginna_seven classified



Figure 5.27 Y_{11} Ginna_seven



Figure 5.28 Y_{11} Ginna_seven classified

Additional steps were taken to improve the images prior to processing. First, median filtering was performed on the image, using a 5 x 5 median filter in ENVI. This helped alleviate some of the salt and pepper noise. Next, the image was convolved with a 5 x 5 low-pass filter to further blur some of the remaining noise effects. In an effort to increase the signal to noise of the image, the REBIN function in IDL was used to shrink the image spatially by averaging neighboring pixels, while still maintaining the spectral resolution,

although the spectral structure is degraded some due to the mixing of the adjacent pixels. Then, the same function restores the spatial dimensions of the image, using the default bilinear sampling on the expansion. After all of this processing, there were still bands that needed to be discarded, mostly in the NIR. A majority of the results discussed in this section were obtained by performing the principal components algorithm (Philpot 1989) on the September 3, 1999 Ginna image, C9 (Fig. 5.29). After pre-processing the image to reduce noise, only 24 bands were retained, shown in Table 5.3.

C9 MISI Band	From (nm)	To (nm)
1	413.2962	423.2962
2	424.0093	434.0093
3	433.4654	443.4654
4	443.4092	453.4092
5	453.3446	463.3446
7	472.5747	482.5747
8	482.7745	492.7745
9	492.398	502.398
13	531.0634	541.0634
14	541.0261	551.0261
15	550.9241	560.9241
17	569.9559	579.9559
18	579.4766	589.4766
19	589.0528	599.0528
21	608.0472	618.0472
22	617.5073	627.5073
23	626.9557	636.9557
24	636.0559	646.0559
26	654.5307	664.5307
27	663.8746	673.8746
28	672.8923	682.8923
29	681.5585	691.5585
31	699.4486	709.4486
32	708.0663	718.0663

Table 5.3 Ginna (C9) MISI Bands retained for algorithm

5.3 Image Selection

Philpot's algorithm (1989) was implemented on an image called C9 after noise processing. The image is shown in Figure 5.29.

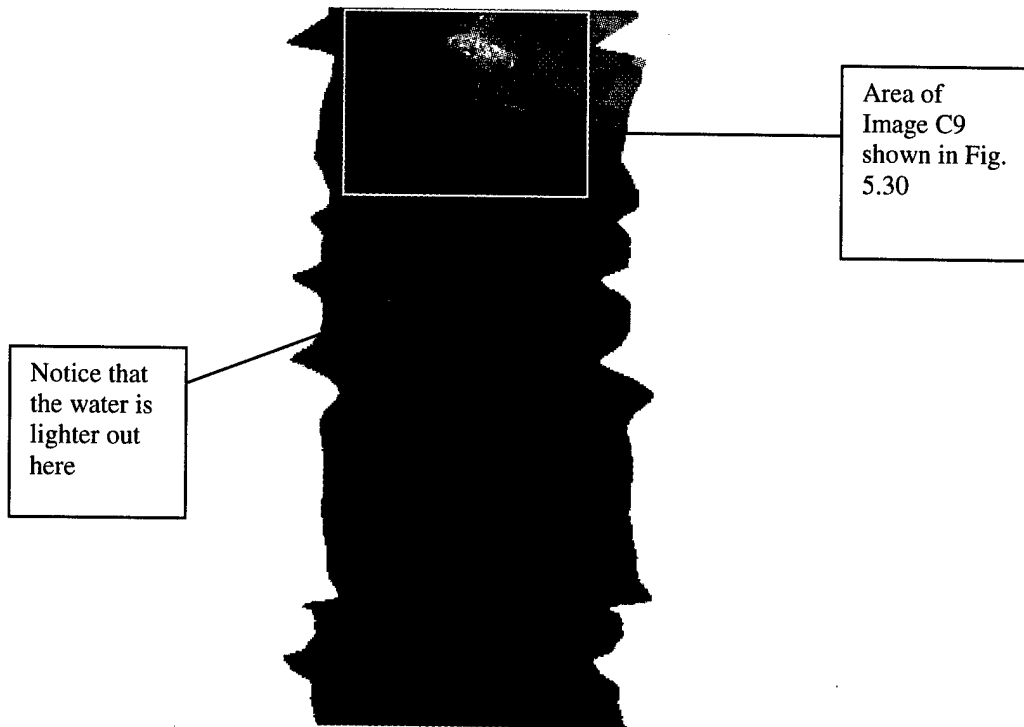


Figure 5.29 C9 – R,G,B, Image of Ginna

Philpot's algorithm (1989) depends on a deep-water subtraction. Many of the images taken during flight lines parallel to shore do not contain deep-water pixels. A benefit of using this image is that deepwater pixels taken at the same angle as the image can be selected. A second benefit of using this image is that the Ginna area has a lot of variation in it. Figure 5.30, a smaller piece of C9, shows the variation in bottom type near the shore, which the algorithm will extract.

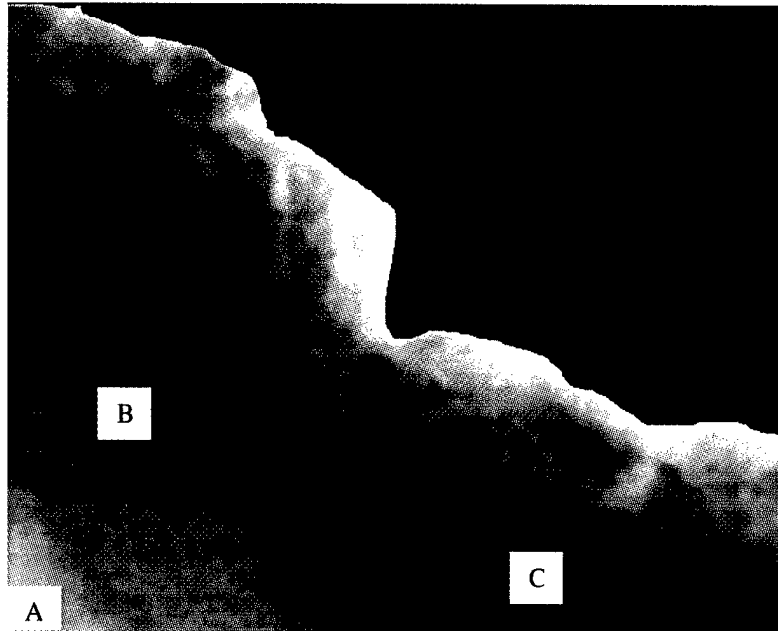


Figure 5.30 Smaller portion of Image C9 showing coastal bottom type variation

An aspect of this image, which will be discussed later in this Chapter, is the bright blue area of water at the left side of Figure 4.30. This image characteristic provided a challenge in implementing Philpot's (1989) algorithm on Case 3 data, where the water type varies, and in this image, the water type variation is apparent from the image. The very bright blue corner, A, is most likely due to a phytoplankton bloom that was occurring at the time this image was taken and was noted during water sampling on September 3 (corresponding to sample I4 discussed in Table 5.2). The slightly darker water, B, is most likely due to a combination of different water type and lighting conditions and C is an area where the water type appears darker than both A and B. The

image was taken at 11:19 EST, which means that the sun was more towards the left side of the image (east), resulting in a variation in lighting conditions.

Although most of the results were calculated from the September 3, 1999 image of Ginna, one of the MISI images taken on July 5, 2000 near the Charlotte Pier, C2 (Flight Line RFL1), was also processed (Fig. 5.31). These images were taken parallel to the shore, and therefore were not ideal, because there is not much deep water. The deep-water pixels are selected from an area of the image that was not at the same angle relative to nadir as that area being processed by the algorithm. However, one of the goals of this research is to see how well the algorithm performs on images taken of this portion of Lake Ontario, since it experiences many problems due to algae washing up on the shore. The images from this day have some missing lines, so a smaller area of image C2 (Fig. 5.31) was selected that did not have missing lines and contained land references easily recognizable from the water for ground truth purposes.

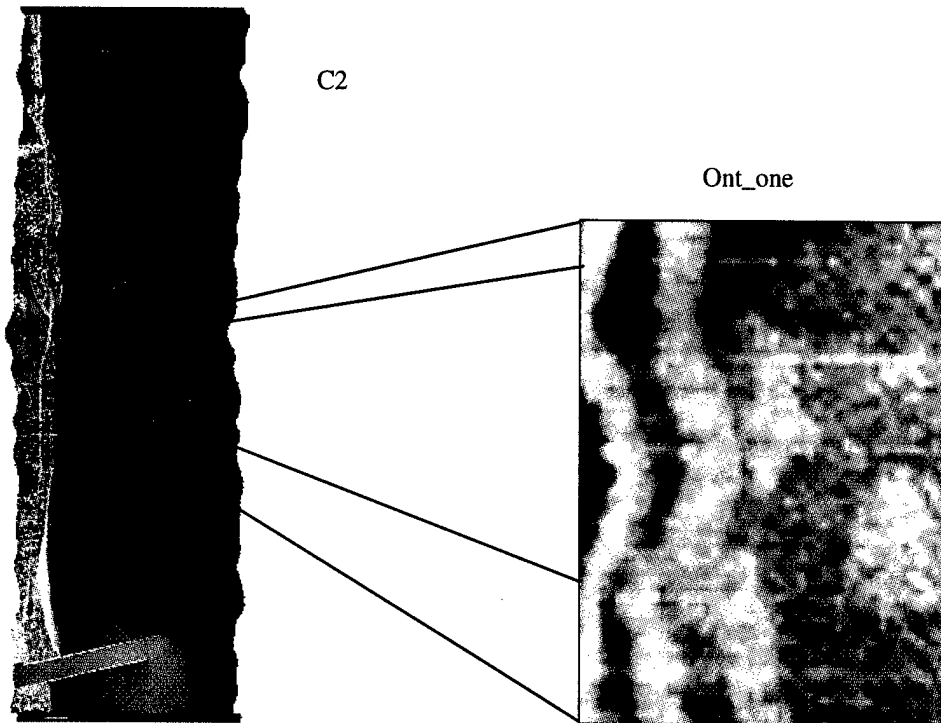


Figure 5.31 C2 – along Ontario Beach and a spatially resized portion of C2, Ont_one

5.4 Qualitative Results

After applying Philpot's (1989) algorithm to various small pieces of the C9 image, the next step was to look at bigger areas of the image. In order to do this, the algorithm must be able to perform the eigenvector analysis on just the water pixels, because applying the algorithm to the entire image, including the land, decreases the likelihood that the variability of interest is in the first two eigenvalues, if any of them. The image, C9, was resized both spatially and spectrally in ENVI to produce an image that contains the shallow water and eliminates the noisy bands, resulting in a 24-band image, the bands shown earlier in Table 5.3. The depth and bottom type maps are a result of k-means

unsupervised classifications, which essentially are just the gray-level maps discussed earlier, on the $Y_{||}$ and Y_{\perp} images, for which areas that are similar in brightness are grouped in the same class.

5.4.1 Using the Entire Width for Deep-Water

Usually, deep-water pixels are selected such that they cover the same columns as the image. However, in C9, there was an obvious difference in water type further out in the image, which might affect the results. Figure 5.32 is the image, called Ginna for discussion purposes, and the corresponding deep water taken over the entire width of the original image, C9 (Fig 5.29).

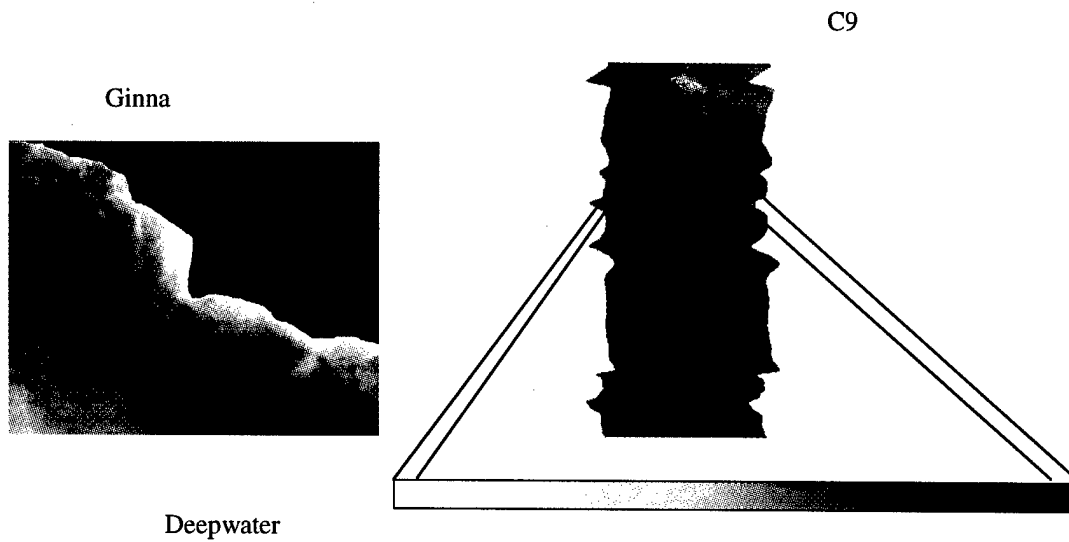


Figure 5.32 Image Ginna and the deepwater taken over the entire width of the image

Of note is how light the pixels are on the left side of the deepwater image. The deep-water pixels were averaged and the resulting vector was subtracted from each of the pixels in the Ginna image. The next step in this deep-water correction technique is to calculate the natural log of the resulting matrix. The final result of this deep-water correction is the linearized variable, \underline{X} . Plotting the \underline{X} values for the 640 nm vs 545 nm band should show that there is a somewhat linear relationship between the two linearized variables, \underline{X}_{640} and \underline{X}_{545} , provided the water type is constant. Figure 5.34 is a scatter plot of these two bands in linearized space for the colored section of the image in Figure 5.33. Next, the principal components analysis was performed on the linearized data. The first principal component points in the direction of maximum variance in the data set, showing that a linear combination of the variables \underline{X}_{640} and \underline{X}_{545} using the optimal coefficients (first eigenvector) indicates the information that is correlated between the two bands.



Figure 5.33 Y for Ginna image processed using the entire width of C9 for deep water (colored portion corresponds to 5.34)

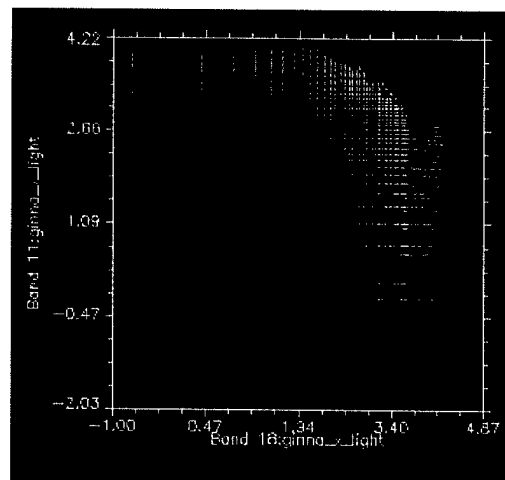


Figure 5.34 Scatter plot of \underline{X}_{640} (Band 24) vs. \underline{X}_{545} (Band 15) using the entire width of C9

This plot is not linear, which is an indication that an assumption has been violated. The scatter plot should be linear if the water type is constant, which is not true of this example. The deepwater term, L_w , used in the principal components algorithm (1989) is also presumed constant, but when this is not a valid assumption, the usual linearization is no longer suitable, and attempting to use it results in the nonlinearities seen in the scatter plot (Fig. 5.34).

Further analysis of the scatter plot and its corresponding regions in the image reveal other inconsistencies. The red and green regions of the image (Fig 5.33), which, based on their position in the scatter plot, should correspond to the shallow areas of the image, seem reasonable, but the next region (yellow) based on the scatter plot should be getting shallower because the yellow points start to spread towards the top of the plot, also shows up near the left side of the image. Intuition and bathymetry confirm that this trend of getting deeper as one moves away from shore and then shallower again further out is due to error in the assumptions made. The blue area in the image corresponds to pixels in the scatter plot that are in a very shallow area due to their location near the top of the plot. However, considering the location of the blue region in the image, this does not make sense, and results from a combination of the different water types, i.e. water with different optical properties, in the image being processed by the principal components algorithm and from using the entire width of the image, which contains different water types, for the deep water. The deep-water correction of the algorithm

subtracts off the averaged deep-water pixels and therefore does not take into account the fact that the image being processed contains different deep and shallow water types. The next figures show the depth map and bottom type map resulting from using the entire width for deep water.

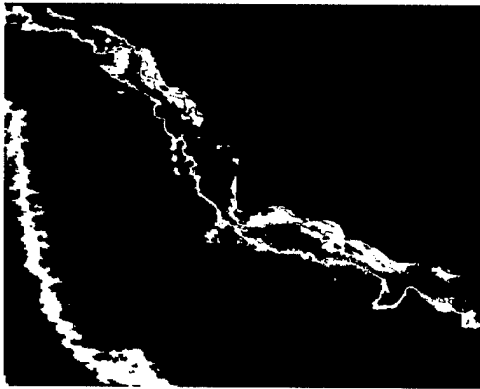


Figure 5.35 $Y_{||}$ - deepwater of entire image (~Depth)

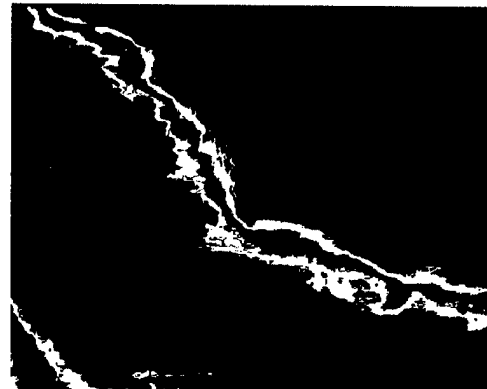


Figure 5.36 Y_{\perp} - deepwater of entire image (~Bottom type)

These maps do not seem reasonable, as might be expected based on analysis of the scatter plot in Fig 5.34. In Figure 5.35, the depth map, the water gets deep and then shallow again as one moves away from shore. There is deeper water (yellow) near the shore. From water truth observations, the trends in the depth map are not true. Figure 5.36 is not picking up on the bottom type variation that is visible from the image itself. It is also very similar to Figure 5.35 in appearance, which was not expected because it is a bottom type map.

Next, the technique was repeated, choosing a different area for deep-water pixels.

5.4.2 Using Darker Deep-Water

The algorithm was performed on the same shallow water image, Ginna, but the deep-water pixels were selected from the right side of the image C9 as shown in Fig 5.37.

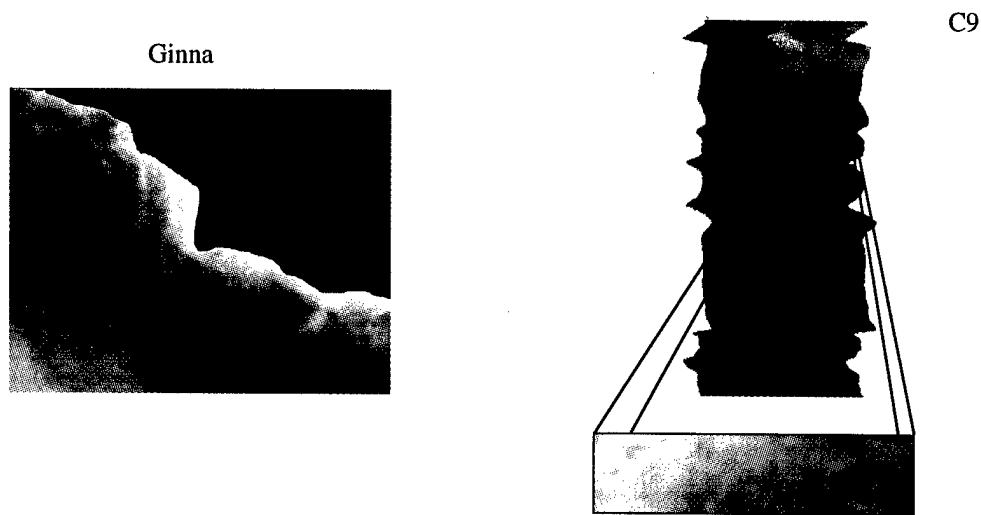


Figure 5.37 Ginna image and deepwater from the right side of the image, C9

The deepwater image in Figure 5.37 is noticeably darker than that shown in 5.32, which used the entire width of the image. The left side of the deepwater image is still brighter than the right side due to stretching in ENVI. Once again, the average of the deep-water pixels was calculated and the algorithm applied, as above, resulting in improved depth and bottom type maps. Figure 5.39 is the scatter plot of the linearized variables, X_{640} vs X_{545} , and it is closer to the expected linear plot that should result when the water type is constant.

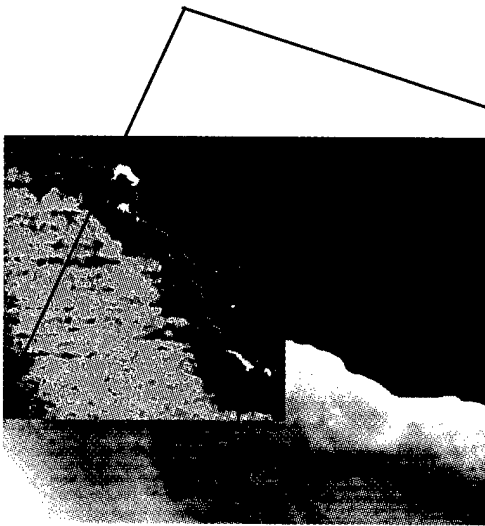


Figure 5.38 Y_{11} for Ginna processed with deep water from right (colored portion corresponds to Fig. 5.39)

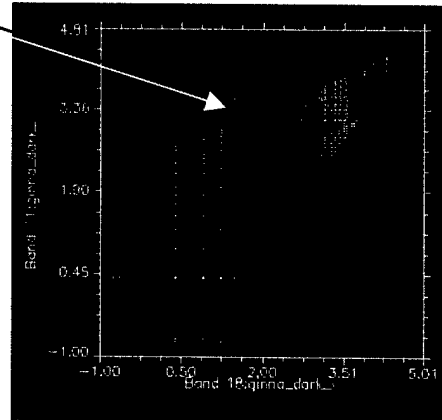


Figure 5.39 Scatter plot of X_{640} (Band 24) vs. X_{545} (Band 15) using the right side of C9 for deepwater

The colors of the scatter plot represent the data that correspond to the regions of the image in Figure 5.38. The linearization performed better at smaller depths, but where the scatter plot spreads out at greater depths, the results depart from intuition. The dark green class at the left side of the image corresponds to the portion of the scatter plot pointed to by the arrow. If our assumptions are correct, this dark green area is more shallow than the sea-green region of the image. However, the dark green region is located at the very left of the image, where the water should be the deepest. This inconsistency is probably a result of the dark deepwater being subtracted from an area of different water type, and the greatest variation is no longer related to depth, but is now associated with a change in water type. The shallow areas of the image correctly correspond to the right side of the scatter plot, although caution is required in

interpretation because this may be an area where water type varies with depth. The uncertainty of the depth estimate increases greatly with depth, as can be seen in Figure 5.39, indicated by the spreading out of the graph as the depth increases.

Figure 5.40 is a plot of the eigenvalues for this image. The first eigenvalue, the amount of variability assumed to be due to depth, accounts for 41% of the variability. The second eigenvalue, variability assumed to be related to bottom type, accounts for 21% of the variability in the data.

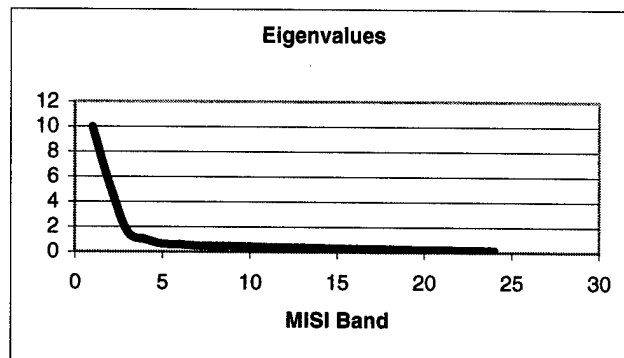


Figure 5.40 Eigenvalues from PCA on Ginna image processed using deep water from the right side of C9

The first three bands carry most of the variability in the data. In this example, the variability accounted for in the first eigenvector does not totally correspond to depth variation but also includes some variation due to change in water type. Similarly, the second eigenvector is mixed because as soon as the first eigenvalue is mixed, the remaining eigenvalues must also be mixed due to their perpendicular nature.

The depth map and bottom type map determined using the deep-water from the right side of the C9 image seem more reasonable than the previous example (Fig. 5.32).

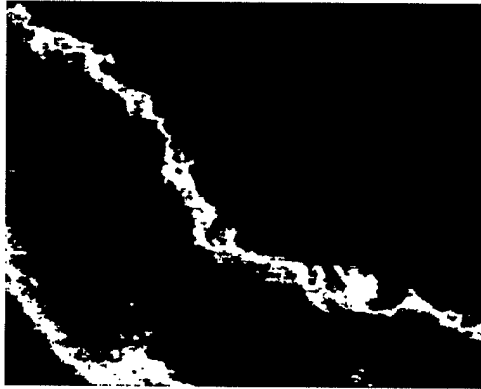


Figure 5.41 Y using deep water from right (~Depth)



Figure 5.42 Yperp using deep water from right (~Bottom Type)

Figure 5.41 is more intuitive than the depth image calculated when the entire width of the image was used for deep-water. The first four classes (cyan, yellow, blue, and then green in order of decreasing brightness) show that the water gets consistently deeper as one moves out from the shore, as one would expect. But, the results show again that the water gets deeper and then shallow, so that the area one would expect to be deepest (the bottom left corner of Fig 5.41) is actually shown to have a similar score, i.e. is as shallow as, the water right off the coast (cyan class). The algorithm is equating the brightness in the lower left corner of the Ginna image presumably caused by different water type to shallow water. Figure 5.42 is a great improvement over the bottom map from the results processed using the entire width of the image for deep-water (Fig. 5.36). Fig. 5.43 points out where the bottom map seems to be discerning bottom-type variations that are visible in the image.

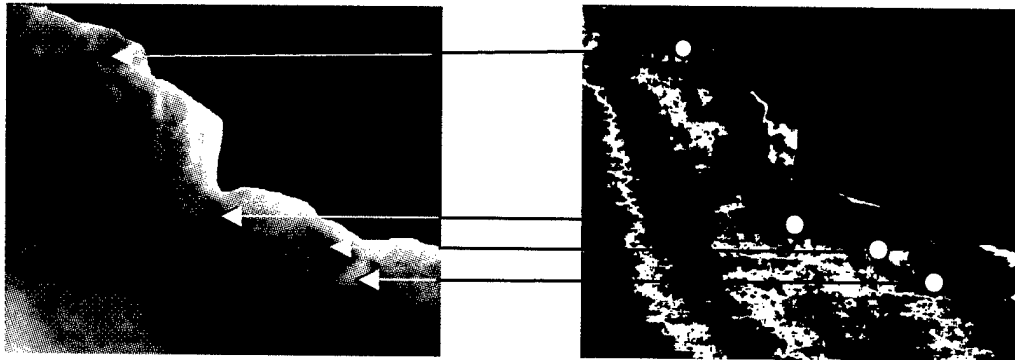


Figure 5.43 Y_{\perp} (~Bottom type) is picking up on variations in Ginna image

The cyan class on the left side of the Y_{\perp} image is still problematic. This is due to the deep water not being consistent with the water qualities in the rest of the image. It can be inferred that the bottom type mapping, like depth mapping, performs better at smaller depths, which is most likely because there is less effect due to water-type variation in shallow water.

The qualitative effects of variable water type in the deepwater pixels are significant. Further processing was done on smaller portions of the image where there appeared to be constant water type.

5.4.3 Consistent Deep Water

Figure 5.44 shows the image selected from the right side of the image (Ginna_right) and its respective deep-water image that was used to perform the algorithm.

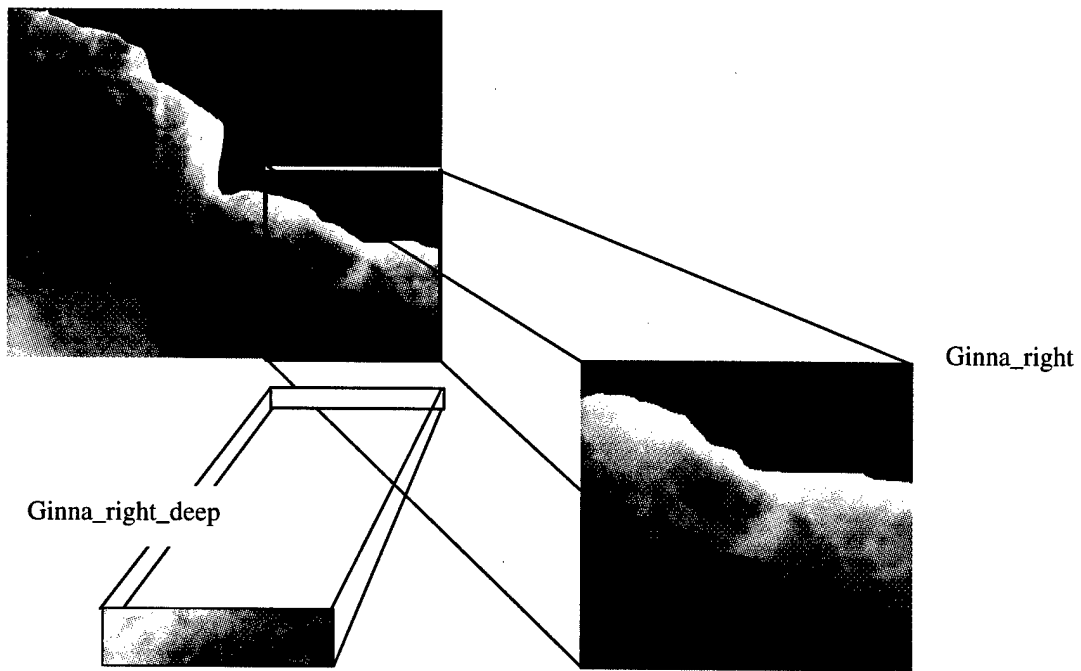


Figure 5.44 Image and Deep_water from the Right Side of Ginna



Figure 5.45 Ginna_right with colors corresponding to 4.45

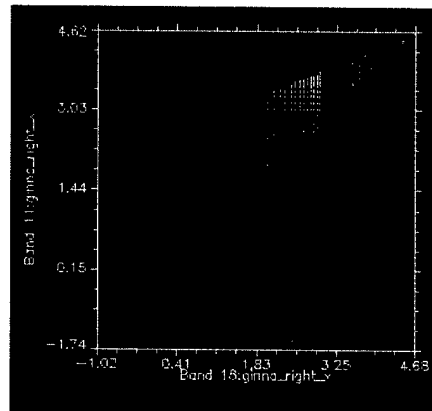


Figure 5.46 Scatter plot of X_{545} (Band 15) vs. X_{640} (Band 24) for Ginna_right

The results from processing with these images are very encouraging. Fig. 5.46 exhibits much more linear behavior, indicating that the information in these bands is more closely correlated in the linearized space and that there are fewer unmodeled factors.

Statistically, the information was pretty highly correlated before, but this does not always mean that the correlation provides the information desired. The trend in Fig. 5.47 is very intuitive, the water gets deeper as one moves away from the shore. Below are the depth and bottom type maps.



Figure 5.47 $Y_{11}(\sim\text{depth})$ – k -means classification of Ginna_right using 3 classes and 4 classes, respectively

These results are very reasonable; the water gets consistently deeper as one moves out from the shore. Looking at 2 m resolution bathymetry from this area confirms this trend.

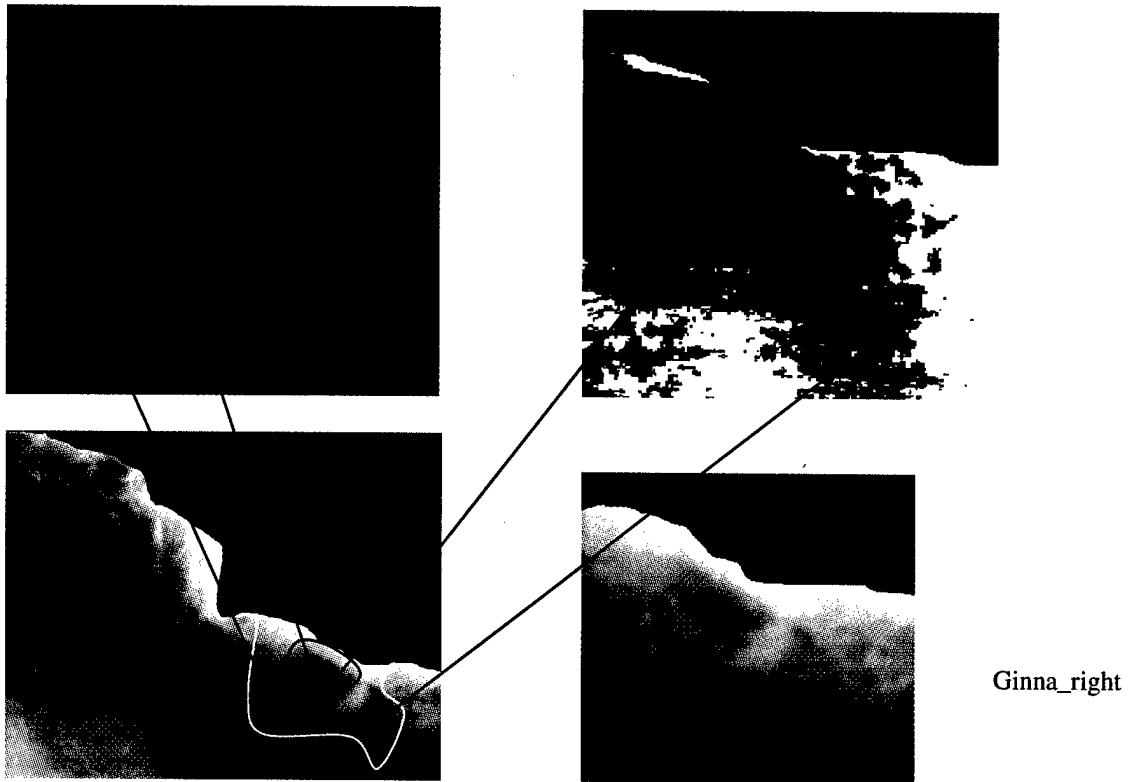


Figure 5.48 Y_{\perp} (~bottom type) using 3 and 4 classes, respectively and comparison to actual image. Arrows indicate where bottom type variation seen in the image shows up in the bottom type maps

This bottom map is reasonable, however it appears that using three different gray-level brightnesses is sufficient for distinguishing the different bottom types. The bottom type map highlights some of the major variations that can be seen in the image, and there are problems with the varying water types seem to be eliminated.

The algorithm performs better when the deep water is the same, or nearly the same, water type as the image being processed as in this example. The results do not

contain the non-linearities evident in the example discussed in Section 5.4.1, which used the entire width of the image as the deep water. The depth map and bottom type map agree with intuition and analysis of the image.

In summary, to obtain good results, one must select an area in which the water type is constant over the image and the deep water, there are depth variations, and bottom variations. This is a limitation of the principal components analysis approach in that it depends on the image selection.

5.4.4 More Results

Attempts were made to select other areas in the image where the water type was thought to be constant, although the efforts were not as successful as that in Sec. 5.4.3.

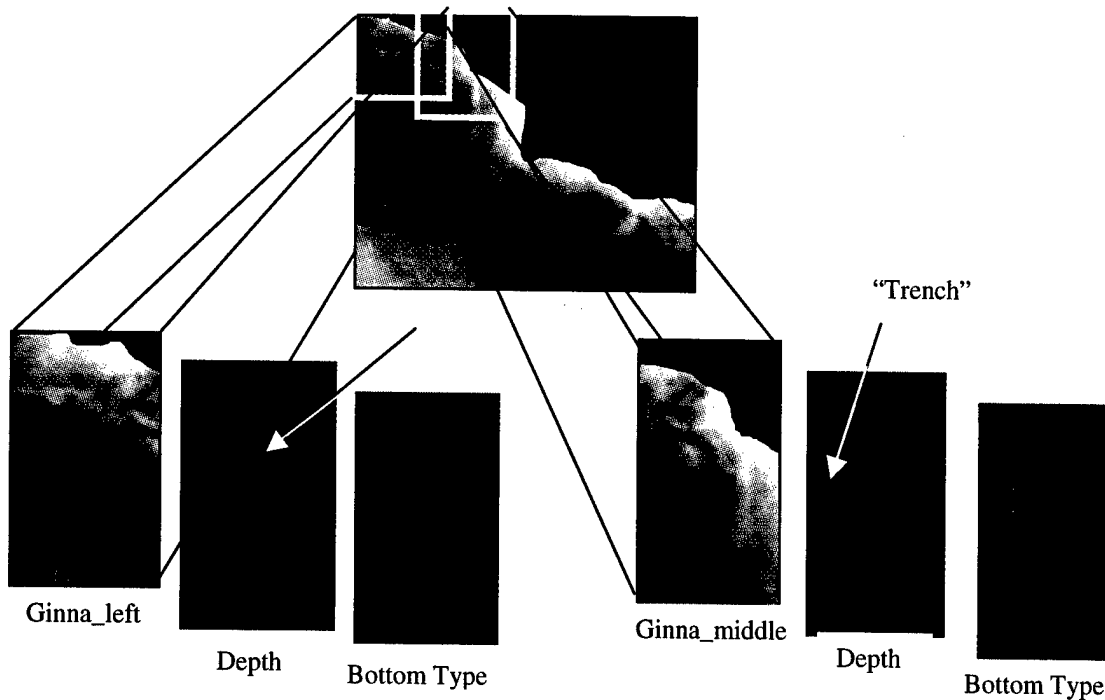


Figure 5.49 Ginna_left with its corresponding depth and bottom type maps

Figure 5.50 Ginna_middle with its corresponding depth and bottom type maps

An interesting feature of the depth maps of both images is a narrow region (red) that indicates some sort of trench, or area of deeper water. The “trench” corresponds to the line where the water becomes deep very quickly as indicated by the drop-off in the ability to see the bottom variation in the image. The “trench” shows up in both depth maps, which were produced using eigenvectors from different principal component analyses. The bottom maps again are highlighting variations in bottom type that can be seen in the images themselves.

The algorithm performs better on smaller sections of the image because there are typically not as many variations, such as water type, over a small area. The variations that will most likely be present in an image that covers a greater spatial region are not limited to varying water type, but might include atmospheric conditions, illumination, and sea state.

5.4.5 Ontario Beach Results

In order to determine the feasibility of mapping the distribution of benthic algae in the Ontario Beach area to benefit the County Health Lab, a preliminary analysis was done on a MISI image taken of the area July 5, 2000. The image selected for this analysis was C2 (Fig. 5.51). This image was selected because it was taken at a higher altitude than some of the other images; this is significant because more water is included in the image, which is important in deep-water selection. Also, it was one of the better-quality images in terms of noise, missing lines, and sun glint through the middle of the

image. The flight line for this image was parallel to shore, and therefore, it is almost certain that the deepwater pixels are not at the same angle relative to nadir as the part of the image being processed. This effect was not corrected for in this analysis.

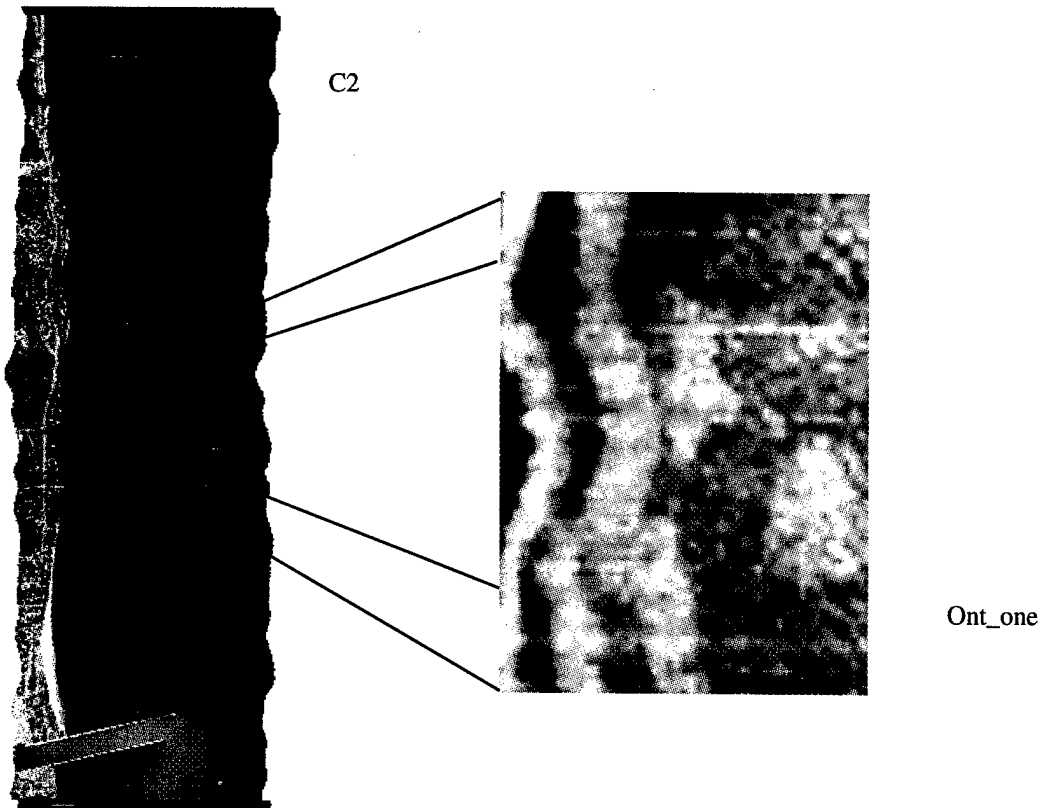


Figure 5.51 Image near Ontario Beach, C2, and the Image area selected for processing, Ont_one

Although this was one of the better images from the July 5, 2000 MISI collect, the sun glint can be seen down the middle of the image C2, and is present on the right side of Ont_one. Below (Fig. 5.52 - 5.55) are the results of applying the algorithm to this image. The deepwater was selected from the extreme right of the image (C2) because there is not

a significant amount of water that appears to be deep enough to not be influenced by the bottom type.



Figure 5.52 Y for Ont_one



Figure 5.53 Y classified for Ont_one



Figure 5.54 Y_{\perp} for Ont_one



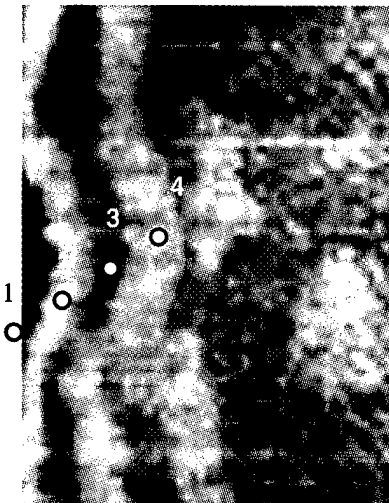
Figure 5.55 Y_{\perp} classified for Ont_one

The depths and bottom types are correlated in this image. Analysis of Figs. 5.52 and 5.53 indicates that there are ridges on the lake floor and the depth alternates between shallow and deep with these ridges. The bright area (green in Fig 5.53) on the right of 5.52 is due

to the sun glint effect and is not related to depth. The shallow areas (green) correspond to the light areas in Fig. 5.54, which are of sand bottom type, based on ground truth. The deeper areas (red) correspond to the dark areas in Fig. 5.54, which indicate rock bottom type. The change in depth has been verified by ground truth.

These preliminary results are very promising for the application of this algorithm to MISI images in order to determine the location of benthic algae. The algae attach themselves to hard surfaces, i.e. rock. At one sampling location, a small amount of algae was grabbed from the rock bottom with the dredger.

The depth changes and bottom type changes in Figs. 5.53 and 5.55 were verified by ground truth. Fig. 5.56 shows the sampling locations and data for this image, which was collected on July 30, 2000.



	Bottom Type	Depth (m)
1	Rock	2
2	Sand	1.6
3	Rock	2.4
4	Sand	2.2

Figure 5.56 Ground Truth Results for Ont_one

5.5 Building the Forward Model

The HydroMod model was run for September 3, 1999 atmosphere and water conditions. The water types that were input were based on the water sampling campaign and subsequent processing of the samples. The results for sampling are in Appendix D. The output for each of the HydroMod runs was water-leaving radiance. For the purposes of comparison to the algorithm output, the sensor-reaching radiance was needed. To get the radiance to the sensor, it was necessary to multiply by the transmission and then add upwelled radiance for the September 3, 1999 atmosphere. Figure 5.57 shows the upwelled radiance and transmission information for September 3, 1999 conditions sampled at MISI wavelengths. These values were obtained using MODTRAN.

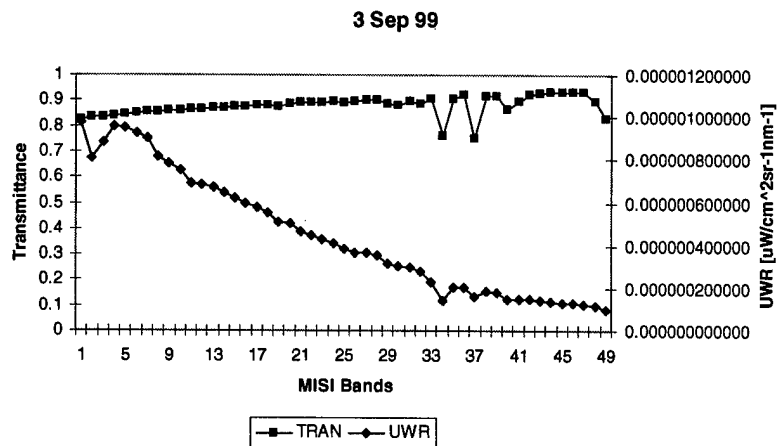


Figure 5.57 Transmission and Upwelled Radiance for September 3, 1999

One run was performed, with the bottom reflectance set to zero at every band in order to determine the radiance due to the water column itself. Fig. 5.58 is a plot for the various water types at various depths over the zero reflectance bottom.

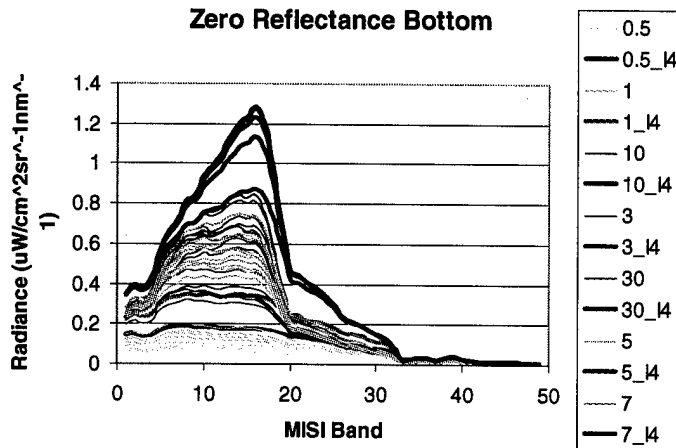


Figure 5.58 Plot of Sensor-Reaching Radiances for a Zero-Reflectance Bottom

The spectra with the greatest radiance in the plot are from the water sample I4, which contained the highest values of chlorophyll-a and TSS. The characteristics of the spectra for the sample I4 agree with the physics of the situation, a high TSS concentration increases the radiance, and the high CDOM value for this sample decreases the radiance at wavelengths < 600 nm.

The next figures, 5.59, 5.60, and 5.61, plot the sensor-reaching radiances for various water types and bottom types at 0.5 m, 1 m, and 30 m respectively. In Figs. 5.59 and 5.60, the plots for each water type are grouped by color, based on bottom type, for legibility purposes. The 30 m plot does not show which bottom type the spectra represent

because at 30 m, the water is deep enough that the bottom has no influence on the radiance. These spectra were used as the deep water data in the application of the algorithm to the HydroMod output.

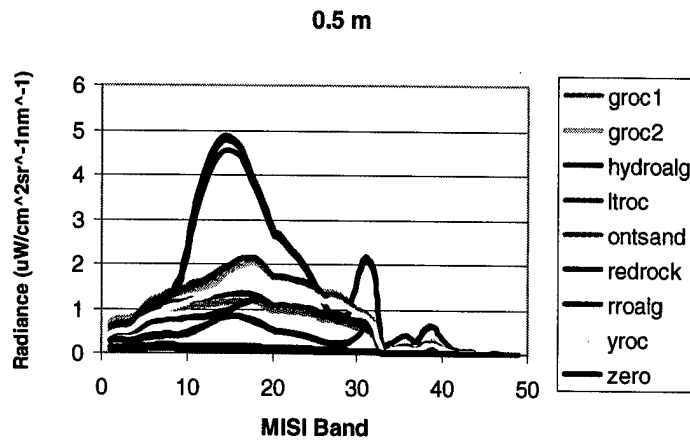


Figure 5.59 Sensor-Reaching Radiances at Depth of 0.5 m

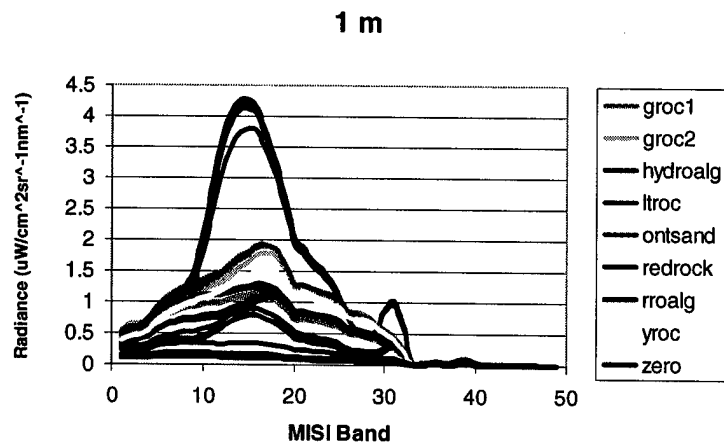


Figure 5.60 Sensor-Reaching Radiances at Depth of 1 m

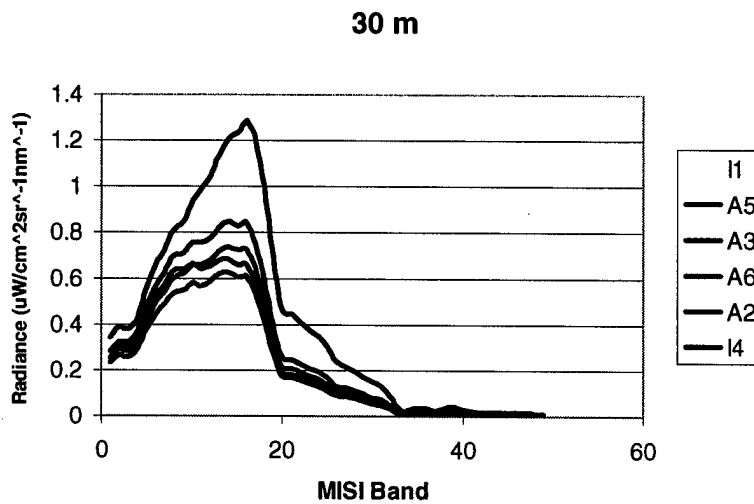


Figure 5.61 Sensor-Reaching Radiances at Depth of 30 m

Aside from the radiances calculated for the HydroMod green algae bottom, the other radiance spectra are similar in shape. At one point, an area of the C9 Ginna image was selected, that was known to contain red rocks on the bottom, and a z-profile (where z = wavelength) of the radiance spectra at each wavelength was collected using ENVI. Then, a crude procedure was implemented to try to match the shape of the z-profile to the shape of the radiance spectra output from the HydroMod runs. The z-profile matched to one of the Ontario sand spectra by minimizing the RMS error between the z-profile and the HydroMod radiance spectra. Several other areas in the image known contain some type of rock bottom matched to Ontario sand spectra as well. This seems to be because there is not a significant difference in the output spectra from HydroMod, especially in the 24 bands that were retained from the MISI image.

5.6 PCR

The principal components regression was attempted on the HydroMod outputs. The deep-water correction was performed by subtracting the 30 m spectra generated by HydroMod from the spectra generated for the other depths, and then taking the natural log of the result. The principal components analysis was then performed on the linearized data. Fig. 5.62 is the plot of the eigenvalues from the PCA.

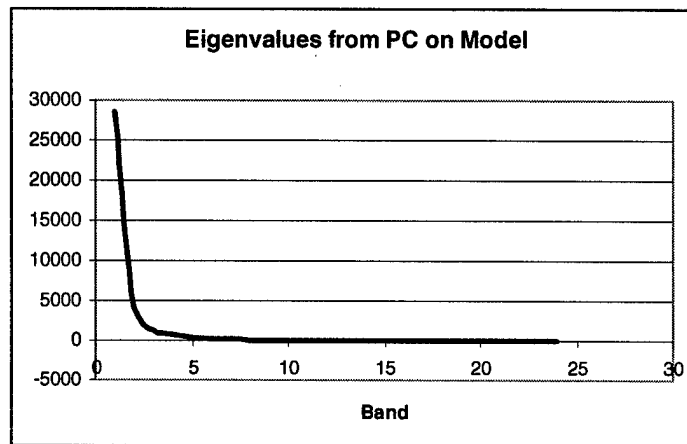


Figure 5.62 Eigenvalues from the PCA on Model Data

The first principal component accounts for 80.5% of the variability in the data, the second for 11.3 %, and the third for 3.5%. Depth accounts for 80% of the variability in the data. Next, the first three principal components were regressed against the inputs, depth, bottom type, and water type in order to obtain regression coefficients. The regression failed with regard to bottom type and water type because the inputs, numbers representing the bottom type or water type, had no physical meaning and regression does not work on categorical data. The regression predicted the depth with an RMS error of

0.82 m which is not very accurate because it is greater than one of the depths the regression is attempting to predict. The depth does not account for 100% of the variation in the data. The effects of depth, bottom type, and water type cannot be completely separated and still have some influence on one another even after principal components analysis.

The images of Ginna discussed in previous sections were transformed into Y and Y_{\perp} using the algorithm and then the depth regression coefficients determined from the HydroMod model data were applied to see what depths would be predicted (Figs. 5.63-5.65). Then, these values were compared to actual ground truth.

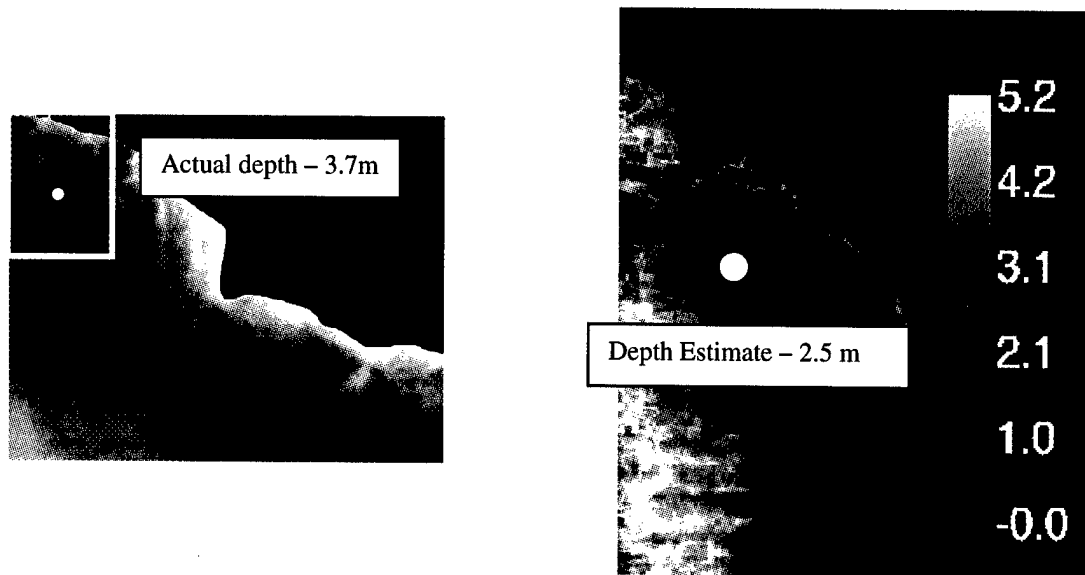


Figure 5.63 Quantitative Depth Results for Ginna_left

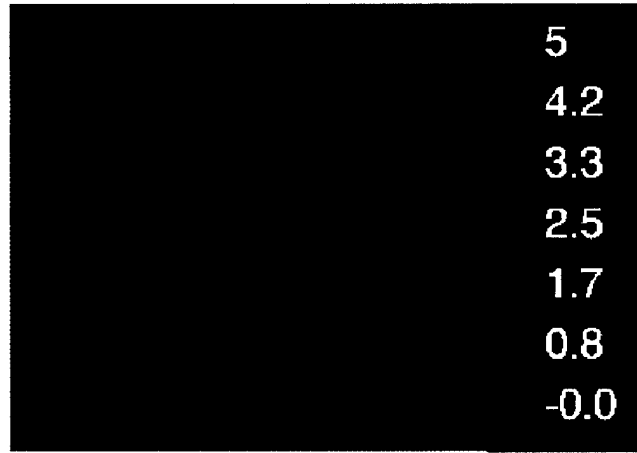
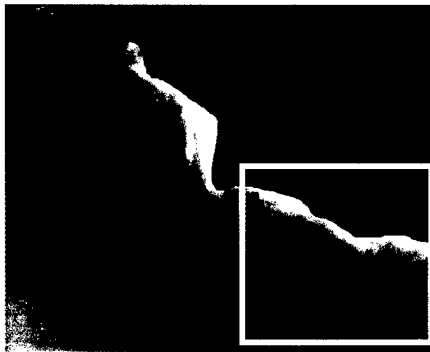


Figure 5.64 Quantitative Depth Results for Ginna_right

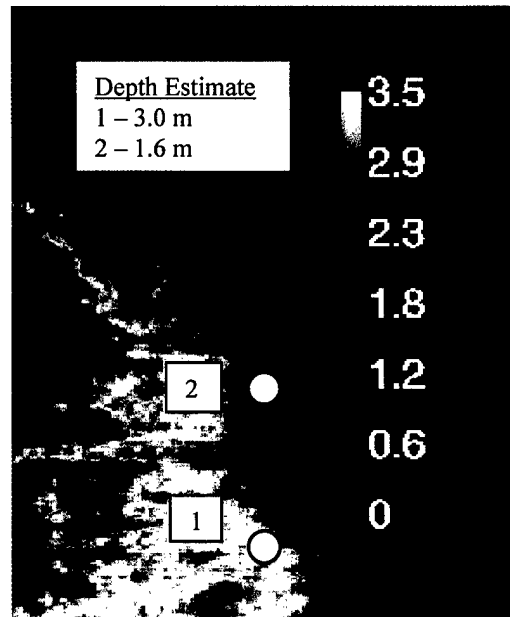
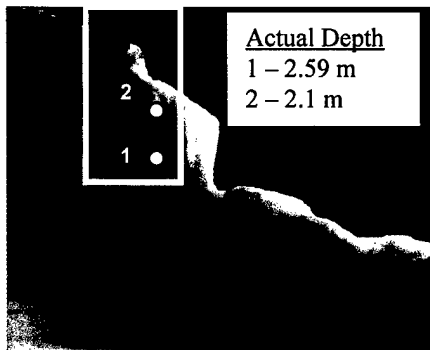


Figure 5.65 Quantitative Depth Results for Ginna_middle

Some fairly reasonable estimates were made of depth. However, there are some limitations to using the PCR for this application which will be discussed in the following chapter.

Chapter 6

Conclusion

Recently, increased attention has been given to studying shallow water to include the effects of bottom reflectance. Great potential exists for determining qualitative water depths and bottom type maps in the shallow coastal waters of Lake Ontario. The implementation of Philpot's (1989) principal components algorithm was successful under certain conditions. The approach used in this research to determine quantitative depth and bottom type information had serious limitations, but introduced the concept of incorporating the radiative transfer model, HydroMod, into this type of bathymetric research.

Philpot's method (1989) was chosen for implementation for a number of reasons. The first was ease of implementation. The algorithm consists mainly of a deep-water correction and principal components analysis (PCA), which was easy to implement because there are PCA programs available. The principal components algorithm was more flexible than other methods for bottom type mapping and water depth determination, because the main assumptions of Philpot's algorithm (1989) are vertically homogeneous water and constant water type. In addition, the algorithm takes advantage of the hyperspectral nature of the MISI images upon which it was implemented. The algorithm was implemented in a variety of situations on a MISI image (C9) taken 3 September 1999 on a perpendicular flight path over the Ginna power plant. This

particular image was selected for its perpendicular nature because there were more deep-water areas than in the parallel-to-shore images. Another benefit of the perpendicular image is that the deep water can be selected from an area of the image that has the same ground instantaneous field of view as the shallow water area that is being processed. Therefore, the deep water contains the same atmospheric conditions and lighting conditions as the shallow water from which it is being subtracted, which is important since the angular effects were not taken into account. In addition to the image near the Ginna power plant, an image taken on 5 July 2000 near Ontario Beach was processed in order to analyze the potential of the algorithm for future algae distribution mapping.

First, the entire shallow area in the C9 image taken near Ginna was processed by selecting different areas of the image for deep water. The selection of deep water had a great impact on the results of the processing. Substantial non-linearities occurred when a deep water area included different water types. One example included selecting deep water over the entire width of the image. This particular image contained different water types that were visible from the image itself, as shown in the C9 image of Ginna (Fig. 6.1).

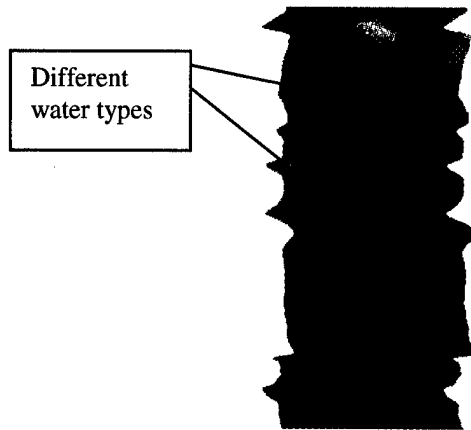


Figure 6.1 C9 image near Ginna power plant

By selecting the deepwater pixels over the entire width of the image, part of the light water from the left side of the image was included. The same light water does not appear in the shallow water areas of the image. The qualitative depth and bottom type maps from this particular example (Fig. 6.2 and 6.3) are inaccurate.

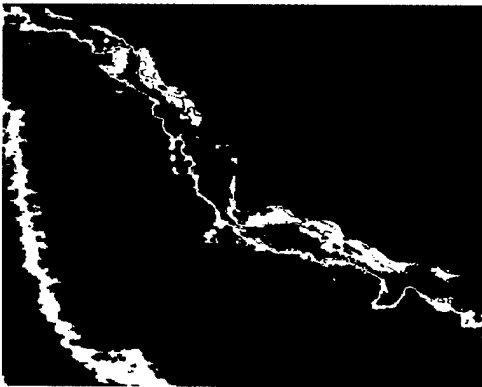


Figure 6.2 Y_{II} - deepwater of entire image
(~Depth)



Figure 6.3 Y_{I} - deepwater of entire image
(~Bottom type)

The bottom type map shows none of the bottom type variations that were visible from the image itself. The interpretation of the depth map is that the water becomes deeper moving away from shore and then becomes shallow again nearing the left edge of the image, where the lighter water occurs. Better results are obtained by selecting deepwater pixels from the right side of the image where the water appears to be more consistent with the water over the shallow areas. The scatter plot is significantly more linear than the plot obtained from the previous example. However, though they were improved over the example using deepwater from the entire width of the image, the bottom type map and water depth map (Fig. 6.4 and 6.5) were still inaccurate.

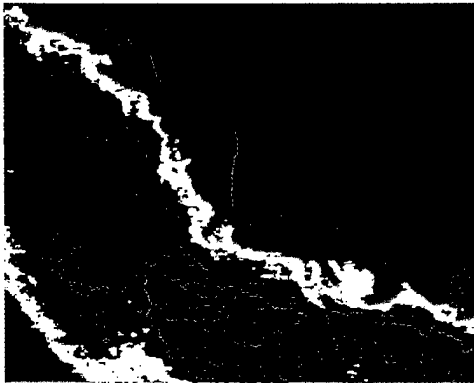


Figure 6.4 $\underline{Y}_{||}$ using deep water from right
(~Depth)

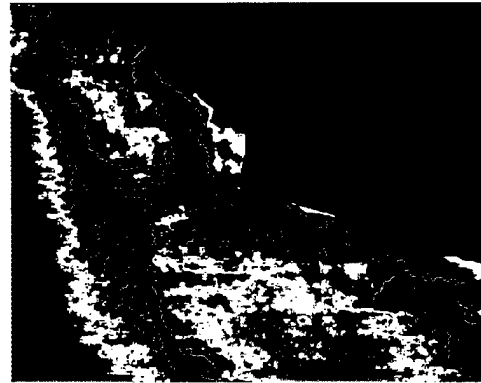


Figure 6.5 \underline{Y}_{\perp} using deep water from right
(~Bottom Type)

The depth map still showed the trend of the water getting deeper and then shallower moving away from shore, which ground truth and bathymetry disproved.

The nonlinearities of the above examples result from the deepwater correction, because several pixels are averaged to form a single deep-water observation, used to

linearize the entire shallow-water image. If the deep-water pixels contain different water types and/or if the shallow-water image contains different water types, the deep-water correction will lead to errors caused by these different water types.

The algorithm is more successful over smaller sections of the image because there is typically less variation in smaller portions. When a shallow water area from the right side of C9 is processed with deep-water pixels from the same columns of the image, the results are very intuitive. The water increased in depth moving further away from shore (Fig.6.6). The bottom type map (Fig. 6.7) picked up on bottom type variations that were visible in the image itself, but the bottom maps are somewhat correlated with depth.

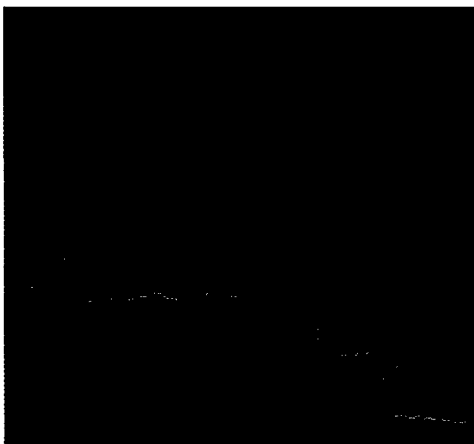


Figure 6.6 $\underline{Y}_{||}$ (~depth) for Ginna_right



Figure 6.7 \underline{Y}_{\perp} (~bottom type) for Ginna_right

Two additional sections of the image were chosen for processing because the corresponding deep-water pixels appeared to be of the same water type. The shallow water images overlapped and the interesting feature was a “trench” that appeared in both

of them. Some inaccuracies are still evident in these smaller images due to the presence of the lighter water and also variant lighting conditions.

The assumptions of the algorithm restrict its application to areas that contain invariant water type and atmospheric conditions. Another limitation involved in using the Case 2 assumptions (variable depth, variable bottom type, constant water type) is that the image must contain depth variation as well as bottom type variation. The images must be pre-processed to reduce noise effects, and as is evident in using the MISI images, the NIR bands may have to be deleted because they may contain mostly noise and very little signal. The NIR bands carry little information because these wavelengths do not penetrate very far into the water. The PCA picks up on any variation in the data; if there is significant noise, it becomes one of the main sources of variation. If the image contains land pixels, these must be masked out to eliminate land variability.

The flexibility and multiplicity of utilities that HydroMod has was demonstrated here. For a variety of bottom types, water types, and depths, water leaving radiances were generated for a particular atmosphere to be used as a calibration model for a Principal Components Regression. HydroMod radiance outputs matched expectations based on knowledge of the effect that aquatic component concentrations have on reflectance spectra. One of the September 3, 1999 Ginna water samples contained a relatively high amount of chlorophyll-a and total suspended solids, which could be seen in the spectrum of sensor-reaching radiances. The sample with high chlorophyll and TSS peaked in the green due to the chlorophyll and was significantly brighter than the other

spectra, which is characteristic when there is high TSS. This sample was collected from an area near the left side of the image, (Fig. 6.8), in the lighter water (A), which corresponds to the brighter spectra for this sample.

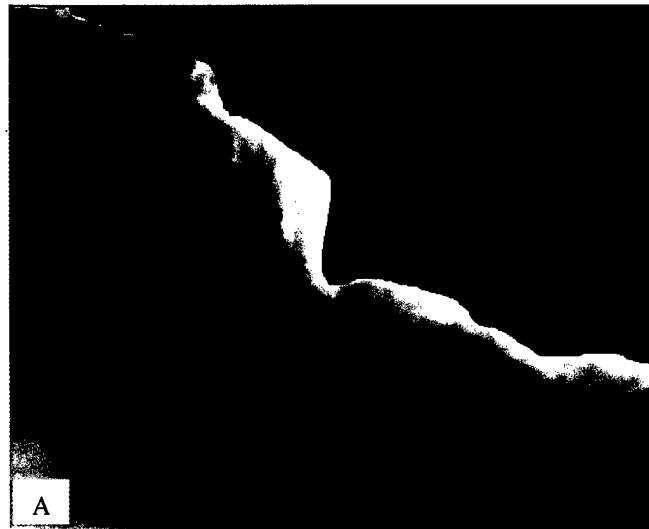


Figure 6.8 Smaller portion of Image C9 (Ginna)

For the 24 bands retained while working with the Ginna images, and also the HydroMod data, there was not significant difference between the shape of the spectra over the various bottom types, although there was some difference in magnitude. This is the reason why the z-profile method of verifying bottom type did not work. An area of the image that appeared to be a different bottom type was selected and then a z-profile of some of the pixels in that area were averaged and normalized. When all of the HydroMod spectra were normalized in an attempt to match the shape of the image z-profile to the normalized HydroMod spectra, the z-profile of the image bottom type consistently matched to Ontario sand. There was not enough variation in the spectra,

with the exception of HydroMod algae; however, there did not appear to be any areas in the image that consisted of HydroMod algae.

The Principal Components Regression approach to determining quantitative results from the algorithm had some success with the depth information, although there are serious limitations to this approach. PCR attempts to reduce the collinearity in the data, which is a problem for other linear regression models, by regressing the concentrations on the PCA scores as opposed to the constituent concentrations themselves. PCA can also have problems with collinearity, though, if the concentrations of two important constituents in the calibration samples are always present in the same ratio. The PCR was calibrated using the radiance outputs from HydroMod, for which the input “concentrations” of depth, water type, and bottom type were known. One limitation of this approach is that the model is scene-specific – the atmosphere, bottom types, and water types, are for a specific location and day. Another limitation is that determining the bottom types and water types for the scene is somewhat arbitrary. There are mixed bottom types at Ginna, containing some sand, some algae and some rock in mixed patches. It is difficult to model the radiance that comes from this mixture of bottom types.

The PCR on depth information resulted in a 0.82 m RMS error, which is not very accurate considering one of the inputs was 0.5 m. However, the depth estimates were somewhat consistent with the actual depths. The PCR on bottom type and water type information did not perform at all because regression does not work on categorical data,

which is grouped in categories with no ordinal significance. No information was gathered from PCR on these two inputs; each bottom type and water type were simply assigned a number to represent them, with no physical meaning to the number. More work needs to be done in this area, looking at categorical data analysis, or perhaps figuring out another way to relate categorical data to a principal component.

The eigenvector analysis on the model data showed that over 80% of the variability in the data is contained in the first principal component, and therefore is due to depth. Only 11.3% of the variability is due to bottom type. As discussed earlier, there was not significant variability in the radiance spectra. This method would perhaps work better in the Ontario Beach area where there are two bottom types that differ significantly, algae (or the rock it grows on) and sand. Another consideration is how many bands are retained; some of the bands that are deleted may contain most of the variability between bottom types.

Another limitation of PCR is that there is no guarantee that the largest common variations will be related to changes in the constituent concentrations (Galactic 2000). PCR will suffer if the constituent concentrations are collinear, which can be avoided by using many observations.

Regression coefficients for depth were obtained through PCR and applied to the actual image data from the C9 image of Ginna. The results were reasonable, although the approach is somewhat arbitrary. There is no indication of how many different bottom types, water types, or depths are needed to adequately calibrate the regression.

Monroe county is interested in the location of benthic algae near Ontario Beach in an attempt to manage the problem of dead algae washing up in the recreational areas. Some preliminary analysis was done to see if Philpot's algorithm (1989) would be of use in addressing the problem. A July 5, 2000 image taken parallel to shore, near the Ontario Beach area, was processed with the algorithm. Only a small section of the image was used due to noise, missing lines, and sun glare that runs down the middle of the image. The image, C2 is shown in Figure 6.9.



Figure 6.9 C2 - Image near Ontario Beach

The results of this processing were very encouraging for future work in this geographic area of the lake. There are predominantly two bottom types in the area – sand and rock with some algae growing on it. There were “ridges” in the image that was processed, as evidenced by the depth map and confirmed with ground truth. Also, the ridges were alternating bottom types, according to the map created using the second eigenvector and confirmed by ground truth. One of the characteristics of this image is that bottom type and depth are correlated, where there is sand, the water is shallower, and vice versa. The

effects of illumination conditions affected the right side of the depth map, which indicated that the water was shallow at the furthest point from shore. This is due to the glint that is down the center of the image C2 (Fig. 6.9), evidenced in the brighter right side of this portion of the image. The deep water was selected from a different portion of image C2, that is at a different angle from the shallow portion of the image, but the angle effects have not been analyzed here. This is an area for future study especially if most of the images that are being worked with are parallel to shore.

Images that are perpendicular to shore, or at least taken at a higher altitude, are better because there are more deepwater pixels. Images taken perpendicular to shore can take advantage of having deepwater pixels at the same angle from nadir as the portion of the image that is of interest. More perpendicular flight lines need to be planned for data collections.

Further work needs to be performed in taking advantage of the HydroMod data. Both the inputs and outputs for various conditions are known. The capability of this approach to relate depth to the principal components using the HydroMod data should be considered at the Ontario Beach area where there are two distinct bottom types.

Implementing Philpot's (1989) algorithm on MISI data was challenging, but under the proper conditions, it performed reasonably well in obtaining qualitative depth and bottom type information. There is definite promise in using this algorithm to process the Ontario Beach images to determine algae distributions in the area. HydroMod also has potential in this area; however, it needs to be developed further.

Works Cited

- Berk, A., L. S. Bernstein, and D. C. Robertson, "MODTRAN: a moderate resolution model for LOWTRAN 7, GL-TR-89-0122" Spectral Science, Burlington, MA (1989).
- Bierwirth, P. N., T. J. Lee, and R. V. Burne. "Shallow Sea-Floor Reflectance and Water Depth Derived by Unmixing Multispectral Imagery." *Photogrammetric Engineering & Remote Sensing*, Vol. 59, (1993): 331-338.
- Bricaud, A., A. Morel, and L. Prieur. "Absorption by Dissolved Organic Matter of the Sea (yellow substance) in the UV and Visible Domains." *Limnology and Oceanography*, Vol. 26, (1981): 43-53.
- Bricaud, A. and D. Stramski. "Spectral Absorption Coefficients of Living Phytoplankton and Nonalgal Biogenous Matter: A Comparison Between the Peru Upwelling and the Sargasso Sea." *Limnology and Oceanography*, Vol. 35, (1990): 562-582.
- Bukata, R. P., et al. "Optical Water Quality Model of Lake Ontario. 1: Determination of the Optical Cross Sections of Organic and Inorganic Particulates in Lake Ontario." *Applied Optics*, Vol. 20, (1981): 1696-1703.
- Bukata, R. P., J. H. Jerome, K. Y. Kondratyev, D. V. Pozdnyakov. *Optical Properties and Remote Sensing of Inland and Coastal Waters*. Boca Raton, FL, CRC Press, Inc., (1995).
- Clark, R. K., T. H. Fay, and C. L. Walker. "Bathymetry Calculations with Landsat 4 TM Imagery Under a Generalized Ratio Assumption." *Applied Optics*, Vol. 26, (1987): 4036-4037.

- Cleveland, J. S., and A. D. Weidemann. "Quantifying Absorption by Aquatic Particles: A Multiple Scattering Correction for Glass-Fiber Filters." *Limnology and Oceanography*, Vol. 38, (1993): 1321-1327.
- Fairbanks, R., Maj. PhD dissertation (1999).
- Gordon, H. R. and O. B. Brown. "Influence of Bottom Depth and Albedo on the Diffuse Reflectance of a Flat Homogeneous Ocean." *Applied Optics*, Vol. 13, (1974): 2153-2159.
- Galactic Industries Corp. "Principal Component Regression."
<http://www.galactic.com/algorithms/pcr.html> (2000).
- Gose, E., R. Johnsonbaugh, and S. Jost. *Pattern Recognition and Image Analysis*, (1996).
- Jackson, E. J. *A User's Guide to Principal Components*. New York, John Wiley & Sons, Inc. (1991).
- Jerlov, N. G. *Optical Oceanography*. Elsevier, New York (1976).
- Hamren-Larsson, M. <http://www.geog.ubc.ca/courses/klink/g472/class98/hamren-larsson/> (1998).
- Hickman, P. G., Jr., and J. E. Hogg. "Application of and Airborne Pulsed Laser for Near Shore Bathymetric Measurements." *Remote Sensing of the Environment*, Vol. 1, (1969).
- Kirk, J. T.O. *Light and Photosynthesis in Aquatic Ecosystems*. Cambridge, University Press (1983).
- Kirk, J. T. O. "The Upwelling Light Stream in Natural Waters." *Limnology and Oceanography*, Vol. 34, (1989): 1410-1425.

- Lyzenga, D. R., R. A. Shuchman, and R. A. Arnone. "Evaluation of an Algorithm for Mapping Bottom Features Under a Variable Depth of Water", reprinted from *Proceedings of the Thirteenth International Symposium on Remote Sensing of Environment*, (1979)
- Lyzenga, D. R. "Passive Remote Sensing Techniques for Mapping Water Depth and Bottom Features." *Applied Optics*, Vol. 17, (1978): 379-383.
- Lyzenga, D. R. "Remote Sensing of Bottom Reflectance and Water Attenuation Parameters in Shallow Water Using Aircraft and Landsat Data." *International Journal of Remote Sensing*, Vol. 2 (1981): 71-82.
- Lyzenga, D. R. "Shallow-water Bathymetry Using Combined Lidar and Passive Multispectral Scanner Data." *International Journal of Remote Sensing*, Vol 6, (1985): 115-125
- Maritorena, S., A. Morel, and B. Gentili. "Diffuse Reflectance of Oceanic Shallow Waters: Influence of Water Depth and Bottom Albedo." *Limnology and Oceanography*, Vol. 39, (1994): 1689-1703.
- Mitchell, B. G. "Algorithms for Determining the Absorption Coefficient of Aquatic Particulates Using the Quantitative Filter Technique (QFT)." *SPIE Vol. 1302 Ocean Optics X*, (1990): 137-148.
- Mobley, Curtis D. "HYDROLIGHT 3.0 User's Guide", SRI International, SRI Project Number 5632 Final Report, Office of Naval Research Contract number N00014-94-C-0062, Menlo Park, CA (1995).

- Mobley, Curtis D. "HYDROLIGHT 3.1 User's Guide", SRI International, SRI Project Number 6583 Final Report, Office of Naval Research Contract number N00014-95-C-0238, Menlo Park, CA (1996).
- Mobley, C. D. *Light and Water*. San Diego, CA., Academic Press (1994).
- Monroe County Environmental Health Lab. "1998 Ontario Beach Monitoring Report." (1998).
- Murtagh, F. *Multivariate Data Analysis*. Dodrecht, Kluwer Academic Publishers (1987).
- Paredes, J. M., and R. E. Spero. "Water Depth Mapping From Passive Remote Sensing Data Under a Generalized Ratio Assumption." *Applied Optics*, Vol. 22, (1983): 1134-1135.
- Philpot, W. D. "Bathymetric Mapping With Passive Multispectral Imagery." *Applied Optics*, Vol. 28, (1989): 1569-1578.
- Rosenshein, J. S., C. R. Goodwin, and Antonio Jurado. "Bottom Configuration and Environment of Tampa Bay." *Photogrammetric Engineering*, Vol. 43, (1977): 693-699.
- Schott, J. R. *Remote Sensing: The Image Chain Approach*. Oxford, Oxford University Press, 1997.
- Smith, R. C. and K. S. Baker. "Optical Properties of the Clearest Natural Waters (200-800 nm)." *Applied Optics*, Vol. 20, (1981): 177-184.
- Spitzer, D., and R. W. J. Dirks. "Bottom Influence on the Reflectance of the Sea." *International Journal of Remote Sensing*, Vol. 8, (1987): 279-290.
- Strong, A. E. "Chemical Whitings and Chlorophyll Distributions in the Great Lakes as Viewed by Landsat." *Remote Sensing of Environment*, Vol. 7, (1978): 61-72.

Tewinkel, G. C. "Water Depths from Aerial Photographs." *Photogrammetric Engineering*, Vol. 29, (1963): 1037-1042.

Vodacek, A., N.V. Blough, M. D. DeGrandpre, E. T. Peltzer, and R. K. Nelson.

"Seasonal Variation of CDOM and DOC in the Middle Atlantic Bight: Terrestrial Inputs and Photooxidation." *Limnology and Oceanography*, Vol 42, (1997): 674-686.

Wezernak, C.T. and D.R. Lyzenga. "Analysis of Cladophora Distribution in Lake Ontario Using Remote Sensing." *Remote Sensing of Environment*, Vol. 4, (1975): 37-48.

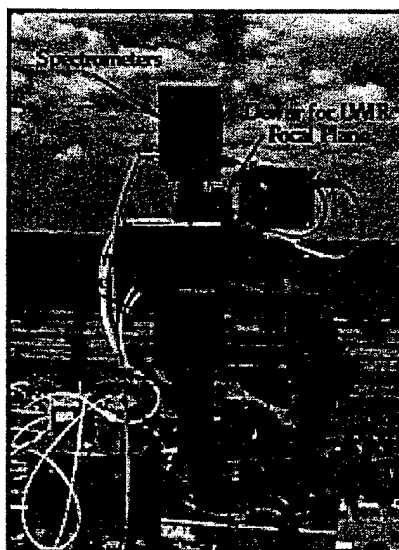
Appendix A: MISI Information

Modular Imaging Spectrometer Instrument (MISI)

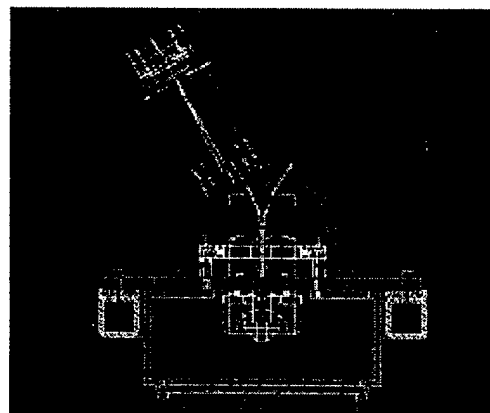
The Digital Imaging and Remote Sensing Group at RIT has constructed an imaging spectrometer called the Modular Imaging Spectrometer Instrument which is a line scanner with a 6" rotating mirror coupled to a Cassegrain telescope of focal ratio $f/3.3$. Two 0.5mm square silicon detectors (broad-band visible) and two 1.5mm fiber optics are placed at the primary focal plane to give a GIFOV of 0.3 m and 1.0 m respectively at 0.3 km of altitude. The fibers lead to two separate 36-channel spectrometers to cover the EM spectrum from $0.440\mu\text{m}$ to $1.020\mu\text{m}$ in $0.010\mu\text{m}$ spectral bands. A pyramid mirror diverts some photons from the primary focal plane to five HgCdTe detectors for the long-wave infrared region; secondary focal planes are available in the SWIR and MWIR for future use (Feng, 1995). An on-board calibration system consisting of two blackbodies for the LWIR and a tungsten source for the visible completes this imaging system for gathering absolute radiometrically calibrated data for remote sensing applications.

The system is designed to serve as:

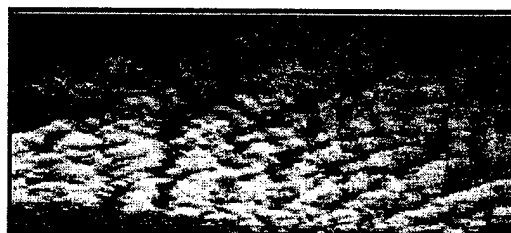
- an airborne laboratory for earth observation research
- a high resolution under-flight system for high-altitude aircraft and satellite sensor performance evaluation
- a versatile data collection platform for acquiring imagery to be used in algorithm development and evaluation for reconnaissance and environmental application
- and as a survey instrument for demonstration and proof-of-concept studies of image analysis methods in areas such as energy conservation, water quality assessment, and hazardous waste site management



The Modular Imaging Spectrometer Instrument (MISI)



An AutoCad schematic of MISI



The MISI Optical System

The Spectral Calibration of MISI

The Thermal Calibration of MISI

Web Reference:

Feng, Xiaofan., "Design and Performance of a Modular Imaging Spectrometer Instrument", Rochester Institute of Technology Ph.D. Dissertation, (1995).

Previous Project | Next Project

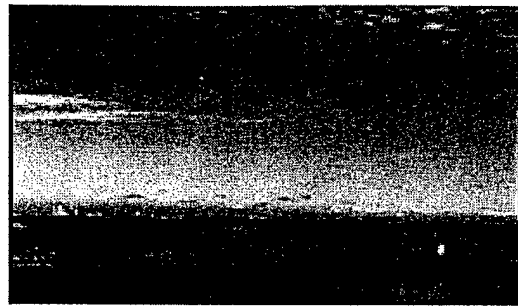
Places to Go

[Faculty](#)

[Areas of Research](#)

[Send a Comment](#)

[DIRS Web Resources](#)



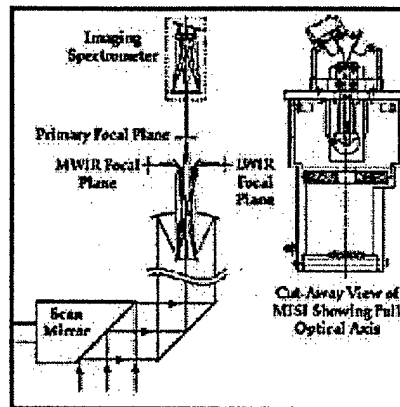
First Line-Scan Image Taken by the Broad-Band Visible Detectors on the MISI of the Rochester Skyline (12/02/95).



First Line-Scan Image Taken by the Broad-Band Visible Detectors on the MISI of the RIT Dormitories (12/02/95).

The MISI Optical System

The overall optical system with the various focal planes is shown in the figure. The 6-inch clear aperture scan mirror will spin at up to 40 revolutions per second and folds the image onto a second fold mirror which reflects the image into the Dall-Kirkham Cassegrainian-style telescope. The converging image is split onto four slightly off-axis (less than 2 degrees) focal planes by a four-sided pyramid mirror. The on-axis rays pass through a hole in the center of the pyramid mirror and are used to sample the visible/near-infrared EM region. Of the four off-axis focal planes, two are in the along-track scan direction (one fore and one aft of the primary optical axis) and two are in the cross-track direction (one leading, one lagging the primary optical axis). Presently, only the on-axis (VIS/NIR) and cross-track (long-wave infrared) focal planes are utilized. The along-track focal planes are intended for additional detector modules. The modular nature of the focal planes allow for easy addition of new detectors arrays or modification of the existing ones. The total field-of-view is 90 degrees (plus/minus 45 degrees) with calibration standards being viewed within every full rotation.



Line-Scanner Optical Schematic Showing Complete Radiation Path From Ground

[Previous Project](#) | [Next Project](#)

Places to Go

[Faculty](#)

[Areas of Research](#)

[Send a Comment](#)

[DIRS Web Resources](#)

Spectral Calibration of MISI Spectrometer Channels

With hyperspectral imaging, the absolute spectral calibration is extremely important since the detector response function is convolved with the estimate of the radiance-at-the-sensor (during the inversion to reflectance process). The detector response function itself (for typical hyperspectral systems) is completely characterized by the center wavelength and FWHM (full width half-max) of the gaussian. Errors in center spectral wavelength because of poor spectral calibration technique can result in gross radiometric errors when performing analysis on spectral features of ground targets that require spectral match-up.

By illuminating a spectroradiometer with a stable spectral line source, such as Mercury or Argon lamp, the spectroradiometer can be spectrally calibrated to tolerances tighter than 0.1nm. The spectroradiometer can then be used illuminate the hyperspectral sensor array with narrow bandwidth light to find the maximum spectral response point (center) and FWHM of the typically Gaussian detector response function. From a discrete, fine scan through the visible wavelengths, the detector response functions for each channel of the imaging spectrometer can be determined. This spectral scan can also be used to find cross-talk between spectral channels as well as determine if there is grating misalignment in the hyperspectral imager.

[Previous Project](#) | [Next Project](#)

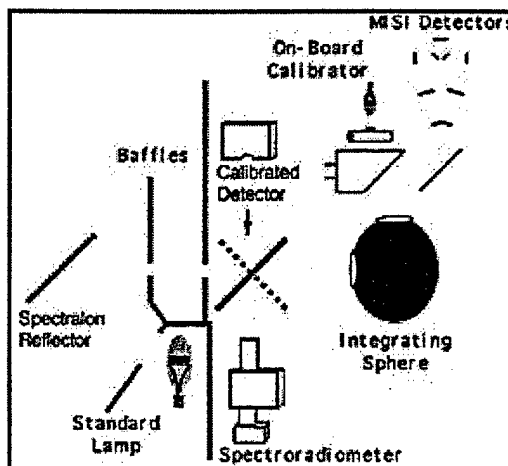
Places to Go

[Faculty](#)

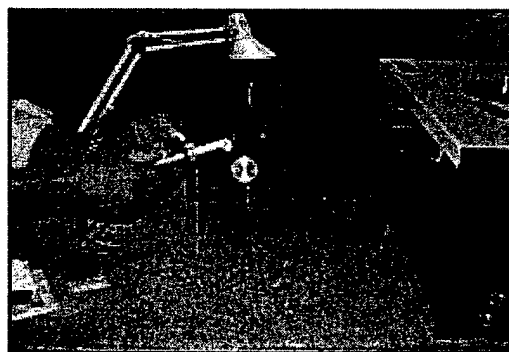
[Areas of Research](#)

[Send a Comment](#)

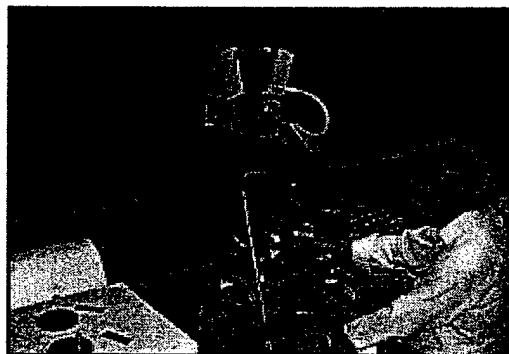
[DIRS Web Resources](#)



Overhead view of absolute radiometric calibration set up.



A Mercury line source is used to calibrate the monochromator.



A broad-band source is then put through the monochromator (illumination with 2.5nm bandwidths of light), collimated (since the MISI optics are focused at infinity), and detected at the spectrometer focal plane.

Appendix B: IDL Programs

PRO deepwater, deepwater_mean

```
; NAME:
;   deepwater
;
; PURPOSE:
;   Read in the area that has been selected as "deep water" from
;   the MISI image. It will average the pixels over each band in
;   the image, returning a vector.
; EXPLANATION:
;   Program called by runpca_ginna.pro for use in deepwater
;   subtraction
;
; CALLING SEQUENCE:
;   deepwater, deepwater_mean
;
; INPUT PARAMETERS
;   None. The deepwater_filename is hardcoded into this procedure.
;   MISI images must be read into an intarr() because they are
;   unsigned integer
;
; OUTPUT PARAMETERS
;   deepwater_mean = a 1 column by zsize vector which contains the
;   average of the pixels over each band
;
; NOTES:
;   Make sure that the deepwater_filename corresponds to the image
;   that is being processed with runpca_ginna.pro
;
; REVISION HISTORY:
;   Nikole Wilson      November 1999
```

;Name of the deepwater file. Assumes file is BSQ and hardcoded

```
deepwater_filename='/dirs/home/nlw4923/C9/ginna_right_deep'
```

```
Dimensions of the deepwater image hardcoded
xsize=308.0 ; Number of columns in deepwater image
ysize=16.0  ; Number of rows in deepwater image
zsize=24.0  ;number of bands
```

;Print size of deepwater image before read to check dimensions

```
print, "size of deepwater filename"
```

```
print, size(deepwater_filename)
```

;Reading in the deepwater image

```
deepwater_image = intarr(xsize, ysize, zsize)
```

```
    print, "size of deepwater image before read"
```

```
    print, size(deepwater_image)
```

```
    openr,lun,deepwater_filename,/GET_LUN
```

```
    readu,lun,deepwater_image
```

```
    close,lun
```

```
    Free_LUN,lun
```

;Print size of deepwater image after read

```
print, "size of deepwater image"
```

```
print, size(deepwater_image)
```

```
;Getting MISI image calibrated radiance values into uW/cm^2sr^-1nm^-1
;because these are the units on the HydroMod output
deepwater_image=temporary(deepwater_image)/100.0

;Setting up the array which will hold the average value in each of
;the z bands

deepwater_mean=fltarr(zsize)

for i=0,(zsize-1) do begin
    sum = total(deepwater_image[*,* ,i])
    deepwater_mean[i]=sum/(xsize*ysize)
endfor

;Printing out the average of the deepwater image
print,'deepwater mean'
print,deepwater_mean
print,size(deepwater_mean)

deepwater_mean=transpose(temporary(deepwater_mean))

END
```

PRO runpca_ginna, shore_image, a, eigenval, percentages, x, final, yest

```
; NAME:
;   runpca_ginna
;
; PURPOSE:
;   Implements Philpot's principal components algorithm (1989) on a
;   MISI image. Also applies the regression coefficients obtained
;   through principal components regression on HydroMod model data
;   in pcrtest.pro
;
; EXPLANATION:
;   The pc scores are stored in the parameter, final
;   which can be imported into ENVI. The first band in final
;   corresponds to the data multiplied by the first eigenvector,
;   which provides depth information. The second band in final
;   corresponds to bottom type information.
;
; CALLING SEQUENCE:
;   runpca_ginna, shore_image, a, eigenval, percentages, x, final, yest
;
; INPUT PARAMETERS:
;   None. The shore_image is read into the procedure. It must be
;   read into an intarr because the MISI data is in unsigned integer.
;   The regression coefficient matrix, b, is also read in.
;
; OUTPUT PARAMETERS:
;   shore_image: the MISI image being processed by the algorithm
;   a = zsize by zsize matrix containing the eigenvectors
;   eigenval = zsize element vector containing the sorted eigenvalues
;   percentages = zsize element vector containing the cumulative
;                 percentage variances associated with the
;                 principal components
;   x = xsize x ysize x zsize matrix of deepwater-corrected data
;       (linearized data)
;   final = xsize x ysize x zsize matrix of transformed data.
;           Obtained by multiplying the matrix x by a. The first
;           band is the matrix Y, which corresponds to depth
;           information and is a qualitative depth map. The second
;           band is the matrix Y^, which corresponds to bottom
type
;           information and is a qualitative bottom type map
;   yest = 1 x h vector of quantitative depth information obtained by
;         applying the regression coefficients, b, to the first
;         score (1st eigenvector x the data)
;
; NOTES: The land must be masked in shore_image and set to a value of
;        -1 so the land pixels are not included in the principal
;        components analysis. The radiance values in shore_image are
;        changed from calibrated radiances to  $\mu\text{W}/\text{cm}^2\text{sr}^{-1}\text{nm}^{-1}$ 
;        so the image data is in the same units as the HydroMod output
;
; PROCEDURES CALLED:
;   deepwater, astrolib, pca
;
; REVISION HISTORY:
;   Nikole Wilson November 1999
;   Added ability to process just the unmasked data N. Wilson Jun '00
;   Algorithm taken from Philpot (1989)
```

```

;Call deepwater procedure to read in the deepwater average vector
deepwater,deepwater_image,deepwater_mean
deepwater_mean=transpose(temporary(deepwater_mean))

;Opening shore_image

shore_filename='/dirs/home/nlw4923/C9/ginna_right'
;Setting up array for shore image
xsize=308.0
ysize=284.0
zsize=24.0
;Reading bsq shore image into an array
shore_image=intarr(xsize,ysize,zsize)
    print, "size of shore image before read"
    print, size(shore_image)
    openr,lun,shore_filename,/GET_LUN
    readu,lun,shore_image
    close,lun
    Free_LUN,lun

;Setting up shore image into a 2-d array with the pixels down the side
;and the bands across the top
g=xsize*ysize
shore_image = reform(temporary(shore_image),g,zsize)
;changing it to floating point data
shore_image=temporary(shore_image)*1.0
;changing calibrated radiances into uW/cm^2sr^-1nm^-1
shore_image=temporary(shore_image)/100.0
;assigning water pixels to matrix "values"
values=where(shore_image gt -.005,count);the mask value of -1 has been
                                         ;changed due to changing the
                                         ;units

;setting up one band image with the mask values so the yest matrix
;determined near the end can be reformed into the original spatial
;information
one_band=shore_image(*,*,0)
values_one_band=where(one_band gt -0.005,values_count)

h=count/zsize ;determining the number of observations that are just
               ; water pixels for dimensioning purposes
print,'shore_image has been reformed into a 2d matrix'
print,''
print,'Size of shore_image:'
print, size(shore_image)
values_array=shore_image(values)
print,'size of values array:'
print,size(values_array)
;Reforming the water pixels into an array with h columns and
;zsize rows for the deepwater subtraction
values_array=reform(temporary(values_array),h,zsize)

;Setting up a unit vector as big as the shore image so I can multiply
;it by the deepwater mean in order to subtract
;the mean matrix from the shore image or vice versa if the mean matrix
;value is larger than the shore_image value

```

```

mean=fltarr(h,zsize)

temp=(replicate(1.0,h,1))
print,'unit vector has been set up'
print,size(mean)
mean=deepwater_mean##temp
print,'mean_matrix has been created'
print,size(mean)
print,size(shore_image)

;Deepwater subtraction

;Subtract mean_matrix from shore_image.
x=fltarr(h,zsize)
;for i=0L,(g-1) do begin
for i=0L,(h-1) do begin
    for j=0,(zsize-1) do begin
        if (values_array(i,j) gt mean(i,j)) $
            then x(i,j)=(values_array(i,j)-mean(i,j)) else $
                x(i,j)=(mean(i,j)-values_array(i,j))
    endfor
endfor

print,'just ran loop'
print,size(x)

;Take natural log of non-zero data
logx= x*1.0
templogx=alog(x(where(x ne 0)))

logx(where(logx ne 0))=templogx
print,'Performed natural log function'

data=fltarr(zsize,h)
data=transpose(logx)
print,'data'
print,size(data)

;Reshaping linearized data (X) into original size image
shore_image(values)=logx
x=reform(shore_image,xsize,ysize,zsize)

data=transpose(temporary(data))

;Calling astrolib procedure to run two procedures that are required
;for PCA.pro
astrolib
;Running PCA.pro,
PCA,data,eigenval,eigenvect,percentages,/covariance,/silent

plot,eigenval

a=eigenvect
scores=transpose(a)##data
shore_image(values)=scores
final=reform(shore_image,xsize,ysize,zsize)

```

```
scores=transpose(scores)
xforpcr=fltarr(2,63972)
xforpcr(0,*)=1.0
xforpcr(1,*)=scores(0,*)
b=fltarr(1,2)
fname='/dirs/home/nlw4923/C9/b'
openr,unit,fname,/get_lun
readf,unit,b
close,unit
free_lun,unit

yest=xforpcr##b

print,'size of yest:',size(yest)

print,'done'

end
```

```

PRO PCA, data, eigenval, eigenvect, percentages, proj_obj, proj_atr, $
    MATRIX=AM,TEXTOUT=textout,COVARIANCE=cov,SSQ=ssq,SILENT=silent

;+
; NAME:
;   PCA
;
; PURPOSE:
;   Carry out a Principal Components Analysis (Karhunen-Loeve
Transform)
; EXPLANATION:
;   Results can be directed to the screen, a file, or output variables
;   See notes below for comparison with the intrinsic IDL function
PCOMP.
;
; CALLING SEQUENCE:
;   PCA, data, eigenval, eigenvect, percentages, proj_obj, proj_atr,
;       [MATRIX =, TEXTOUT =, /COVARIANCE, /SSQ, /SILENT ]
;
; INPUT PARAMETERS:
;   data - 2-d data matrix, data(i,j) contains the jth attribute
value
;           for the ith object in the sample.   If N_OBJ is the
total
;           number of objects (rows) in the sample, and N_ATTRIB is
the
;           total number of attributes (columns) then data should be
;           dimensioned N_OBJ x N_ATTRIB.
;
; OPTIONAL INPUT KEYWORD PARAMETERS:
;   /COVARIANCE - if this keyword is set, then the PCA will be carried
out
;               on the covariance matrix (rare), the default is to use
the
;               correlation matrix
;   /SILENT - If this keyword is set, then no output is printed
;   /SSQ - if this keyword is set, then the PCA will be carried out on
;         on the sums-of-squares & cross-products matrix (rare)
;   TEXTOUT - Controls print output device, defaults to !TEXTOUT
;
;           textout=1      TERMINAL using /more option
;           textout=2      TERMINAL without /more option
;           textout=3      <program>.prt
;           textout=4      laser.tmp
;           textout=5      user must open file
;           textout = filename (default extension of .prt)
;
; OPTIONAL OUTPUT PARAMETERS:
;   eigenval - N_ATTRIB element vector containing the sorted
eigenvalues
;   eigenvect - N_ATTRIB x N_ATTRIB matrix containing the
corresponding
;               eigenvectors
;   percentages - N_ATTRIB element containing the cumulative
percentage
;               variances associated with the principal components
;   proj_obj - N_OBJ by N_ATTRIB matrix containing the projections of
the
;               objects on the principal components
;   proj_atr - N_ATTRIB by N_ATTRIB matrix containing the projections
of

```

```

;           the attributes on the principal components
;
; OPTIONAL OUTPUT PARAMETER
;   MATRIX   = analysed matrix, either the covariance matrix if
/COVARIANCE
;           is set, the "sum of squares and cross-products" matrix if
;           /SSQ is set, or the (by default) correlation matrix.
Matrix
;           will have dimensions N_ATTRIB x N_ATTRIB
;
; NOTES:
;   This procedure performs Principal Components Analysis (Karhunen-
Loeve
;   Transform) according to the method described in "Multivariate
Data
;   Analysis" by Murtagh & Heck [Reidel : Dordrecht 1987], pp. 33-48.

;
;   Keywords /COVARIANCE and /SSQ are mutually exclusive.
;
;   The printout contains only (at most) the first seven principle
;   eigenvectors.  However, the output variables EIGENVECT contain
;   all the eigenvectors
;
;   Different authors scale the covariance matrix in different ways.
;   The eigenvalues output by PCA may have to be scaled by 1/N_OBJ or
;   1/(N_OBJ-1) to agree with other calculations when /COVAR is set.
;
;   PCA uses the non-standard system variables !TEXTOUT and
!TEXTUNIT.
;   These can be added to one's session using the procedure ASTROLIB.
;
;   The intrinsic IDL function PCOMP (introduced in V5.0) duplicates
most
;   most of the functionality of PCA, but uses different conventions
and
;   normalizations.  Note the following:
;
;   (1) PCOMP requires a N_ATTRIB x N_OBJ input array; this is the
transpose
;       of what PCA expects
;   (2) PCA uses standardized variables; use /STANDARDIZE keyword to
PCOMP
;       for a direct comparison.
;   (3) PCA (unlike PCOMP) normalizes the eigenvectors by the square
root
;       of the eigenvalues.
;   (4) PCA returns cumulative percentages; the VARIANCES keyword of
PCOMP
;       returns the variance in each variable
;
; EXAMPLE:
;   Perform a PCA analysis on the covariance matrix of a data matrix,
DATA,
;   and write the results to a file
;
;   IDL> PCA, data, /COVAR, t = 'pca.dat'
;
;   Perform a PCA analysis on the correlation matrix.  Suppress all
;   printing, and save the eigenvectors and eigenvalues in output
variables

```

```

;
; IDL> PCA, data, eigenval, eigenvect, /SILENT
;
; PROCEDURES CALLED:
; TEXTOPEN, TEXTCLOSE
;
; REVISION HISTORY:
; Immanuel Freedman (after Murtagh F. and Heck A.). December
1993
; Wayne Landsman, modified I/O December 1993
; Converted to IDL V5.0 W. Landsman September 1997
; Fix MATRIX output, remove GOTO statements W. Landsman August
1998
; Changed some index variable to type LONG W. Landsman March
2000
;-
  On_Error,2 ;return to user if error

; Constants
  TOLERANCE = 1.0E-5 ; are array elements near-zero ?

; Dispatch table

IF N_PARAMS() EQ 0 THEN BEGIN
  print,'Syntax - PCA, data, [eigenval, eigenvect, percentages,
proj_obj, proj_atr,'
  print,' [MATRIX =, /COVARIANCE, /SSQ, /SILENT,
TEXTOUT=]'
  RETURN
ENDIF

  SZ = size(data)
  if SZ[0] NE 2 THEN $
  BEGIN
    HELP,data
    MESSAGE,'ERROR - Data matrix is not two-dimensional'
  ENDIF

  Nobj = sz[1] & Mattr = sz[2] ;Number of objects and attributes

  IF KEYWORD_SET(cov) THEN BEGIN
    msg = 'Covariance matrix will be analyzed'
; form column-means
    temp = replicate(1.0, Nobj)
    column_mean = (temp # data)/Nobj
    X = (data - temp # transpose(column_mean))
  ENDIF ELSE $
  IF KEYWORD_SET(ssq) THEN BEGIN

    msg = 'Sum-of-squares & cross-products matrix will be analyzed'
    X = data

  ENDIF ELSE BEGIN
    msg = 'Default: Correlation matrix will be analyzed'
; form column-means
    temp = replicate( 1.0, Nobj )
    column_mean = (temp # data)/ Nobj
    X = (data - temp # transpose(column_mean))
    S = sqrt(temp # (X*X)) & X = X/(temp # S)
  
```

```

ENDELSE

A = transpose(X) # X
if arg_present(AM) then AM = A

; Carry out eigenreduction
trired, A, D, E          ; D contains diagonal, E contains off-
diagonal
triql, D, E, A          ; D contains the eigen-values, A(*,i) -
vectors

; Use TOLERANCE to decide if eigenquantities are sufficiently near zero

index = where(abs(D) LE TOLERANCE*MAX(abs(D)),count)
if count NE 0 THEN D[index]=0
index = where(abs(A) LE TOLERANCE*MAX(abs(A)),count)
if count NE 0 THEN A[index]=0

index = sort(D)          ; Order by increasing eigenvalue
D = D[index] & E=E[index]
A = A[* ,index]

; Eigenvalues expressed as percentage variance and ...
W1 = 100.0 * reverse(D)/total(D)

;... Cumulative percentage variance
C = replicate(1., Mattr, Mattr)
for j = 1L, Mattr-1 do C[0,j] = fltarr(j)
W = C # W1

;Define returned parameters
eigenval = reverse(D)
eigenvect = reverse(transpose(A))
percentages = W

; Output eigen-values and -vectors

if not keyword_set(SILENT) then begin
;   Open output file
if not keyword_set( TEXTOUT ) then TEXTOUT = textout
textopen,'PCA', TEXTOUT = textout
printf,!TEXTUNIT,'PCA: ' + systime()
sz1 = strtrim( Nobj,2) & sz2 = strtrim( Mattr, 2 )
printf,!TEXTUNIT, 'Data matrix has '+ sz1 + ' objects with up
to ' + $
           sz2 + ' attributes'
printf,!TEXTUNIT, msg
printf,!TEXTUNIT, " "
printf,!TEXTUNIT, $
percentages'
           Eigenvalues      As Percentages      Cumul.
for i = 0L, Mattr-1 do $
printf,!TEXTUNIT, eigenval[i], W1[i], percentages[i] ,f =
'(3f15.4)'
printf,!TEXTUNIT," "
printf,!TEXTUNIT, 'Corresponding eigenvectors follow...'
Mprint = Mattr < 7
header = ' VBLE '
for i = 1, Mprint do header = header + ' EV-' + strtrim(i,2) +
printf,!TEXTUNIT, header

```

```

        for i = 1L, Mattr do printf,!TEXTUNIT, $
            i, eigenvect[0:Mprint-1,i-1],f='(i4,7f9.4)'
        endif

; Obtain projection of row-point on principal axes (Murtagh & Heck
convention)
projx = X # A

; Use TOLERANCE again...
index = where(abs(projx) LE TOLERANCE*MAX(abs(projx)),count)
if count NE 0 THEN projx[index]=0
proj_obj = reverse( transpose(projx) )

if not keyword_set( SILENT ) then begin
    printf,!TEXTUNIT,' '
    printf,!TEXTUNIT, 'Projection of objects on principal axes ...'
    printf,!TEXTUNIT,' '
    header = ' VBLE '
    for i = 1, Mprint do header = header + 'PROJ-' + strtrim(i,2) +
    ,

    printf,!TEXTUNIT, header
    for i = 0L, Nobj-1 do printf,!TEXTUNIT, $
        i+1, proj_obj[0:Mprint-1,i], f='(i4,7f9.4)'
endif

; Obtain projection of column-points on principal axes
projy = transpose(projx)#X

; Use TOLERANCE again...
index = where(abs(projy) LE TOLERANCE*MAX(abs(projy)),count)
if count NE 0 THEN projy[index] = 0

; scale by square root of eigenvalues...
temp = replicate( 1.0, Mattr )
proj_atr = reverse(projy)/(sqrt(W)#temp)

if not keyword_set( SILENT ) then begin
    printf,!TEXTUNIT,' '
    printf,!TEXTUNIT,'Projection of attributes on principal axes
...
    printf,!TEXTUNIT,' '
    printf,!TEXTUNIT, header
    for i = 0L, Mattr-1 do printf,!TEXTUNIT, $
        i+1, proj_atr[0:Mprint-1,i], f='(i4,7f9.4)'
    textclose, TEXTOUT = textout ; Close output file
endif

RETURN
END

```

Appendix C: Standard Methods Chl-a process

ENVIRONMENTAL HEALTH LABORATORY
STANDARD OPERATING PROCEDURES

8/9/96

PAGE 1

CHLOROPHYLL a

I. TITLE: CHLOROPHYLL a

II. DESCRIPTION:

Chlorophyll a constitutes approximately 1 to 2% of the dry weight of organic material in all planktonic algae and is the preferred indicator for algal biomass estimates.

Application: This method measures the amount of photosynthetic pigments in the water, both chlorophyll a, and its degradation product, pheophytin a. Interferences from less important pigments are corrected for by the use of several wavelengths.

Summary of Method : The sample is filtered to remove algae. The filter with the algae is then ground in aqueous acetone stored over MgCO₃ to extract the chlorophyll from the cells. The extract is centrifuged to remove the filter and cellular debris, and absorbance is read on a spectrophotometer. Four wavelengths are read. Each pigment absorbs at a particular wavelength, for example: chl. c absorbs at 630 nm, chl. b absorbs at 647 nm, chl. a absorbs at 664 nm and the turbidity blank is measured at 750 nm. The extract is then acidified so as to break down the chlorophyll a to pheophytin. Absorbance is read again. The absorbance values are then used in equations, which compensate for the various interferences, to obtain final results.

III. REFERENCE

Standard Methods, 18th ed., p.10-18, 10200H spectrophotometric method (1992)

IV. ENVIRONMENTAL LABORATORY APPROVAL PROGRAM (ELAP) Method code

none

V. SPECIAL SAFETY PRECAUTIONS: See Material Safety Data Sheets (MSDS) for:

- a. acetone
- b. magnesium carbonate, MgCO₃
- c. hydrochloric acid, HCl, concentrated

VI. PRECISION STATEMENT -based on 1996 data

<u>RANGE</u>	<u>ANALYTE</u>	<u>MEAN</u>	<u>UWL</u>	<u>UCL</u>
< 25 µg/L	Uncor. Chlor a	0.38	0.96	1.25
	Cor. Chlor a	0.74	1.86	2.41
	Pheophytin	0.79	1.99	2.59
> 25 µg/L	Uncor. Chlor a	7.3	na	24
	Cor. Chlor a	na	na	na
	Pheophytin	na	na	na

ENVIRONMENTAL HEALTH LABORATORY
STANDARD OPERATING PROCEDURES

8/9/93

PAGE 2

VII. ACCURACY STATEMENT

no external standards are available for this analysis at this time

VIII. EQUIPMENT AND SUPPLIES

Note that all glassware must be acid-free

- A. Spectrophotometer, with a narrow band resolution (0.5 to 2 nm) Use the Varian DMS-90 UV-visible spectrophotometer.
- B. Cuvettes - matched with 2 cm path length.
- C. Tissue grinder, ground glass-ground glass - A.H.T. Co. #126
- D. Centrifuge - use the DYNAC in the ME Lab.
- E. Centrifuge tubes - 15ml glass - marked with line at 12 cm.
- F. Corks - to stopper the centrifuge tube
- G. Filtration equipment:
 1. Filter unit
 2. Membrane filters (Millipore brand) - 0.45 μ m porosity, 47 mm diameter.
 3. Vacuum port with valve
- H. Pasteur pipet with bulb
- I. Automatic pipettor adjusted to deliver 2.80 ml
- J. 1 ml graduated pipet with pipetting bulb
- K. 250 ml graduated cylinder

IX. REAGENTS

- A. Magnesium Carbonate Suspension 1%
add 1.0 g finely powdered $MgCO_3$ to 100 ml deionized distilled water. Stir well.
Note - this will not go into solution.
- B. Aqueous Acetone Solution, 90% (also known as 9 + 1)
mix 900 ml acetone (reagent grade BP 56 c) with 100 ml deionized distilled water. (Final vol. will be less than 1000 ml).
- C. 90% Acetone Containing Magnesium Carbonate Suspension
mix 900 ml acetone with the above 100 ml of magnesium carbonate suspension
- D. Hydrochloric acid, HCl, 1N
Dilute 8.4 ml. concentrated HCl to 100 ml with deionized distilled water.
- E. Hydrochloric acid, 0.1N
Dilute 3 ml 1N HCl to 30 ml.

X. PRESERVATION AND HOLDING TIMES

1. Volume required: about 250 ml
2. Preservation:
Filter within 24 hours, place filter with sample in a corked centrifuge tube. If the sample is then frozen and kept in the dark, it can be held up to 3 weeks.

XI. PROCEDURE

Note that Chlorophyll a is easily broken down by acids, light, and heat. All glassware should be acid-free, and samples should be processed away from excessive light and heat. Also samples should be covered to protect them from light when not being handled.

A. Filtration:

1. Shake sample to mix. Using the graduated cylinder, measure 250 ml of the sample.
2. Pour sample into the filtering unit with the filter in place and turn on the suction.
3. Rinse down the cylinder with the deionized distilled water and pour this into the filtering apparatus. Also rinse down the filter unit.
4. Remove the membrane filter from the filtering unit. Fold the filter 4 times and place into a centrifuge tube labeled w/the sample #, and stopper with a cork.
5. If the extraction is to be done at a later date, freeze the filters in the tubes and keep them in the dark. (i.e. wrap tubes in rack with aluminum foil and place in freezer).

B. Extraction:

1. Remove the filter from the centrifuge tube and place it inside the female half of the tissue grinder. Be sure filter falls all the way to the bottom of grinder. Do not use any acetone or start grinding until filter is in place.
2. Add 2 aliquots ~ 2.8 mls each of 90% acetone/ $MgCO_3$ using the automatic pipettor. (The $MgCO_3$ keeps the acetone basic and prevents the chlorophyll a from breaking down.)
3. Vortex on high to break up filter. Then, insert the male half of the tissue grinder, and proceed to grind the filter remnants until the sample is completely homogenized.
4. Lift the male half of the grinder, carefully, and rinse it into the female half with two aliquots 90% acet./susp., adding to extract.
5. Vortex to mix and pour the extract back into the centrifuge tube.
6. Add one aliquot ~ 2.8 mls of 90% acet./ $MgCO_3$ using the automatic pipettor to the grinder.
7. Vortex to rinse and add rinse to centrifuge tube.
8. Using the pipettor, bring the volume in the centrifuge tube to 12 ml. with 90% acet./susp.. Mix well with a Pasteur pipet. Cork.
9. Place each centrifuge tube in a rack in a covered container.
10. Repeat one in five samples and do two blanks. When all of the samples are done, place the tubes in the coldroom (4 °C) and steep for 24 hrs. in dark..

C. Analysis:

1. Remove rack from cold room and place tubes into white DYNAC centrifuge (in

- ME area).
2. Set the timer for 30 min., and run centrifuge at full speed. (Speed should be increased in a couple of increments.)
 3. Program the spectrophotometer (Varian DMS-90, UV/visible) according to #3.5 Multi wavelength operation pg. 15 in the Operation manual. Use 90% acetone in the 2 cm cells as blanks and program the spec. to read 630 nm, 645 nm, 664 nm, 665 nm, 750nm. Zero the instrument at 630 nm, and check the zero at 647, 664 and 750. Subtract the slight reading for zero found at 750 nm from the sample's absorbance at 750 nm.
 4. Remove the samples from the centrifuge and place into rack in the covered container.
 5. Empty the cuvette to be used to read the samples, (the one at the front) and place it on a Kimwipe.,
 6. With a Pasteur pipet proceed to pipette the sample into the cuvette, carefully so as not to disturb the sediment in the bottom of the centrifuge tube. Fill only to the stem leaving room for HCl addition later.
 7. Place the cover on the cuvette, wipe faces with a clean Kimwipe, and check that they are clean. Then place cuvette in spectrophotometer.
 8. Start the spectrophotometer running in multi mode and record readings at 630, 647, 664, and 750nm.
 9. Remove the cuvette and add 0.2 ml of 0.1 N HCL. Turn cuvette upside down 3X to mix the sample. Record the readings at 665, and 750nm, after waiting at least 1 min. but no more than 2 minutes after adding the acid. Note: In multi mode the spectrophotometer pauses for 10 seconds after each wavelength. If you wait approx. 45 sec. after adding the acid then start the spec., the 665, 750nm wavelengths will read between 1 min. 15 sec. and 1 min 35 sec.
 10. Dump the sample into waste container for acetone.
 11. Using the automatic pipettor fill cuvette halfway with 90% to rinse it, and dump into waste container.
 12. Repeat steps #5 through #11 for each sample.

XII CALCULATIONS

Three parameters are determined:

- A. Uncorrected chlorophyll a, this includes both chlorophyll a, and its degradation product pheophytin a but subtracts out chl b and c. (Trichromatic method.)

$$a(\mu\text{g/L}) = \frac{(11.85(\text{OD}_{664} - \text{OD}_{760}) - 1.54(\text{OD}_{647} - \text{OD}_{750}) - 0.08(\text{OD}_{630} - \text{OD}_{750})) \times \text{ml extract} \times 10^3}{[\text{ml sample} \times \text{cell path length cm.}]}$$

- B. Corrected chlorophyll a

$$\text{CORR. a } (\mu\text{g/L}) = \frac{[26.73((\text{OD}_{664} - \text{OD}_{750}) - (\text{OD}_{665a} - \text{OD}_{750a})) \times \text{ml extract} \times 10^{31}]}{\text{X ml sample} \times \text{cell path length cm.}}$$

C. PHEOPHYTIN a

$$\text{PHEO a } (\mu\text{g/L}) = \frac{[26.73(1.7(\text{OD}_{665a} - \text{OD}_{750a}) - (\text{OD}_{664} - \text{OD}_{750})) \times \text{ml extract} \times 10^{31}]}{[\text{ml sample} \times \text{light path length cm}]}$$

Where a = reading after acidification

XII REPORTING

Detection limit is 0.1 $\mu\text{g/l}$.

CONCENTRATION RANGE

0.1 - 9.9 $\mu\text{g/l}$

10 - 100 $\mu\text{g/l}$

REPORT TO NEAREST

0.1 $\mu\text{g/l}$

1 $\mu\text{g/l}$

F:\lab\chem\wpdocs\96chlora.sop

Soak for 2 min in a second 100% propanol wash, filter, and add xylene. At least two washes are required; let the final one soak 10 min before filtering. Trim the xylene-soaked filter and place on a microscope slide on which there are several drops of mounting medium.† Apply several more drops of medium to top of filter and install a cover glass. Carefully squeeze out excess mounting medium. Make the final mount permanent by lacquering the edges of the cover glass.

Count organisms using the most appropriate magnification. "Live" diatoms typically are red while "dead" ones are unstained. Oil immersion is necessary for species identifications of diatoms and many other algae. Count either strips or random fields and calculate plankton densities per milliliter:

$$\text{No./mL} = \frac{C \times A_t}{A_c \times V}$$

where:

C = number of organisms counted,

A_t = total area of effective filter before trimming and mounting,

† Permout, Fisher Scientific Co., or equivalent.

A_c = area counted (strips or fields), and

V = volume of sample filtered, mL.

3. References

1. INGRAM, W.M. & C.M. PALMER. 1952. Simplified procedures for collecting, examining, and recording plankton in water. *J. Amer. Water Works Assoc.* 44:617.
2. STRICKLAND, J.D.H. & T.R. PARSONS. 1968. A Practical Manual of Sea Water Analysis. Fish. Res. Board Can. Bull. No. 167. Queen's Printer, Ottawa, Ont.
3. PALMER, C.M. & T.E. MALONEY. 1954. A New Counting Slide for Nannoplankton. Spec. Publ. No. 21, American Soc. Limnology & Oceanography.
4. SOURNIA, A., ed. 1978. Phytoplankton Manual. Monogr. Oceanogr. Methodol. No. 6. United Nations Educational, Scientific & Cultural Org., Paris.
5. LACKEY, J.B. 1938. The manipulation and counting of river plankton and changes in some organisms due to formalin preservation. *Pub. Health Rep.* 53:2080.
6. OWEN, B.B., JR., M. AFZAL & W.R. CODY. 1978. Staining preparations for phytoplankton and periphyton. *Brit. Phycol. J.* 13:155.

10200 G. Zooplankton Counting Techniques

1. Subsampling

Count entire samples having low zooplankton numbers (<200 zooplankters) without subsampling. However, most zooplankton samples will contain more organisms than can be enumerated practically; therefore, use a subsampling procedure. Before subsampling, remove and enumerate all large uncommon organisms such as fish larvae in fresh water or coelenterates, decapods, fish larvae, etc., in salt water. Subsample by the pipet or splitting method.

In the pipet method, adjust sample to a convenient volume in a graduated cylinder or Imhoff cone. Concentrating the plankton by using a rubber bulb and clear acrylic plastic tube with fine mesh netting fitted on the end is convenient and accurate (Figure 10200:9). For picoplankton and the smaller microzooplankton, use sedimentation techniques described for concentrating phytoplankton. Transfer sample to a beaker or other wide-mouth vessel for subsampling with a Hensen-Stempel or similar wide-bore pipet. Gently stir sample completely and randomly with the pipet and quickly withdraw 1 to 5 mL. Transfer to a suitable counting chamber.

Alternatively, subsample by splitting with any of a number of devices of which the Folsom plankton splitter¹ is best known (Figure 10200:10). Level splitter before using. Place sample in the splitter and divide into subsplits. Rinse splitter into the subsamples. Repeat until a workable number (200 to 500 individuals) is obtained in a subsample. Exercise care to provide unbiased splits. Even when using the Folsom splitter unbiased subsamples cannot be unquestioningly assumed;² therefore, count animals in several subsamples from the same sample to verify that the splitter is unbiased and to determine the sampling error introduced by using it.

Another method permits abundance estimates of more equivalent levels of precision among taxa than obtained with either

the Hensen-Stempel pipet or the Folsom splitter.³ Normal counting procedures tally organisms on the basis of their abundance in a sample. Therefore, in a sample with a dominant organism making up 50% of total numbers, the tally of the dominant taxon will be large and have a small error. However, error about the subdominants will increase as the tally of each taxon decreases. By accepting one level of precision, the technique³ has been developed to obtain the same error about dominants and subdominants, permitting quantitative comparisons between taxa over successive times or between stations.

2. Enumeration

Using a compound microscope and a magnification of 100×, enumerate small zooplankton (protozoa, rotifers, and nauplii) in a 1- to 5-mL clear acrylic plastic counting cell fitted with a glass cover slip. For larger, mature microcrustacea use a counting chamber holding 5 to 10 mL. A Sedgwick-Rafter cell is not suitable because of size. An open counting chamber 80 by 50 mm and 2 mm deep is desirable; however, an open chamber is difficult to move without jarring and disrupting the count. A mild detergent solution placed on the chamber before counting reduces organism movements or special counting trays with parallel or circular grooves or partitions^{4,5} can be used. Count microcrustacea with a binocular dissecting microscope at 20× to 40× magnification. If identification is questionable, remove organisms with a microbiological transfer loop and examine at a higher magnification under a compound microscope.

Report smaller zooplankton as number per liter and larger forms as number per cubic meter:

$$\text{No./m}^3 = \frac{C \times V'}{V'' \times V''}$$

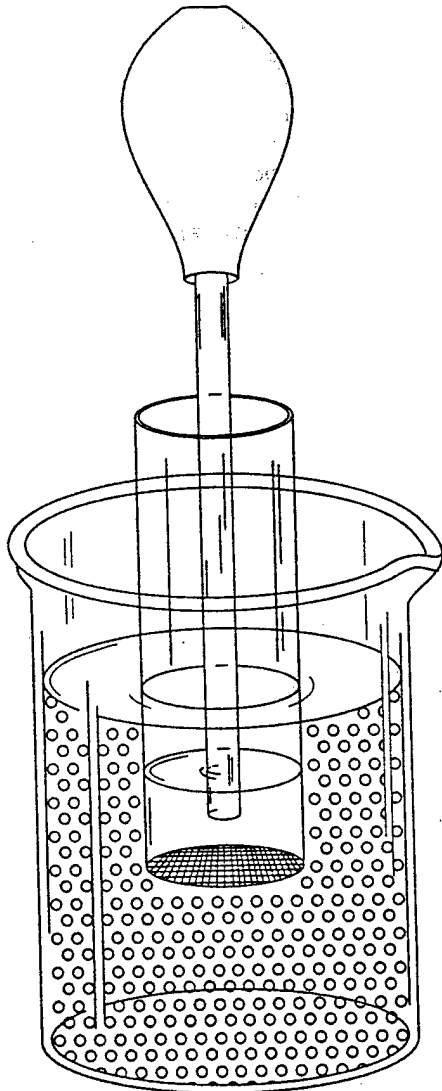


Figure 10200:9. A simple, efficient device for concentrating plankton. The tube is lowered into the beaker containing the sample. Water filtering into the tube is removed with the rubber bulb. The filter is nylon monofilament screen cloth that is glued to the bottom of the tube. The mesh size should be sufficiently small to prevent zooplankters from entering the filtrate (after Dodson and Thomas⁵).

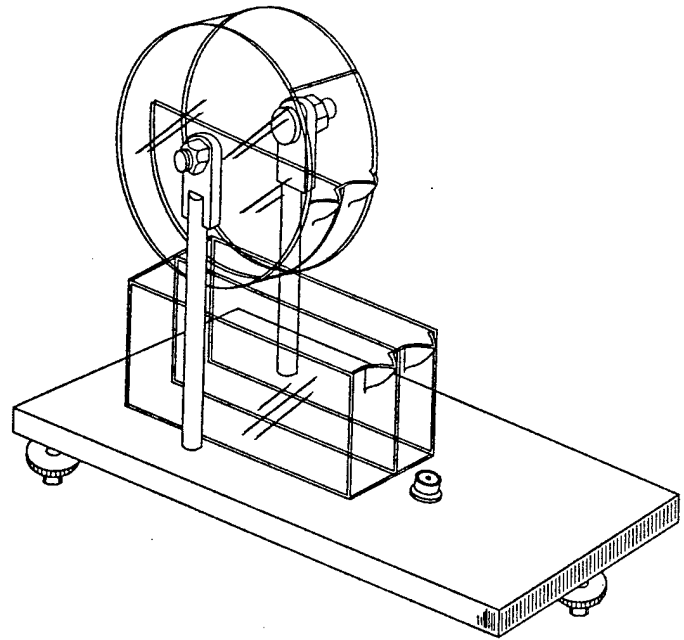


Figure 10200:10. The Folsom plankton splitter.

where:

- C = number of organisms counted,
- V' = volume of the concentrated sample, mL,
- V'' = volume counted, mL, and
- V''' = volume of the grab sample, m³.

To obtain organisms per liter divide by 1000.

3. References

1. LONGHURST, A.R. & D.L.R. SEIBERT. 1967. Skill in the use of Folsom's plankton sample splitter. *Limnol. Oceanogr.* 12:334.
2. McEWEN, G.F., M.W. JOHNSON & T.R. FOLSOM. 1954. A statistical analysis of the Folsom sample splitter based upon test observations. *Arch. Meteorol. Geophys. Bioklimatol.*, Ser. A, 6:502.
3. ALDEN, R.W., III, R.C. DAHIYA & R.J. YOUNG, JR. 1982. A method for the enumeration of zooplankton samples. *J. Exp. Mar. Biol. Ecol.* 59:185.
4. GANNON, J.E. 1971. Two counting cells for the enumeration of zooplankton micro-crustacea. *Trans. Amer. Microsc. Soc.* 90:486.
5. DODSON, A.N. & W.H. THOMAS. 1964. Concentrating plankton in gentle fashion. *Limnol. Oceanogr.* 9:455.

10200 H. Chlorophyll

The concentration of photosynthetic pigments is used extensively to estimate phytoplankton biomass.^{1,2} All green plants contain chlorophyll *a*, which constitutes approximately 1 to 2% of the dry weight of planktonic algae. Other pigments that occur in phytoplankton include chlorophylls *b* and *c*, xanthophylls, phycobilins, and carotenes. The important chlorophyll degradation products found in the aquatic environment are the chlorophyllides, pheophorbides, and pheophytins. The presence or absence of the various photosynthetic pigments is used, among other features, to separate the major algal groups.

The three methods for determining chlorophyll *a* in phytoplankton are the spectrophotometric,³⁻⁵ the fluorometric,⁶⁻⁸ and the high-performance liquid chromatographic (HPLC) techniques.⁹ Fluorometry is more sensitive than spectrophotometry, requires less sample, and can be used for in-vivo measurements.¹⁰ These optical methods can significantly under- or overestimate chlorophyll *a* concentrations,¹¹⁻¹⁸ in part because of the overlap of the absorption and fluorescence bands of co-occurring accessory pigments and chlorophyll degradation products.

Pheophorbide *a* and pheophytin *a*, two common degradation

products of chlorophyll *a*, can interfere with the determination of chlorophyll *a* because they absorb light and fluoresce in the same region of the spectrum as does chlorophyll *a*. If these pheopigments are present, significant errors in chlorophyll *a* values will result. Pheopigments can be measured either by spectrophotometry or fluorometry, but in marine and freshwater environments the fluorometric method is unreliable when chlorophyll *b* co-occurs. Upon acidification of chlorophyll *b*, the resulting fluorescence emission of pheophytin *b* is coincident with that of pheophytin *a*, thus producing underestimation and overestimation of chlorophyll *a* and pheopigments, respectively.

HPLC is a useful method for quantifying photosynthetic pigments^{9,13,15,16,19-21} including chlorophyll *a*, accessory pigments (e.g., chlorophylls *b* and *c*), and chlorophyll degradation products (chlorophyllides, pheophorbides, and pheophytins). Pigment distribution is useful for quantitative assessment of phytoplankton community composition and zooplankton grazing activity.²²

1. Pigment Extraction

Conduct work with chlorophyll extracts in subdued light to avoid degradation. Use opaque containers or wrap with aluminum foil. The pigments are extracted from the plankton concentrate with aqueous acetone and the optical density (absorbance) of the extract is determined with a spectrophotometer. The ease with which the chlorophylls are removed from the cells varies considerably with different algae. To achieve consistent complete extraction of the pigments, disrupt the cells mechanically with a tissue grinder.

Glass fiber filters are preferred for removing algae from water. The glass fibers assist in breaking the cells during grinding, larger volumes of water can be filtered, and no precipitate forms after acidification. Inert membrane filters such as polyester filters may be used where these factors are irrelevant.

a. Equipment and reagents:

1) *Tissue grinder*:* Successfully macerating glass fiber filters in tissue grinders with grinding tube and pestle of conical design may be difficult. Preferably use round-bottom grinding tubes with a matching pestle having grooves in the TFE tip.

2) *Clinical centrifuge*.

3) *Centrifuge tubes*, 15-mL graduated, screw-cap.

4) *Filtration equipment*, filters, glass fiber† or membrane (0.45- μ m porosity, 47-mm diam); vacuum pump; solvent-resistant disposable filter assembly, 1.0- μ m pore size;‡ 10-mL solvent-resistant syringe.

5) *Saturated magnesium carbonate solution*: Add 1.0 g finely powdered MgCO₃ to 100 mL distilled water.

6) *Aqueous acetone solution*: Mix 90 parts acetone (reagent-grade BP 56°C) with 10 parts saturated magnesium carbonate solution. For HPLC pigment analysis, mix 90 parts HPLC-grade acetone with 10 parts distilled water.

b. Extraction procedure:

1) Concentrate sample by centrifuging or filtering as soon as possible after collection. If processing must be delayed, hold samples on ice or at 4°C and protect from exposure to light. Use opaque bottles because even brief exposure to light during stor-

age will alter chlorophyll values. Samples on filters taken from water having pH 7 or higher may be placed in airtight plastic bags and stored frozen for 3 weeks. Samples from acidic water must be processed promptly to prevent chlorophyll degradation. Use glassware and cuvettes that are clean and acid-free.

2) Place sample in a tissue grinder, cover the 2 to 3 mL 90% aqueous acetone solution, and macerate at 500 rpm for 1 min. Use TFE/glass grinder for a glass-fiber filter and glass/glass grinder for a membrane filter.

3) Transfer sample to a screw-cap centrifuge tube, rinse grinder with a few milliliters 90% aqueous acetone, and add the rinse to the extraction slurry. Adjust total volume to 10 mL, with 90% aqueous acetone. Use solvent sparingly and avoid excessive dilution of pigments. Steep samples at least 2 h at 4°C in the dark. Glass fiber filters of 25- and 47-mm diam§ have dry displacement volumes of 0.03 and 0.10 mL, respectively, and introduce errors of about 0.3 and 1.0% if a 10-mL extraction volume is used.

4) Clarify by filtering through a solvent-resistant disposable filter (to minimize retention of extract in filter and filter holder, force 1 to 2 mL air through the filter after the extract), or by centrifuging in closed tubes for 20 min at 500 g. Decant clarified extract into a clean, calibrated, 15-mL, screw-cap centrifuge tube and measure total volume. Proceed as in 2, 3, 4, or 5 below.

2. Spectrophotometric Determination of Chlorophyll

a. Equipment and reagents:

1) *Spectrophotometer*, with a narrow band (pass) width (0.5 to 2.0 nm) because the chlorophyll absorption peak is relatively narrow. At a spectral band width of 20 nm the chlorophyll *a* concentration may be underestimated by as much as 40%.

2) *Cuvettes*, with 1-, 4-, and 10-cm path lengths.

3) *Pipets*, 0.1- and 5.0-mL.

4) *Hydrochloric acid*, HCl, 0.1N.

b. *Determination of chlorophyll a in the presence of pheophytin a*: Chlorophyll *a* may be overestimated by including pheopigments that absorb near the same wavelength as chlorophyll *a*. Addition of acid to chlorophyll *a* results in loss of the magnesium atom, converting it to pheophytin *a*. Acidify carefully to a final molarity of not more than $3 \times 10^{-3}M$ to prevent certain accessory pigments from changing to absorb at the same wavelength as pheophytin *a*.¹³ When a solution of pure chlorophyll *a* is converted to pheophytin *a* by acidification, the absorption-peak-ratio (OD₆₆₄/OD₆₆₅) of 1.70 is used in correcting the apparent chlorophyll *a* concentration for pheophytin *a*.

Samples with an OD₆₆₄ before/OD₆₆₅ after acidification ratio (664_o/665_a) of 1.70 are considered to contain no pheophytin *a* and to be in excellent physiological condition. Solutions of pure pheophytin show no reduction in OD₆₆₅ upon acidification and have a 664_o/665_a ratio of 1.0. Thus, mixtures of chlorophyll *a* and pheophytin *a* have absorption peak ratios ranging between 1.0 and 1.7. These ratios are based on the use of 90% acetone as solvent. Using 100% acetone as solvent results in a chlorophyll *a* before-to-after acidification ratio of about 2.0.³

Spectrophotometric procedure—Transfer 3 mL clarified extract to a 1-cm cuvette and read optical density (OD) at 750 and 664 nm. Acidify extract in the cuvette with 0.1 mL 0.1N HCl. Gently agitate the acidified extract and read OD at 750 and at 665 nm, 90 s after acidification. The volumes of extract and acid

* Kontes Glass Co., Vineland, N.J. 08360: Glass/glass grinder, Model No. 8855; Glass/TFE grinder, Model 886000; or equivalent.

† Whatman GF/F (0.7 μ m), GFB (1.0 μ m), Gelman AE (1 μ m),²³ or equivalent.

‡ Gelman Acrodisc or equivalent.

§ GF/F or equivalent.

and the time after acidification are critical for accurate, consistent results.

The OD664 before acidification should be between 0.1 and 1.0. For very dilute extracts use cuvettes having a longer path length. If a larger cell is used, add a proportionately larger volume of acid. Correct OD obtained with larger cuvettes to 1 cm before making calculations.

Subtract the 750-nm OD value from the readings before (OD 664 nm) and after acidification (OD 665 nm).

Using the corrected values calculate chlorophyll *a* and pheophytin *a* per cubic meter as follows:

$$\text{Chlorophyll } a, \text{ mg/m}^3 = \frac{26.7 (664_b - 665_a) \times V_1}{V_2 \times L}$$

$$\text{Pheophytin } a, \text{ mg/m}^3 = \frac{26.7 [1.7 (665_a) - 664_b] \times V_1}{V_2 \times L}$$

where:

V_1 = volume of extract, L,

V_2 = volume of sample, m³,

L = light path length or width of cuvette, cm, and

664_b, 665_a = optical densities of 90% acetone extract before and after acidification, respectively.

The value 26.7 is the absorbance correction and equals $A \times K$

where:

A = absorbance coefficient for chlorophyll *a* at 664 nm = 11.0, and

K = ratio expressing correction for acidification.

$$\begin{aligned} &= \frac{\left(\frac{664_b}{665_a}\right) \text{ pure chlorophyll } a}{\left(\frac{664_b}{665_a}\right) \text{ pure chlorophyll } a - \left(\frac{664_b}{665_a}\right) \text{ pure pheophytin } a} \\ &= \frac{1.7}{1.7 - 1.0} = 2.43 \end{aligned}$$

c. Determination of chlorophyll *a*, *b*, and *c* (trichromatic method):

Spectrophotometric procedure—Transfer extract to a 1-cm cuvette and measure optical density (OD) at 750, 664, 647, and 630 nm. Choose a cell path length or dilution to give OD664 between 0.1 and 1.0.

Use the optical density readings at 664, 647, and 630 nm to determine chlorophyll *a*, *b*, and *c*, respectively. The OD reading at 750 nm is a correction for turbidity. Subtract this reading from each of the pigment OD values of the other wavelengths before using them in the equations below. Because the OD of the extract at 750 nm is very sensitive to changes in the acetone-to-water proportions, adhere closely to the 90 parts acetone:10 parts water (v/v) formula for pigment extraction. Turbidity can be removed easily by filtration through a disposable, solvent-resistant filter attached to a syringe or by centrifuging for 20 min at 500 g.

Calculate the concentrations of chlorophyll *a*, *b*, and *c* in the extract by inserting the corrected optical densities in following equations:⁵

$$\text{a) } C_a = 11.85(\text{OD}664) - 1.54(\text{OD}647) - 0.08(\text{OD}630)$$

$$\text{b) } C_b = 21.03(\text{OD}647) - 5.43(\text{OD}664) - 2.66(\text{OD}630)$$

$$\text{c) } C_c = 24.52(\text{OD}630) - 7.60(\text{OD}647) - 1.67(\text{OD}664)$$

where:

C_a , C_b , and C_c = concentrations of chlorophyll *a*, *b*, and *c*, respectively, mg/L, and

OD664, OD647,

and OD630 = corrected optical densities (with a 1-cm light path) at the respective wavelengths.

After determining the concentration of pigment in the extract, calculate the amount of pigment per unit volume as follows:

$$\text{Chlorophyll } a, \text{ mg/m}^3 = \frac{C_a \times \text{extract volume, L}}{\text{volume of sample, m}^3}$$

3. Fluorometric Determination of Chlorophyll *a*

The fluorometric method for chlorophyll *a* is more sensitive than the spectrophotometric method and thus smaller samples can be used. Calibrate the fluorometer spectrophotometrically with a sample from the same source to achieve acceptable results. Optimum sensitivity for chlorophyll *a* extract measurements is obtained at an excitation wavelength of 430 nm and an emission wavelength of 663 nm. A method for continuous measurement of chlorophyll *a* in vivo is available, but is reported to be less efficient than the in-vitro method given here, yielding about one-tenth as much fluorescence per unit weight as the same amount in solution. Pheophytin *a* also can be determined fluorometrically.²⁴

a. Equipment and reagents: In addition to those listed under 1a and 2a above:

Fluorometer, equipped with a high-intensity F4T.5 blue lamp, photomultiplier tube R-446 (red-sensitive), sliding window orifices 1 ×, 3 ×, 10 ×, and 30 ×, and filters for light emission (CS-2-64) and excitation (CS-5-60). A high-sensitivity door is preferable.

b. Extraction procedure: Prepare sample as directed in 1b above.

1) Calibrate fluorometer with a chlorophyll solution of known concentration as follows: Prepare chlorophyll extract and analyze spectrophotometrically. Prepare serial dilutions of the extract to provide concentrations of approximately 2, 6, 20, and 60 μg chlorophyll *a*/L. Make fluorometric readings for each solution at each sensitivity setting (sliding window orifice): 1 ×, 3 ×, 10 ×, and 30 ×. Using the values obtained, derive calibration factors to convert fluorometric readings in each sensitivity level to concentrations of chlorophyll *a*, as follows:

$$F_s = \frac{C_s}{R_s}$$

where:

F_s = calibration factor for sensitivity setting S ,

R_s = fluorometer reading for sensitivity setting S , and,

C_s = concentration of chlorophyll *a* determined spectrophotometrically, μg/L.

2) Measure sample fluorescence at sensitivity settings that will provide a midscale reading. (Avoid using the 1 × window because of quenching effects.) Convert fluorescence readings to concentrations of chlorophyll *a* by multiplying the readings by the appropriate calibration factor.

⁵ Model 10-005, Turner Designs, Sunnyvale, Calif. or equivalent.

c. Determination of chlorophyll a in the presence of pheophytin

a: This method normally is not applicable to freshwater samples. See discussion under 10200G and 1c above.

1) **Equipment and reagents**—In addition to those listed under 1a and 2a above, pure chlorophyll *a*# (or a plankton chlorophyll extract with a spectrophotometric before-and-after acidification ratio of 1.70 containing no chlorophyll *b*).

2) **Fluorometric procedure**—Calibrate fluorometer as directed in ¶ 3b1). Determine extract fluorescence at each sensitivity setting before and after acidification. Calculate calibration factors (F_s) and before-and-after acidification fluorescence ratio by dividing fluorescence reading obtained before acidification by the reading obtained after acidification. Avoid readings on the 1 × scale and those outside the range of 20 to 80 fluorometric units.

3) **Calculations**—Determine the “corrected” chlorophyll *a* and pheophytin *a* in sample extracts with the following equations:^{8,24}

$$\text{Chlorophyll } a, \text{ mg/m}^3 = F_s \frac{r}{r-1} (R_b - R_a) \frac{V_e}{V_s}$$

$$\text{Pheophytin } a, \text{ mg/m}^3 = F_s \frac{r}{r-1} (rR_a - R_b) \frac{V_e}{V_s}$$

where:

- F_s = conversion factor for sensitivity setting *S* (see ¶ 2b, above),
- R_b = fluorescence of extract before acidification,
- R_a = fluorescence of extract after acidification,
- $r = R_b/R_a$, as determined with pure chlorophyll *a* for the instrument (redetermine r and F_s if filters or light source are changed),
- V_e = volume of extract, and
- V_s = volume of sample.

d. Extraction of whole water, nonfiltered samples: Alternatively, to prevent cell lysis during filtration, extract whole water sample.

1) **Equipment and reagents**—Fluorometer equipped with a high-sensitivity R928 phototube** with output impedance of 36 ma/W at 675 nm and a high-sensitivity door. Place neutral density filter (40–60N) in the rear light path,†† selected to permit reagent blanking on the highest sensitivity scale.

2) **Extraction procedure**—Decant 1.5 mL sample into screw-cap test tube and add 8.5 mL 100% acetone. Mix with vortex mixer and hold in the dark for 6 h at room temperature. Filter through glass fiber filter‡‡ or centrifuge. Measure fluorescence as described in Section 10200H.3 and estimate concentrations as in ¶ 3c. Because humic substances interfere, if they are present filter a sample portion (see 10200H.1b) and process filtrate with sample. Subtract filtrate (blank) fluorescence from that of sample.

4. High-Performance Liquid Chromatographic Determination of Algal Chlorophylls and Their Degradation Products

a. Equipment and reagents: In addition to those listed for pigment extraction, ¶ 1a above:

1) **High-pressure liquid chromatograph** capable of a flow rate of 2.0 mL/min.

2) **High-pressure injector valve** equipped with a 100-μL sample loop.

3) **Guard column** (4.0 × 0.5 cm, C₁₈ packing material, 3-μm particle size, or equivalent protection system) for extending life of primary column.

4) **Reverse-phase HPLC column**.§§

5) **Fluorescence detector** capable of excitation at 430 ± 30 nm and measuring emission at wavelengths greater than 600 nm.

6) **Data recorder device:** Strip chart recorder or, preferably, an electronic integrator.

7) **Syringe**, glass, 250-μL.

8) **HPLC eluents:** System A (80:15:5; methanol:Type I reagent water:ion-pairing solution) and System B (80:20; methanol:acetone). Use HPLC-grade solvents; measure volumes before mixing. Filter eluents through a solvent-resistant 0.4-μm filter before use and degas with helium. Prepare the ion-pairing (IP) solution from 15 g tetrabutylammonium acetate|| and 77 g ammonium acetate## made up to 1 L with Type I reagent water.¹⁵

9) **Calibration standards:** Individually dissolve 1 mg each pure chlorophyll *a* and *b*|| in 100 mL 90% acetone. Determine the exact concentrations spectrophotometrically (ϵ_{664} for chlorophyll *a* in 90% acetone = 87.67 L g⁻¹ cm⁻¹; ϵ_{647} for chlorophyll *b* in 90% acetone = 51.36 L g⁻¹ cm⁻¹).⁵ Prepare pheophytin *a* + *a'* and *b* + *b'* standards from the primary chlorophyll *a* and *b* standards by acidification with hydrochloric acid; correct respective concentrations for Mg²⁺ loss. Extract chlorophyll *c* with 90% acetone from diatoms, purify by thin-layer chromatography (TLC)²⁵ and calibrate spectrophotometrically (ϵ_{631} for a mixture containing equal amounts of chlorophylls *c*₁ and *c*₂ in 90% acetone containing 1% pyridine = 42.6 L g⁻¹ cm⁻¹; the absence of this small amount of pyridine is presumed to cause only small differences in the absorption properties of chlorophyll *c*.²⁶ Alternatively, determine the chlorophyll *c* content of a 90% acetone extract made from diatoms, spectrophotometrically (chlorophyll *c*₁ + *c*₂, μg/mL = 24.36E₆₃₀ - 3.73E₆₆₄)⁵ and use as standard. Prepare chlorophyllide *a* from diatoms,²⁷ purify by TLC²⁵ and calibrate spectrophotometrically in 90% acetone (ϵ_{664} for chlorophyllide *a* = 128 L g⁻¹ cm⁻¹).²⁸ Prepare pheophorbide *a* by acidification of chlorophyllide *a*, purify by TLC,²⁵ and calibrate spectrophotometrically in 90% acetone (ϵ_{665} for pheophorbide *a* = 69.8 L g⁻¹ cm⁻¹).²⁸ Standards stored under nitrogen in the dark at -20°C are stable for about 1 month.

b. Procedure:

1) Set up and equilibrate the HPLC system with solvent System A at a flow rate of 2 mL/min. Adjust fluorometer sensitivity to provide full-scale reading with the most concentrated chlorophyll *a* standard.

2) Calibrate HPLC system by preparing working standards from the primary standards (on day of use). Once retention times of the standards are determined for a particular system, simplify standardization by preparing serial dilutions from mixed standards. Prepare separately mixed standards for the chlorophylls and chlorophyllide *a* and for the pheophytins and pheophorbide *a*. Mix 1-mL portions of standards with 300 μL ion-pairing solutions and equilibrate for 5 min before injection (use of ion-pairing agents greatly enhances separation of dephytylated pigments, chlorophyllide *a*, chlorophyll *c*, and pheophorbide *a*). Prepare blanks by mixing 1 mL 90% acetone with 300 μL IP solution. Rinse syringe twice with 150 μL standard and draw

Purified chlorophyll *a*, Sigma Chemical Company, St. Louis, Mo., or equivalent.

** Hamamatsu Corp., Middlesex, N.J., or equivalent.

†† If using Model 10-005, Turner Designs, or equivalent.

‡‡ Whatman GF/F or equivalent.

§§ Microsorb C₁₈ column, 10 cm long, 3-μm particle size, Rainin Co., or equivalent.

|| Fluka Chemical Corp., 980 South Second Street, Ronkonkoma, N.Y., or equivalent.

Sigma Chemical Company, or equivalent.

about 250 μL standard into syringe for injection. Place syringe in injector valve, overfilling the 100- μL sample loop. Construct calibration curves by plotting fluorescence peak areas (or heights) against standard pigment concentrations.

3) Prepare samples for injection by mixing a 1-mL portion of the 90% acetone pigment extract with 300 μL IP solution.

4) Use a two-step solvent program to optimize separation of the chlorophylls from their degradation products.¹⁵ After injection, change from solvent System A to System B over 5 min and follow with System B for 15 min at a flow rate of 2 mL/min. Re-equilibrate the column with System A for 5 min before the next injection for a total analysis time of approximately 25 min. Degas the solvent systems with helium during analysis. Increase lifetime of HPLC column by storing it in 100% methanol between runs. Periodically flush the HPLC system with reagent water (Type I) to avoid buildup of ion pairing agents.

5) Calculate individual pigment concentrations using the following formula:

$$C_i = \frac{A_i F_i V_E}{V_i V_S}$$

where:

- C_i = individual pigment concentration, mg/L,
- A_i = area of individual pigment peak from sample injection,
- F_i = standard response factor (mg pigment/0.1 mL standard divided by corresponding peak area),
- V_i = injection volume (0.1 mL),
- V_E = extraction volume, mL, and
- V_S = sample volume, L.

6) This method is designed only for quantification of chlorophylls and their degradation products. Detect carotenoid pigments, which also are present in 90% acetone extracts but do not fluoresce, by absorbance spectroscopy (at about 440 nm).²¹

7) The elution order and approximate retention times for the major chlorophyll pigments and their degradation products are shown in Figure 10200:11. The detection limits ($s/n = 2$) vary with fluorometer configuration and flow rate; however, they range from 10 to 100 pg per injection for most chlorophylls and their degradation products.^{15,21,29} The accuracy of the HPLC method depends primarily on purity of pigment standards. Preferably measure absorption spectra (350 to 750 nm) of the standards and compare with published data. Pigment purity also can be assessed by HPLC analysis, providing there are no co-eluting contaminants with absorption and fluorescence bands overlapping those of the standards. HPLC and spectrophotometrically derived pigment concentrations for available EPA standards agree reasonably well ($\pm 20\%$) if spectrophotometric results are corrected for the presence of pheopigments and the HPLC results are expressed as pigment equivalents (e.g., chlorophyll *a* equivalents = chlorophyllide *a* + chlorophyll *a* + chlorophyll *a'*, provided that the proper molecular weight corrections are applied).³⁰ Thus, if significant amounts of chlorophyll derivatives are present, pigment concentrations determined spectrophotometrically will be overestimated. The agreement between HPLC and fluorometrically derived results depends on the presence of accessory chlorophylls *b*, *c*, and their derivatives. Triplicate injections of a fivefold dilution of an EPA sample gave coefficients of variation of 7.5% (chlorophyllide *a*), 9.1% (chlorophyll *c*), 13.4% (pheophorbide *a*), 9.6% (chlorophyll *b*), 0.5% (chlorophyll *a*), 6.2% (pheophytin *a*), and 22.9% (pheophytin *a'*), with an average value of 10% for the seven pigments analyzed.

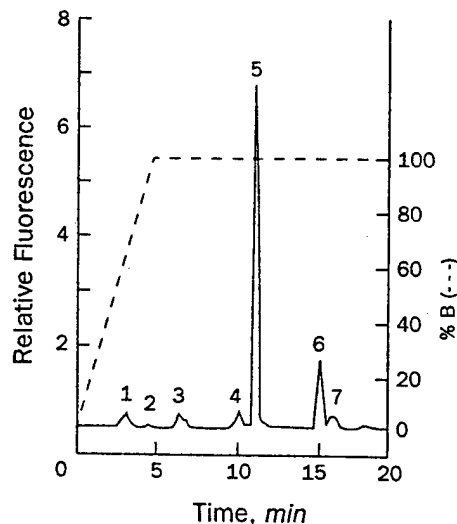


Figure 10200:11. Reverse-phase HPLC chromatogram for a fivefold dilution of EPA sample. Injection volume 100 μL ; peaks detected by fluorescence spectroscopy (λ_{ex} : 400–460 nm; λ_{em} : >600 nm). Peak identities are: 1—chlorophyllide *a*; 2—chlorophyll *c*; 3—pheophorbide *a*; 4—chlorophyll *b*; 5—chlorophyll *a*; 6—pheophytin *a*; and 7—pheophytin *a'*. The chlorophyll *b* degradation products, pheophytin *b* and pheophytin *b'*, were below detection limits. Peak identities confirmed by on-line diode array spectroscopy (350–550 nm).

5. High-Performance Liquid Chromatographic Determination of Algal Chlorophyll and Carotenoid Pigments (PROPOSED)

a. Equipment and reagents: In addition to those listed for pigment extraction, ¶ 1a above:

- 1) *High-performance liquid chromatographic pump* capable of gradient delivery of three different solvents at a flow rate of 1 mL/min.
- 2) *High-pressure injector valve* equipped with a 200- μL sample loop.
- 3) *Guard column* (50 \times 4.6 mm, C_{18} packing material,*** 5- μm particle size) for extending life of primary column.
- 4) *Reverse-phase HPLC column* with endcapping (250 \times 4.6 mm, 5- μm particle size, C_{18} column***).
- 5) *Variable wavelength or filter absorbance detector* with low-volume flowthrough cell. Detection wavelength is 436 nm.
- 6) *Data recording device:* Strip chart recorder or, preferably, an electronic integrator or computer equipped with hardware and software for chromatographic data analysis.
- 7) *Syringe, glass, 500- μL .*
- 8) *HPLC eluents:* Eluent A (80:20, v:v; methanol:0.5M ammonium acetate, pH 7.2); Eluent B (90:10, v:v; acetonitrile:water), and Eluent C, ethyl acetate. Use HPLC-grade solvents. Measure volumes before mixing. Filter eluents through a solvent-resistant 0.4- μm filter before use and degas with helium.
- 9) *Calibration standards:* Chlorophylls *a* and *b*, and β , β -carotene can be purchased††† as can zeaxanthin and lutein.‡‡‡ Other pigment standards can be purified from plant extracts by

*** Spherisorb ODS-2, Phase Separations Inc., Norwalk, Conn., or equivalent.

††† Sigma Chemical Co., St. Louis, Mo., or equivalent.

‡‡‡ Roth Chemical Co., distributed by Atomergic Chemetals Corp., Farmingdale, N. Y., or equivalent.

Appendix D:
Processing Results
for September 3, 1999

Results for September 3, 1999

Chlorophyll-a values were determined both spectrophotometrically and fluorimetrically.

The spectrophotometric results for Sep 3 are shown in Table D.1. The equations for converting the absorbance readings to concentrations are located in the Appendix C: Standard Methods.

Blank vs Blank acetone					0	0	0	-0.002		
Tube #	Sample #	Samp Vol ml	Xtr Vol ml	Light Path cm	Absorbance before acid				w/acid: 1 ml of 0.1N HCl	
					630 nm	647 nm	664 nm	750 nm	665a nm	750a nm
1	A3	600	10	1	0.007	0.008	0.013	0.004	0.01	0.005
2	I1	600	10	1	0.006	0.006	0.009	0.004	0.008	0.005
3	A2	600	10	1	0.008	0.009	0.015	0.005	0.012	0.006
4	I4	750	10	1	0.009	0.011	0.026	0.003	0.017	0.004
5	A6	800	10	1	0.005	0.006	0.014	0.002	0.01	0.004
6	A5	800	10	1	0.005	0.005	0.011	0.003	0.007	0.003

Tube #	Sample #	Chlorophyll a ug/L		Pheophytin ug/L
		corr. for b & c (Trichrom)	corr for pheophytin	
1	A3	1.670833	1.782	-0.22275
2	I1	0.9335	0.891	0.04455
3	A2	1.868333	1.782	0.0891
4	I4	3.463333	3.564	-0.32076
5	A6	1.6975	2.00475	-0.601425
6	A5	1.1445	1.3365	-0.40095

Table D.1 September 3, 1999 Chlorophyll-a concentrations – determined spectrophotometrically

Chlorophyll-a results were also determined fluorimetrically. The excitation bandpass was set at 20 nm in order to have a lot of signal and the data values were recorded at an

emission bandpass of 5 nm for a higher resolution. The concentrations were determined using a standard chlorophyll solution to calibrate the data values to concentrations. The fluorimetrically determined chlorophyll-a values are shown in Table D.2.

Sample #	Samp Vol ml	Xtr Vol ml	Data Value (20/5)	Conc (ug/L)
A3	600	10	42.61	1.49135
I1	600	10	21.94	0.7679
A2	600	10	50.09	1.75315
I4	750	10	102.26	2.86328
A6	800	10	58	1.5225
A5	800	10	38.53	1.011413

Table D.2 September 3, 1999 Chlorophyll-a values determined fluorimetrically

The TSS values were also calculated for each of the water samples and are shown in

Table D.3:

Filter #	Sample #	Vol Filtered (ml)	Pre-weight (g)	Post-weight (g)	Difference	TSS (mg/L)
1	A3	600	0.0351	0.0359	0.0008	1.3333333
2	I1	600	0.0354	0.036	0.0006	1
3	A2	600	0.0361	0.0367	0.0006	1
4	I4	750	0.0365	0.0383	0.0018	2.4
5	A6	800	0.0366	0.0372	0.0006	0.75
6	A5	800	0.0357	0.0365	0.0008	1

Table D.3 September 3, 1999 TSS Values

The CDOM scalar values were obtained from another student who performed the processing. These values are located in Table D.4.

Sample	CDOM (scalar)
I1	0.451
A5	0.485
A3	0.481
A6	0.454
A2	0.467
I4	0.438

Table D.4 September 3, 1999 CDOM Values

As a verification of my chlorophyll-a processing, three filters from the July 26, 1999 collect were delivered to the County Health Lab for processing. The results of the comparison are shown below in Table D.5. The County Health Lab chemists process chlorophyll samples on a weekly basis and felt that the outcome of the comparison indicates that our processes yield comparable results. Further development of a control is necessary to test the robustness of the RIT chlorophyll processing procedure, to include sending more samples to the Health Lab and testing to see how the presence of chlorophyll degrades over storage time.

Sample #	County Health Lab Results			RIT Results		
	Chlorophyll a (Corrected for b,c)	Chlorophyll a (Corrected for pheophytin)	Pheophytin	Chlorophyll a (Corrected for b,c)	Chlorophyll a (Corrected for pheophytin)	Pheophytin
I1/A8	3.8 ug/l	3.0 ug/l	1.4 ug/l	1.7 ug/l	1.3 ug/l	0.5 ug/l
I2/A6	15.8	9.6	9.5	15.3	10.7	7.3
I3/A15	7.1	5.7	2.3	4.7	3.3	2.3

Table D.5 Comparison of Chlorophyll-a processing results

Some of the discrepancies between the values determined by the County and RIT can be attributed to instrumentation and slight differences in processing. The spectrophotometer in the basement would not stay “zeroed”. After the blank acetone sample was zeroed, the reading on the blank fluctuated between -0.001 and -0.003 regardless of the number of times the blank sample was zeroed. The County Health Lab uses a Teflon tip on a drill to grind the glass filters. The grinders at RIT were glass and the glass filters tend to wear down the grinding texture of the pestel, decreasing its effectiveness in grinding. At times, the Health Lab uses filters that are larger in size and are not made of glass. These slight differences may account for some of the discrepancies.